ISSN: 1947-3931 (Print), 1947-394X (Online) Volume 1, Number 1, June 2009

Engineering

Prof. Hong Liu University of Oklahoma, USA

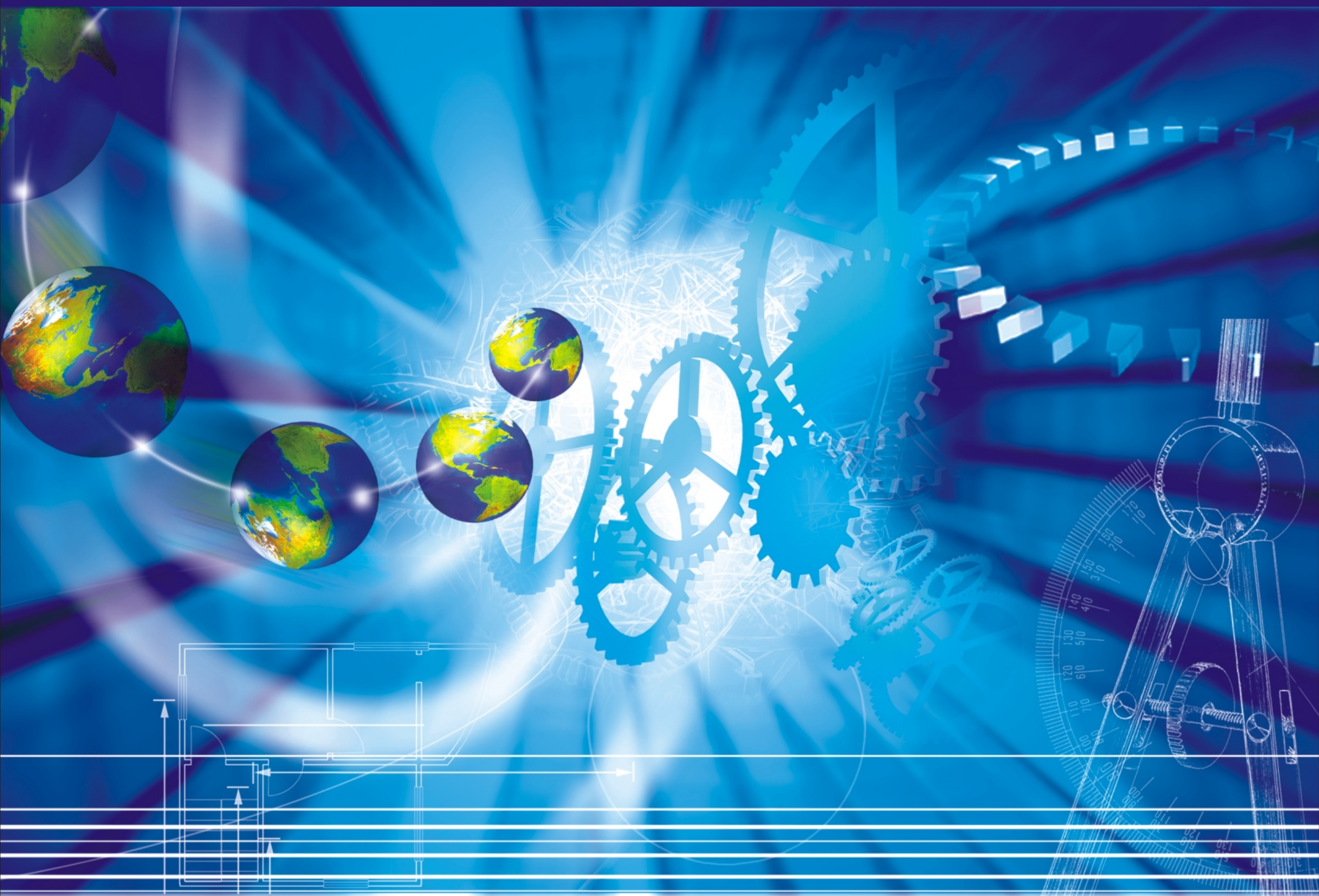

www.scirp.org/journal/eng/

Scientific Research

Journal Editorial Board

ISSN: 1947-3931 (Print), 1947-394X (Online)
http://www.scirp.org/journal/eng

Engineering, **2009, 1, 1-54**
Published Online June 2009 in SciRes (http://www.SciRP.org/journal/eng/).

TABLE OF CONTENTS

Volume 1 Number 1 June 2009

Engineering

Journal Information

SUBSCRIPTIONS

Engineering (Online at Scientific Research Publishing, www.SciRP.org) is published quarterly by Scientific Research Publishing, Inc., USA.

E-mail: eng@scirp.org

Subscription rates: Volume 1 2009

Print: $50 per copy.

Electronic: free, available on www.SciRP.org.

To subscribe, please contact Journals Subscriptions Department, E-mail: eng@scirp.org

Sample copies: If you are interested in subscribing, you may obtain a free sample copy by contacting Scientific Research Publishing, Inc at the above address.

SERVICES

Advertisements

Advertisement Sales Department, E-mail: eng@scirp.org

Reprints (minimum quantity 100 copies)

Reprints Co-ordinator, Scientific Research Publishing, Inc., USA.

E-mail: eng@scirp.org

COPYRIGHT

PRODUCTION INFORMATION

For manuscripts that have been accepted for publication, please contact:

E-mail: eng@scirp.org

***Engineering*, 2009, 1, 1-54**
Published Online June 2009 in SciRes (http://www.SciRP.org/journal/eng/).

Fractional Sampling Improves Performance of UMTS Code Acquisition

Francesco Benedetto, Gaetano Giunta
Department of Applied Electronics, University of ROMA TRE, Rome, Italy
Email: *fbenedet@uniroma3.it*
Received March 31,2009; *revised April* 24,2009; *accepted April* 28, 2009

Abstract

An improved technique with a fractional sampling based on two samples per chip, according to the Nyquist criterion, has been employed by the authors to enhance the performance in the code synchronization of UMTS (or W-CDMA) systems. In this paper, we investigate on the theoretical rationale of such a promising behavior. The performance is analyzed for several wireless channels, in the presence of typical pedestrian and vehicular scenarios of the IMT2000/UMTS cellular systems.

Keywords: Code Synchronization, Spread Spectrum, Cell Search, UMTS, W-CDMA, Wireless Access

1. Introduction

Initial cell search in the wireless access of the International Mobile Telecommunications-2000/Universal Mobile Telecommunications System (IMT2000/UMTS) is the process of the mobile station that includes the search for cell and scrambling codes as far as time synchronization [1]. In fact, the whole synchronization process in Wideband–Code Division Multiple Access (W-CDMA) [2] consists of five sequential steps: 1) slot synchronization; 2) frame synchronization and scrambling code group identification; 3) scrambling code identification; 4) frequency acquisition; 5) cell identification. This contribution addresses algorithms for the initial cell search before frequency acquisition, i.e. the stages 1-3. The combined goal of such stages is to deliver a reliable code-time candidate to the frequency acquisition stage. Several sequential statistical tests were suggested for such purposes [3−9]. In particular, effective non-coherent sequential pseudo-noise (PN) code acquisition using sliding correlation were proposed and analyzed for both chip-asynchronous [7−8] and synchronous [9] direct sequence spread-spectrum (DS/SS) communications. According to such attempts, one testing variable is accumulated after correlation (sometimes implemented as the output of a matched filter) with each possible PN code shifted by each code offset. That is, the decision device sequentially examines all the code offsets of all the possible PN codes. The testing thresholds are optimally set to provide the probability of detection and false alarm, required for the considered application.

This paper extends previous analyses (e.g. [2]) that made the simplifying assumption of one sample per chip. Such choice appears motivated when a rectangular pulse waveform is employed for spread-spectrum modulation, since finer timing estimation can be confined to subsequent acquisition steps [3−4]. Nevertheless, the author of the papers [7−8] already discussed some improvement from over-sampling. Practical acquisition and signal processing requires more than one sample per chip. In fact, using only one sample could result in a significant performance loss [10]. With a more appropriate discretization, we are considering the effect of time-sampling the chip waveform (and the received signal) at twice the chip rate on the performance of detection and acquisition schemes. In fact, IMT2000/UMTS standard employs raised-cosine spectral waveforms with non-zero roll-off [1,11], and it is then necessary to use receivers based on a fractional chip sampling, i.e. operating with more than one sample per chip.

The remainder of this paper is organized as follows. The use of fractional sampling to improve the performance of non-coherent sequential cell search procedure for PN code acquisition is presented and discussed in Section 2. The numerical results of the presented methods for application to the initial cell search (before frequency acquisition) of the IMT2000/UMTS cellular system is examined in Section 3 by a number of numerical results. Our conclusions are finally drawn in Section 4.

2. Improving the Code Synchronization by Fractional Sampling

In this paper, we match the conventional method, based on one sample per chip (like the operating cases reported in [2]), to the fractional technique operating at twice the chip rate. As already noted by [10], such choice matches the Nyquist criterion. Unfortunately, this choice doubles the computational complexity of receivers. Moreover, they must operate twice faster than a conventional receiver. Nevertheless, the current trend, providing higher and higher-speed microprocessors, is going to timely compensate for the augmented request of computational speed.

The author of the paper [7] already discussed some improvement from over-sampling. In particular, that original technique ("scheme 2" in [7]) implements the sampling of the received signal at twice the chip rate, but averages the samples at odd multiples of the half-chip period before a subsequent decimation by the factor 2. As a result, the final data clock is always synchronous with the chip rate. In practice, the average operation of the "scheme 2" in [7] as well as the matched filter correlation by the "averaged" code $\overline{c}(t)$ in [8] are equivalent to using the filter with impulse response $h(t)$ = $[\delta(t-T_c/2) + \delta(t+T_c/2)]/2$, corresponding to the low-pass frequency response $H(f) = cos(\pi T_c f)$, before down-sampling, where T_c is the chip period. In fact, it is well known [12] that some kind of anti-aliasing filtering is required before decimation to avoid the spectral alias error, at the cost of missing the information at frequencies higher than $1/2T_c$ (while the spectrum of a raised cosine waveform is actually as large as $(1+R)/2T_c$, where R is the roll-off). Unlike the method based on 2 samples/chip proposed in this paper, the effect of the "scheme 2" in [7] is to filter out (or, at least, attenuate) the (significant) signal components in all the transition bandwidth [12], that is:

$[(1-R)/2T_c,(1+R)/2T_c]$, because $H(1/2T_c)=0$.

In accordance with the logic scheme [7], let us consider D samples of the complex envelope of the received signal after the matched filter $\{r(iT_c-\tau T_c),\ i = 1, .., D\}$, discretized with the normalized timing offset τ, being $\tau=0$ (without loss of generality) in the chip-synchronous case while (randomly distributed) $-0.5\le\tau\le0.5$ in chip-asynchronous communications. The modified power detector operating at twice the chip rate first estimates the cross-correlation $\rho_w(k';\tau)$ (despreading the generic w-th data block made of D chips) between an over-sampled (by the factor 2) version of the received signal $r(t)$ after the matched filter and the code candidate $c(t)$ also for half-chip offsets kT_c:

$$\rho_w(k;\tau) = \frac{1}{2D}\sum_{i=1}^{2D} r(iT_c/2\text{-}\tau T_c)\cdot c^*(iT_c/2+kT_c)$$

$$\text{with } k = -1.5,-1,-0.5,0,\ 0.5,\ 1,\ 1.5 \qquad \textbf{(1)}$$

As pointed out in [7], the correct timing offset is randomly located ($-0.5\le\tau\le0.5$) in a chip-asynchronous system, being independent of the sampling times (either integer or half-integer multiples of the chip period T_c). As pointed out in [6], the worst case of erroneous synchronization with the conventional power detector will happen if the cross-correlation is computed for an offset which is just in the middle between two chips. In such a case, an error of half chip will affect the estimates. In our method, the worst offset is located at $T_c/4$ instead of $T_c/2$. In practice, the maximum offset error is the half of the conventional detector. As a consequence, the worst case can be modeled by testing the null hypothesis H_0 against the worst positive hypothesis with $\tau = T_c/2$ (say $H_{0.5}$), for the conventional detector, and the worst positive hypothesis with $\tau = T_c/4$ (say $H_{0.75}$) for the devised over-sampled detector. In the conventional technique, the "middle" hypothesis lies at $\tau = T_c/4$ far from the correct timing offset $\tau=0$ (say $H_{0.75}$), while the "middle" positive hypothesis for the proposed approach is $\tau = T_c/8$ far from the correct offset $\tau=0$ (say $H_{0.875}$). It should be noted that the half-chip offset ($\tau = T_c/2$) correlation could have a non-negligible impact on the acquisition performance. Nevertheless, in full agreement with the approach by Jia-Chin Lin [8], detecting the half-chip correlation sample ($H_{0.5}$) is actually a metastable state that may sometimes lead to false-alarm conditions, but such conditions can be very easily corrected in the next test immediately. The mean acquisition time A_T of a serial search procedure over q cells (q>>1) is related to these probabilities according the approximate expression [4−5]:

$$A_T \cong q\cdot[L + P_{fa}T_P]\frac{2-P_D}{2P_D} \qquad \textbf{(2)}$$

where $L=WDT_c$ is the test's duration for each code offset candidate and T_P is the penalty time for an erroneous acquisition while the signal does not actually exist. As a consequence, the ratio of the mean acquisition times, say A_{T1} and A_{T2}, of two generic CFAR detectors with the same duration L, that is:

$$\frac{A_{T1}}{A_{T2}} \cong \frac{(2-P_{D1})\cdot P_{D2}}{P_{D1}\cdot(2-P_{D2})} \qquad \textbf{(3)}$$

is able to directly evidence the approximate gain in saving time (on the average) of the latter against the former methods when the same signal data blocks are available.

In the following of this paper, we are going to compare the performance of the two methods with respect to the "middle" synchronization conditions, considered here as representative of the average operating conditions. The results of our computer simulations, conversely assuming a uniform distribution of the timing offset, are going to show that the "middle" case (defined for one given "middle" offset) is representative of such a random jitter of actual timing offsets.

3. Application to Initial Synchronization in UMTS and Results

In this section, we aim to show that the analyzed methods for code synchronization are applicable to the first stages of initial cell search in the cellular UMTS system. In particular, we are going to evidence that the analytic expressions, reported in the previous sections, are able to predict the achievable gain on the error probability and the mean acquisition time of the over-sampled versus the conventional method. The same scenarios as in [2] of

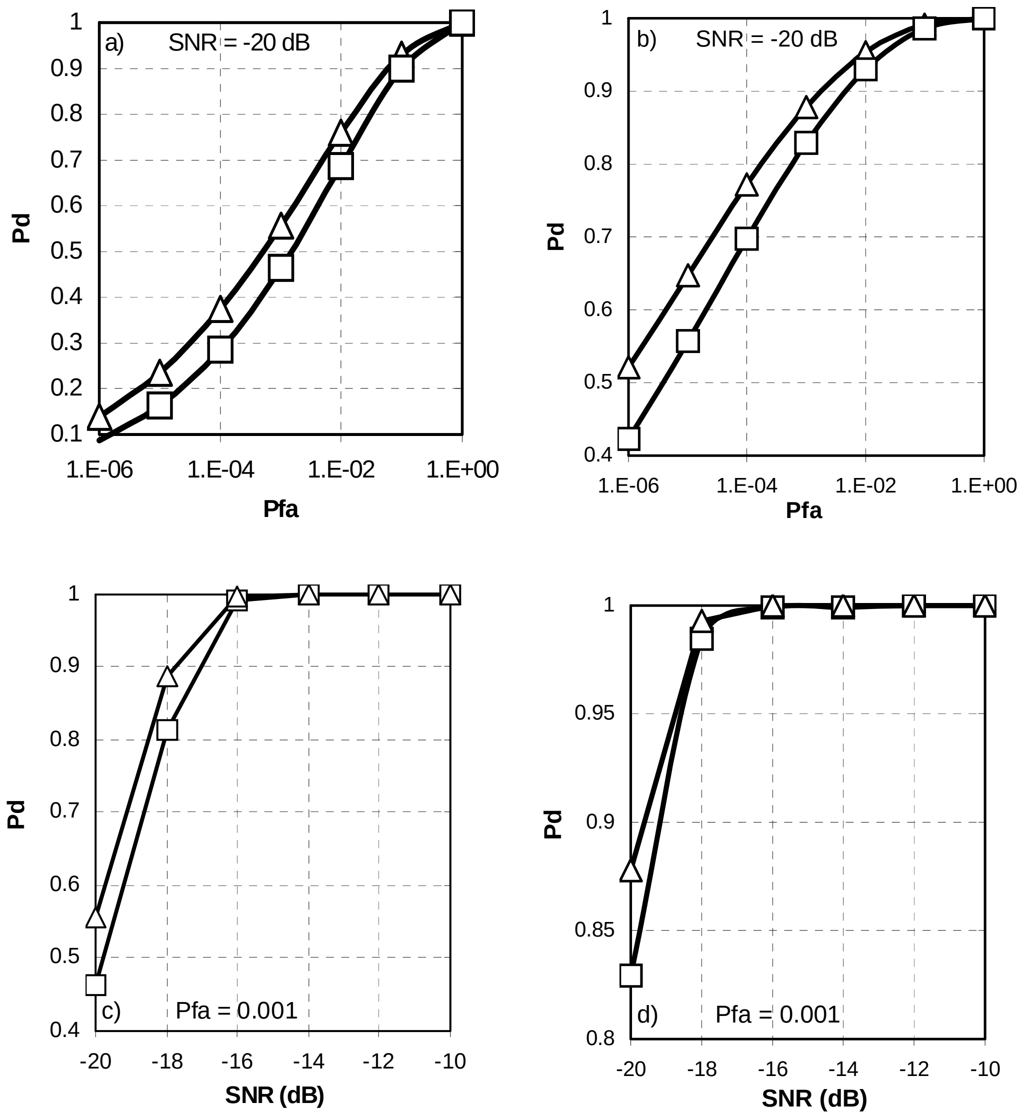

Figures 1a-d. Analytic probability of detection versus the probability of false alarm (top: a,b) and the SNR value per chip (bottom: c,d) in the "middle" offset case for a frequency uncertainty of 20 kHz (left: a,c) and 200 Hz (right: b,d), matching the achieved performance of the conventional (squares) and over-sampled (triangles) methods for W=60 blocks of 64 chips (10 ms).

cell search have been extensively studied. The frequency errors of 20 kHz and 200 Hz, typical of the initial and the target cell search, have been considered. In IMT2000/ UMTS [2], the pilot symbols available for code synchronization consist of 256 consecutive chips per slot (each slot is made of 2560 chips in total). The cross-correlation performance of one and more groups of frames (each made of 15 slots, i.e. 10 ms), as far as the overall synchronization time in flat fading channels, has been analyzed. If one directly chooses D=256, the large frequency error during the initial search results in a large incoherence loss, especially in the initial search. This problem

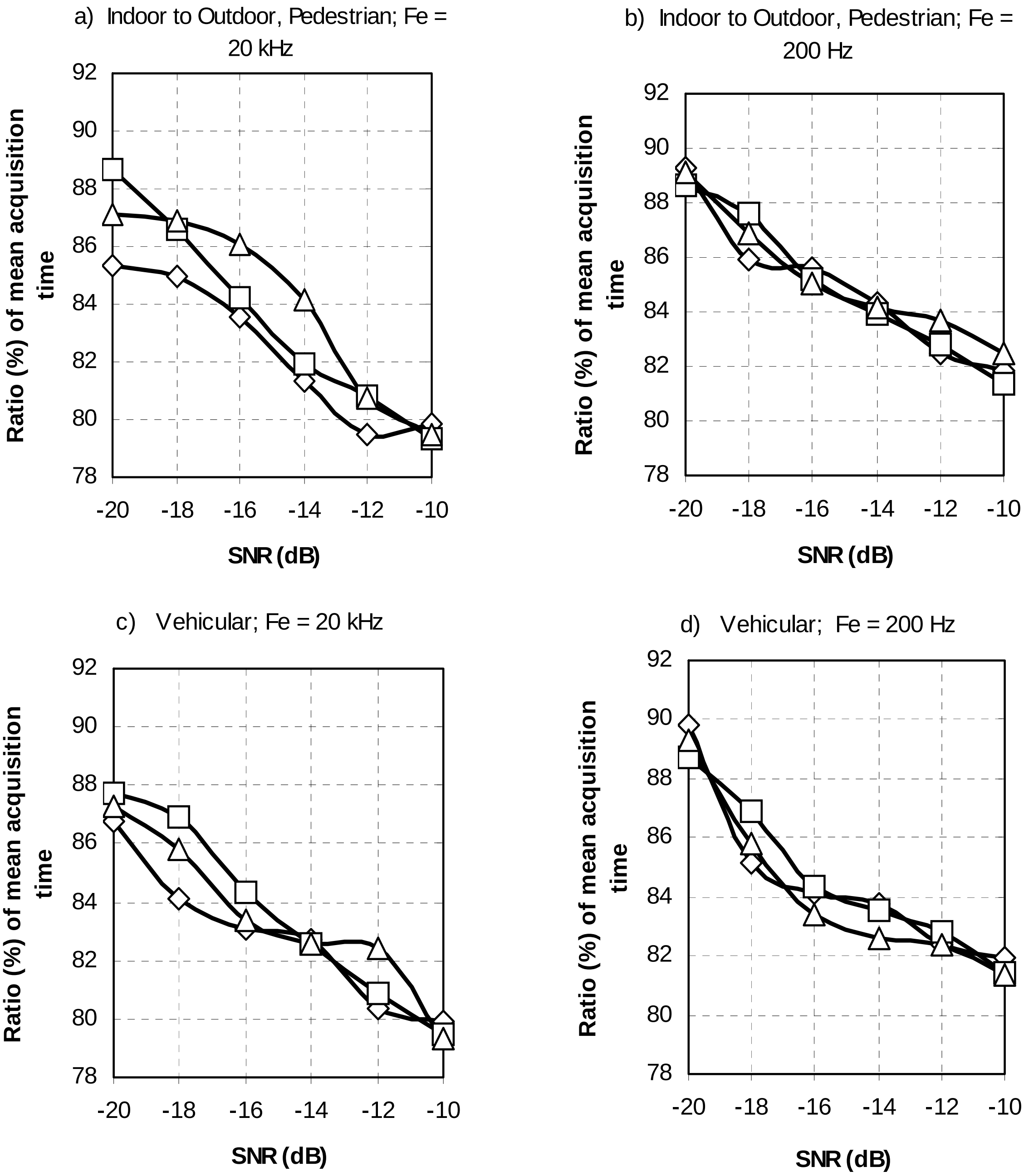

Figures 2a-d. Ratio of the experimental mean acquisition time of fractional and conventional procedures in the three initial stages (stage 1: diamonds; stage 2: squares; stage 3 triangles) versus the SNR per chip for pedestrian (top: a,b) and vehicular (bottom: c,d) scenarios with a random timing jitter for a frequency uncertainty of 20 kHz (left: a,c) and 200 Hz (right: b,d).

is solved by partial symbol despreading [2], using blocks of D=64 contiguous chips and non-coherent combining. In particular, the first stage of initial code synchronization provides a number of possible candidates of code offsets to the following one [2]. As a consequence, a sequential test can be implemented for such a purpose, performed like the procedure described in the former part of this paper. In the following (second and third) stages, only the most reliable code candidate is detected and finally processed by the frequency acquisition system [2].

The probability of detection in the “middle” synchronization case of the timing offset, defined in the previous section, is derived from the analytic expressions and depicted in figures 1a-d versus the probability of fal-sealarm and the SNR for the two methods, in order to assess the validity of the over-sampled testing procedure in the presence of frequency uncertainties. The results of computer simulations, obtained with a uniformly distributed random jitter, have confirmed such trend. For sake of comparison, we have assumed the same typical pedestrian and vehicular scenarios reported in [2]. In particular, a uniformly distributed random timing jitter has been considered while the channel is affected by flat fading and three paths have been simulated, depending on the kind of scenario. Namely, pedestrian (speed: 3 Km/h): the first path is 0 dB with delay =0 ns, the second one 0 dB and delay=976 ns, third one 0 dB and delay =20000 ns; vehicular (speed: 120 km/h): the main path is 0 dB with delay 0 ns, the second one -3 dB and delay =260 ns and the third one is -6 dB and delay =521 ns. Two possible constant frequency errors in the initial and target search [2] procedure (namely, 20 kHz and 200 Hz) are considered. In particular, the figures 2a-d show the ratio of the mean acquisition time of the two methods versus the SNR per chip, obtained by Monte-Carlo simulations of the two reference wireless channels of [2] for P_{fa}=0.001, for the three initial stages of the serial code acquisition in UMTS.

Moreover, the same authors of this paper showed in [13], by extensive computer simulations, that the new scheme outperforms the conventional approach analyzing also the overall acquisition performance of the scrambling code, then including all the three steps of the initial synchronization procedure (before frequency acquisition). The authors, in [13], evidenced the significant real-time saving of the mean acquisition time (from 12% to 21%) of the suggested procedure, compared to the conventional technique, in the presence of multi-path channels with flat fading and frequency inaccuracy. In practice, the benefits on the mean acquisition time of using two samples per chip, since the first stage of code synchronization, are twofold: first, the cross-correlation between the received signal and the code’s candidates are better estimated, then increasing the testing power of stage *1* (i.e. probability of correct detection for a constant false alarm rate); second, the timing error provided to the stages *2* and *3* is ideally the half of the conventional technique, being maximized by one fourth of the chip period.

4. Conclusions

This paper has addressed algorithms for initial code synchronization by sequential cell search, suited for application to the first three stages of the IMT2000/UMTS cellular wireless access system, i.e. initial cell search before frequency acquisition. The basic testing method, based on one sample per chip, has been herein matched to an improved technique based on a fractional chip sampling (and processing) that operates at twice the chip rate, according to the Nyquist criterion. The simulation analyses have evidenced a significant reduction of the mean acquisition time by the suggested procedure, compared to the conventional technique. In perspective, exploiting the half-chip offset correlation (by devising new well-performing testing variables) could further improve these schemes.

5. Acknowledgments

The authors wish to thank Prof. A. Neri and Dr. M. Carli of the University of Roma Tre for their support on the preliminary trials of numerical analysis and further discussions on application to 3G Mobile Systems.

6. References

[1] T. Ojanperä and R. Prasad, “An overview of air interface multiple access for IMT2000/UMTS,” IEEE Communication Magazine, Vol. 36, pp. 82–95, September 1998.

[2] Y. Pin, E. Wang, and T. Ottosson, “Cell search in W-CDMA,” IEEE Journal on Selected Areas in Communications, Vol. 18, No. 8, pp. 1470–1482, August 2000.

[3] R. L. Pickholtz, D. L. Schilling, and L. B. Milstein, “Theory of spread spectrum communications. A tutorial,” IEEE Transactions on Communications, Vol. 30, pp. 855–884, May 1982.

[4] D. M. DiCarlo and C. L. Weber, “Multiple dwell serial search: Performance and application to direct-sequence code acquisition,” IEEE Transactions on Communications, Vol. 31, pp. 650–659, May 1983.

[5] G. Giunta, “Generalized Q-Functions for application to non-coherent serial detection of spread-spectrum communication signals,” IEEE Transactions on Signal Processing, Vol. 48, No. 5, pp. 1506–1513, May 2000.

[6] J.-C. Lin and C.-Y. Lin, “Non-coherent sequential PN code acquisition using sliding correlation in DS/SS,” In-

ternational Conference on Communication, ICC'2000, pp. 341–345, 2000.

[7] J.-C. Lin, "Noncoherent sequential PN code acquisition using sliding correlation for chip-asynchronous direct-sequence spread-spectrum communications," IEEE Transactions on Communications, Vol. 50, No. 4, pp. 664–676, April 2002.

[8] J.-C. Lin, "Differentially coherent PN code acquisition based on a matched filter for chip-asynchronous DS/SS communications", IEEE Transactions on Vehicular Technology, Vol. 51, No. 6, pp. 1596–1599, November 2002.

[9] J.-C. Lin, "Differentially coherent PN code acquisition with full-period correlation in chip-synchronous DS/SS receivers," IEEE Transactions on Communications, Vol. 50, No. 5, pp. 698–702, May 2002.

[10] A. Mantravadi and V. V. Veeravalli, "On chip-matched filtering and discrete sufficient statistics for asynchronous band-limited CDMA systems," IEEE Transactions on Communications, Vol. 49, No. 8, pp. 1457–1467, August 2001.

[11] E. Dahlman, P. Beming, J. Knutsson, F. Ovesjo, M. Persson, and C. Roobol, "WCDMA-The radio interface for future mobile multimedia communications," IEEE Transactions on Vehicular Technology, Vol. 47, pp. 1105–1118, November 1998.

[12] W.-H. Sheen, J.-K. Tzeng, and C.-K. Tzou, "Effects of cell correlations in a matched filter PN code acquisition for direct-sequence spread spectrum systems," IEEE Transactions on Vehicular Technology, Vol. 48, No. 3, pp. 724–732, May 1999.

[13] F. Benedetto, M. Carli, G. Giunta, and A. Neri, "Performance benefits of fractional sampling in the initial code synchronization for the wireless access of 3G mobile communications," IEEE International Vehicle Technology Conference, VTC 2005-Spring, Stockholm, Sweden, June 2005.

Engineering, 2009, 1, 1-54
Published Online June 2009 in SciRes (http://www.SciRP.org/journal/eng/).

Embedded Control of LCL Resonant Converter Analysis, Design, Simulation and Experimental Results

S. Selvaperumal[1], C. Christober Asir Rajan[2]
[1]*Department of EEE, Mepco Schlenk Engineering College, Sivakasi, India*
[2]*Department of EEE, Pondicherry Engineering College, Pondicherry, India*
Email: [1]*perumal.om@gamil.com*, [2]*asir_70@pec.edu*
Received April 3, 2009; *revised May* 19, 2009; *accepted May* 22, 2009

Abstract

The Objective of this paper is to give more insight into CCM Operation of the LCL Converter to obtain optimum design using state-space analysis and to verify the results using PSPICE Simulation for wide variation in loading conditions. LCL Resonant Full Bridge Converter (RFB) is a new, high performance DC-DC converter. High frequency dc-dc resonant converters are widely used in many space and radar power supplies owing to their small size and lightweight. The limitations of two element resonant topologies can be overcome by adding a third reactive element termed as modified series resonant converter (SRC). A three element resonant converter capable of driving voltage type load with load independent operation is presented. We have used embedded based triggering circuit and the embedded 'C' Program is checked in Keil Software and also triggering circuit is simulated in PSPICE Software. To compare the simulated results with hardware results and designed resonant converter is 200W and the switching frequency is 50 KHz.

Keywords: Continuous Current Mode, High-frequency Link, MOSFET, Zero-Current Switching, Resonant Converter

1. Introduction

In Converter applications solid-state devices are operated at very high frequency. So the switching losses are more than the conduction losses [1] and it becomes a major cause of poor efficiency of the converter circuit [2,3]. This leads to the search of a converter that can provide high efficiency [4], lower component stress [5], high power, high switching frequency, lightweight as well as low cost and high power operation [6]. In order to keep the switching power losses low and to reduce the problem of EMI, the resonant converter is suggested [7−9].

The resonant converter is a new high performance DC-DC converter [10]. A resonant converter can be operated either below resonant (leading p.f) mode or above resonant (lagging p.f) mode. The most popular resonant converter configuration is series resonant converter (SRC), parallel resonant converter (PRC) and series parallel resonant converter (SPRC). A SRC has high efficiency from full load to very light loads [11,12]. Where as a PRC has lower efficiency at reduced loads due to circulating currents [13,14].

The limitations of two element resonant topologies can be over come by adding a third reactive element, termed as modified SRC. SRC has voltage regulation problems in light load conditions [15,16]; to over come this problem the modified SRC is presented. The LCL-resonant converter using voltage source type load has nearly load independent output voltage under some operating conditions [17]. These converters are analyzed by using state-space approach. Based on this analysis, a simple design procedure is proposed. Using PSPICE software simulates the LCL-Resonant Full Bridge Converter. The proposed results are improved power densities in air borne applications.

2. Modified Series Resonant Converter

A Series Resonant Full Bridge Converter (SRC) modified by adding an inductor in parallel with the transformer primary is presented. This configuration is referred to as an "LCL Resonance Full Bridge Converter". A three element (LCL) Resonance Full Bridge Converter capable of driving voltage type load with load independent operation is analyzed. In such a converter has load independent characteristics, there is no analysis or design procedure available. It is shown in this project that these type of converter requires a very narrow range of frequencies control from full load to very light loads and can operate with load short circuit while processing the desirable features of the SRC. The resonance converter operating in the above resonance (lagging power factor) mode has a number of advantages (e.g. No need for lossy snubbers and di/dt limiting inductors). Therefore, the proposed converter configuration in the above resonance mode, State-space approach is used for the converter analysis. A modified SRFB Converter with capacity output filter has been presented.

3. Circuit Description

The resonant tank of this converter consists of three reactive energy storage elements (LCL) as opposed to the conventional resonant converter that has only two elements. The first stage converts a dc voltage to a high frequency ac voltage. The second stage of the converter is to convert the ac power to dc power by suitable high frequency rectifier and filter circuit. Power from the resonant circuit is taken either through a transformer in series with the resonant circuit (or) across the capacitor comprising the resonant circuit as shown in Fig.1. In both cases the high frequency feature of the link allows the use of a high frequency transformer to provide voltage transformation and ohmic isolation between the dc source and the load.

In Series Resonant Converter (SRC), the load voltage can be controlled by varying the switching frequency or by varying the phase difference between the two inverts where the switching frequency of each is fixed to the resonant frequency. The phase domain control scheme is suitable for wide variation of load condition because the output voltage is independent of load.

The basic circuit diagram of the full bridge LCL resonant converter with capacitive output filter is shown in Figure 1.

The major advantages of this series link load SRC is that the resonating blocks the DC supply voltage and there is no commutation failure if MOSFET are used as switches. Moreover, since the dc current is absent in the primary side of the transformer, there is no possibility of current balancing. Another advantage of this circuit is that the device currents are proportional to load current. This increases the efficiency of the converter at light loads to some extent because the device losses also decrease with the load current. Close to the resonant frequency the load current becomes maximum for a fixed load resistance. If the load gets short at this condition very large current would flow through the circuit. This may damage the switching devices. To make the circuit short circuit proof, the operating frequency should be changed.

The filter circuit has some disadvantage. It is a capacitor input filter and the capacitor must carry large ripple current. It may be as much as 48% of the load current. The disadvantage is more severe for large output current with low voltage. Therefore, this circuit is suitable for high voltage low current regulators.

4. State – Space Analysis

4.1. Assumptions in State Space Analysis

The following assumptions are made in the state spare analysis of the LCL Resonant Full Bridge Converter.

1) The switches, diodes, inductors, and capacitors used are ideal.

2) The effect of snubber capacitors is neglected.

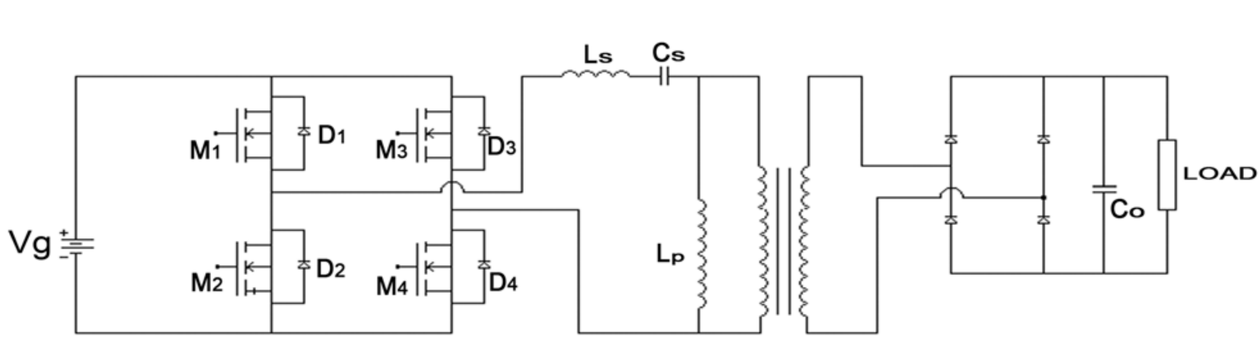

Figure 1. DC- DC converter employing LCL full bridge operating in CCM.

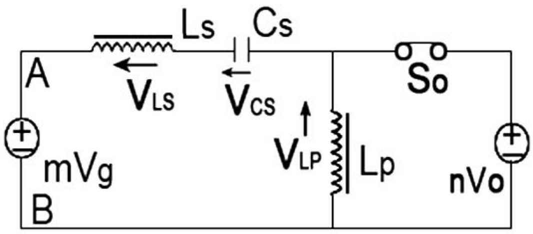

Figure 2. Equivalent circuit model of LCL RFBC.

3) Losses in the tank circuit and neglected.

4) Dc supply used is smooth.

5) Only fundamental components of the waveforms are used in the analysis.

6) Ideal hf transformer with turns ration n =1.

The equivalent circuit shown in Figure 2 is used for the analysis. The vector space equation for the converter is:

$$X = AX + BU \quad \textbf{(1)}$$

where m and n take values as shown in Table 1 representing different modes of continuous and discontinuous conduction.

However, in the discontinuous conduction mode 7, the converter operates like a simple SRC with resonant frequency, fo and $i_{Ls}=i_{Lp}$. It is interesting to note that in all six continuous conduction modes, the voltage V_{LP} is clamped and the current i_{Lp} is independent of the other two state variables. As a result, the 3rd order matrix (1) can be reduced to second order equation for which the solutions are readily available [2].

The state equation describing period $tp_{-1} < t < tp$

$$mVg = Ls\,(di_{Ls}/dt) + nVo – Vc \quad \textbf{(2)}$$

$$(di_{Ls}/dt) = (m/Ls)Vg - (nVo/Ls) - (1/Ls)Vc \quad \textbf{(3)}$$

$$(dV_{Cs}/dt) = (1/Cs)\ i_{Ls} \quad \textbf{(4)}$$

$$(di_{Lp}/dt) = (nVo/Lp) \quad \textbf{(5)}$$

State matrix: X = AX + BU

$$\frac{d}{dt}\begin{pmatrix} i_{Ls} \\ V_{cs} \\ i_{Lp} \end{pmatrix} = \begin{pmatrix} 0 & (-1/L_s) & 0 \\ 1/C_s & 0 & 0 \\ 0 & 0 & 0 \end{pmatrix} + \begin{pmatrix} i_{Ls}(t) \\ V_{cs}(t) \\ i_{Lp}(t) \end{pmatrix} \begin{pmatrix} (m/L_s) & (-n/L_s) \\ 0 & 0 \\ 0 & n/L_p \end{pmatrix} \begin{pmatrix} V_g \\ V_o \end{pmatrix} \quad \textbf{(6)}$$

Table 1. Different mode of operation.

Mode	m	n	So	id
1	+1	+1	ON	> 0
2	0	+1	ON	> 0
3	-1	+1	ON	> 0
4	+1	-1	ON	> 0
5	0	-1	ON	> 0
6	-1	-1	ON	> 0
7	0	-	OFF	0
8	+1	-	OFF	0
9	-1	-	OFF	0

The sum of the zero input response and the zero state response.

$$X(t) = [\ \phi(t)\ [X(o)]\ ] + L^{-1}\ (\phi\ (s)\ B[U\ (s)\ ] \quad \textbf{(7)}$$

The transition matrix

$$\phi(t) = L^{-1}\ [\phi\ (S)] \quad \textbf{(8)}$$

$$= L^{-1}\ [(SI\text{-}A)\ \ -1] \quad \textbf{(9)}$$

$$(S\,I - A) = S_3 + S\ ώ2$$

$$= S\ (S_2 + ώ2) \quad \textbf{(10)}$$

where $ώ=1/\sqrt{LC}$

$$Adj[SI - A] = \begin{pmatrix} S^2 & -S/C & 0 \\ S/Ls & S^2 & 0 \\ 0 & 0 & S^2+ώ^2 \end{pmatrix}$$

$$= \frac{1}{S(S^2+ώ^2)}\begin{pmatrix} S^2 & -S/C & 0 \\ S/Ls & S^2 & 0 \\ 0 & 0 & S^2+ώ^2 \end{pmatrix}$$

$$\phi(S) = \begin{pmatrix} S/S^2+ώ^2 & -1/Cs(S^2+ώ^2) & 0 \\ 1/Ls(S^2+ώ^2) & S/(S^2+ώ^2) & 0 \\ 0 & 0 & 1/S \end{pmatrix}$$

$$\phi(t) = \begin{pmatrix} \cos ώt & -\sin ώ_1 t/Cs\,ώ_1 & 0 \\ \sin ώ_1 t/Ls\,ώ_1 & \cos ώ_1 t & 0 \\ 0 & 0 & 1 \end{pmatrix}$$

$\therefore$ Zero state response, $= L^{-1}\ [(\phi\ (s)\ B\ [U\ (s)]]$

$$= L^{-1}\begin{pmatrix} S/S^2+\acute{\omega}^2 & -1/Cs(S^2+\acute{\omega}^2) & 0 \\ 1/Ls(S^2+\acute{\omega}^2) & S/(S^2+\acute{\omega}^2) & 0 \\ 0 & 0 & 1/S\end{pmatrix}\begin{pmatrix} m/Ls & -n/Ls \\ 0 & 0 \\ 0 & n/Lp\end{pmatrix}\begin{pmatrix} Vg/S \\ \\ Vo/S\end{pmatrix} = \begin{pmatrix}(mVg-nVo)/Zos\sin\acute{\omega}_1(t-t_{p-1}) \\ mVg-nVo[1-\cos\acute{\omega}_1(t-t_{p-1})] \\ Vo/Lp(t-t_{p-1})\end{pmatrix}$$

$$x(t) = [\ \phi(t)[x(o)] + L^{-1}[\phi(s)B[U(s)]]$$

$$\begin{pmatrix} i_{Ls}(t) \\ V_{cs}(t) \\ i_{Lp}(t)\end{pmatrix} = \begin{pmatrix} \cos\acute{\omega}_1 t(t-t_{p-1}) & \sin\acute{\omega}_1(t-t_{p-1})/Ls\acute{\omega}_1 & 0 \\ -\sin\acute{\omega}_1(t-t_{p-1})/Cs\acute{\omega}_1\cos\acute{\omega} & 1(t-t_{p-1}) & 0 \\ 0 & 0 & 1\end{pmatrix}\begin{pmatrix} i_{Ls}(t-t_{p-1}) \\ V_{cs}(t-t_{p-1}) \\ i_{Lp}(t-t_{p-1})\end{pmatrix} + \begin{pmatrix}(mVg-nVo)/Zos\sin\acute{\omega}_1(t-t_{p-1}) \\ mVg-nVo[1-\cos\acute{\omega}_1(t-t_{p-1})] \\ nVo/Lp(t-t_{p-1})\end{pmatrix}$$

$$I_{Ls}(t) = \cos\acute{\omega}1\,(t-t_{p-1})\,I_{Ls}(t_{p-1}) + (\sin\acute{\omega}\,1(t-t_{p-1})/Ls\,\acute{\omega}1)\,VCs(t_{p-1}) + ((mVg-nVo)/Zos)\sin\acute{\omega}_1(t-t_{p-1}) \quad \textbf{(11)}$$

$$I_{Ls}(t) = I_{Ls}(t_{p-1})\cos[\acute{\omega}1(t-t_{p-1})] + [(mVg - nVo - Vcs(t_{p-1}))/Zos]\sin[\acute{\omega}_{os}(t-t_{p-1})] \quad \textbf{(12)}$$

$$V_{cs}(t) = i_{Ls}(t_{p-1})\,Zos\sin[\acute{\omega}_{os}(t-t_{p-1})] + (m\,Vg - nVo)\,[1-\cos\acute{\omega}_1(t-t_{p-1})] + Vcs(t_{p-1})\cos[\acute{\omega}_1(t-t_{p-1})] \quad \textbf{(13)}$$

$$i_{Lp}(t) = i_{Lp}(t_{p-1}) + (n/Lp)\,Vo\,(t-t_{p-1}) \quad \textbf{(14)}$$

where, t_{p-1} is the time at the start of any, ccm. t_p is the time at the end of the same ccm.

Similarly, the solutions for the discontinuous conduction mode are: $i_{Ls} = i_{Lp}$.

$$i_{Ls}(t) = i_{Lp}(t) = i_{Ls}(t_{p-1})\cos[\acute{\omega}_o(t-t_{p-1})] + [(mVg - Vcs(t_{p-1})/Zo)\sin(t-t_{p-1})] \quad \textbf{(15)}$$

$$V_{Cs}(t) = i_{Ls}(t_{p-1})\,Zo\sin[\acute{\omega}_o(t-t_{p-1})] + mVg[1-\cos[\acute{\omega}_o(t-t_{p-1})]] + Vcs(t_{p-1})\cos(\acute{\omega}_o(t-t_{p-1})] \quad \textbf{(16)}$$

where D is the duty cycle = $\tau / (T_s / 2)$

From Mo equation, it can be concluded that the output voltage is not dependent on the load resistance and converter gain follows a sine function. These results are completely validated experimentally by plotting the variation of Mo with duty ratio. At the optimum normalized switching frequency f_{no}, m_o is independent of variations in the load resistance for all pulse widths. The deviation increases with reducing values of load resistance or increasing values of load current for the given voltage. This arises because of sensing resistance of 0.5 Ω used in series with the resonant element for monitoring its and also finite resistance offered by diodes and MOSFET'S in conduction. In order to maintain the output voltage constant at desired value against the variations in the load resistance and supply voltage variations, the pulse width has to be changed in a closed-loop manner. However, the required change in pulse width to maintain constant output voltage against load variations and constant input voltage is very small.

5. Design Procedure

5.1. Design: (Operating Switching Frequency = 50khz)

It is desired to design the converter with the following specifications:

1) Power output =200W
2) Minimum input voltage =100V
3) Minimum output voltage =125V
4) Maximum load current = 1.6 A
5) Maximum overload current = 4A
6) Inductance ratio (K_L) = 1

The hf transformer turns ratio assumed to be unity.

The load resistance:

R_L= Maximum output voltage / maximum output current.

= 100 / 1.6
= 62.5
≅ 63Ω

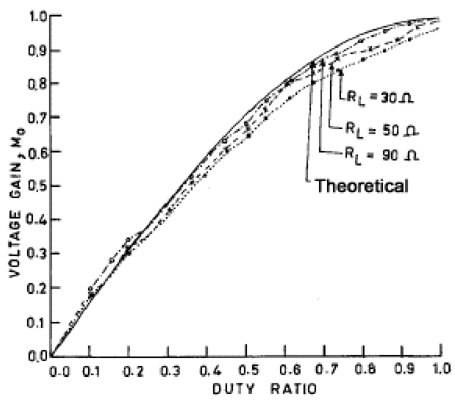

Figure 3. Variation of voltage gain with the duty ratio.

The input rms voltage to the diode bridge:

$$(V_{Lp}) = 2\sqrt{2}\, V_0/\pi \quad \textbf{(17)}$$

The input rms current at the input of the diode bridge

$$= [\pi/2\sqrt{2}\,]I_0 \quad \textbf{(18)}$$

The reflected ac resistance on the input side of the diode bridge is

$$R_{ac} = V_{LP} / I_d \quad \textbf{(19)}$$

$$V_{LP} / I_d = \left(2\sqrt{2}\, V_0/\pi\right) / \left(\pi/2\sqrt{2}\right) I_0$$

$$= \left(2\sqrt{2}\, V_0 \times 2\sqrt{2}\,\right) / \pi \times \pi \times I_0$$

$$V_{LP} / I_d = 8\, V_0 / \pi^2 I_0 \quad \textbf{(20)}$$

For maximum power output

$$\sqrt{L_s / C_s} = 8 R_L / \pi^2 \quad \textbf{(21)}$$

$$= 8 \times 75 / \pi^2$$

$$= 60.8\Omega$$

Since the switching frequency is 50 KHz

$$1/2\, \sqrt{L_s / C_s} = 50 \times 10^3$$

$$\sqrt{L_s} = 60.8\sqrt{C_s}$$

$$\sqrt{C_s} = \sqrt{L_s} / 60.8 \quad \textbf{(22)}$$

$$1/2\, \sqrt{L_s} \times \sqrt{L_s} / 60.8 = 50 \times 10^3$$

$$60.8 / 2\pi \times L_s = 50 \times 10^3$$

from this

$$f_o = 1 / \left[2\Pi\sqrt{(L_S + L_P)C_S}\,\right] \quad \textbf{(23)}$$

$$L_s = 185\mu\text{H}$$

$$C_s = 0.052\mu F$$

From the availability of the capacitors, is in chosen as 0.05µF.The inductance Ls is obtained as 202µH. In the experimental setup, the actual inductance used is 200µH, which is close to the designed value.

6. Simulation of LcLResonant Full Bridge Converter

The simulated circuit of LCL Resonant Full Bridge Converter is shown in Figure 4.

Power MOSFET, are used as switches M1, M2, M3 and M4 in the converters for an operating frequency of 50KHz. The anti parallel diodes, D1, D2, D3 and D4 connected across the switches are not need because they have inherent anti-parallel body diodes. The forward current and the reverse voltage ratings of the diode are the same as the current and voltage ratings of the MOSFET. The internal diode is characterized by forward voltage drop and reverse recovery parameters like a discrete diode.

The resistor, inductor, capacitors, the power diodes and the power MOSFET'S are represented by their PSPICE Model. MOSFET IRF 330 is selected as the switching device which meets the peak current and voltage requirements.

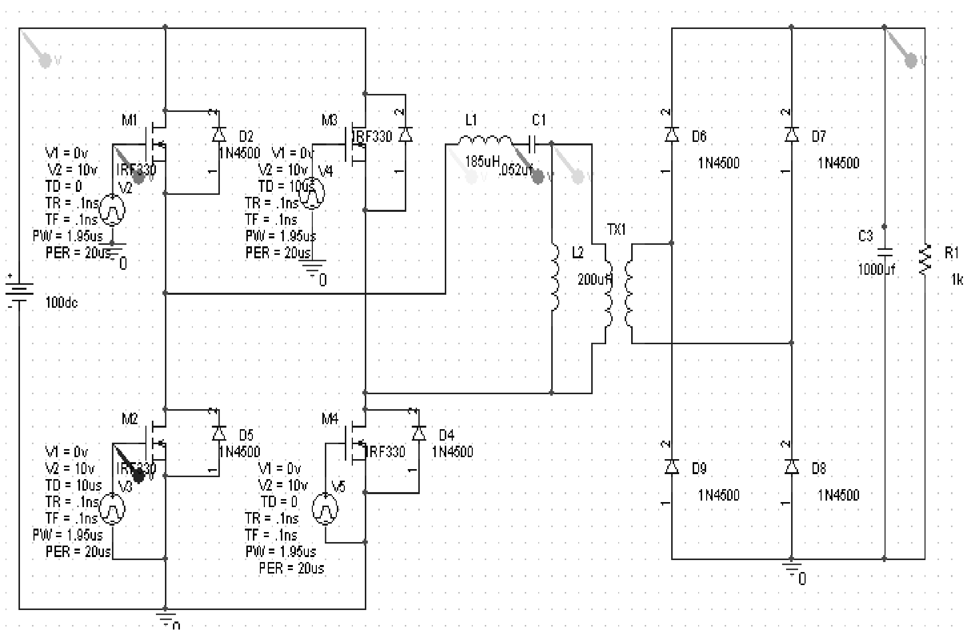

Figure 4. LCL resonant converter circuit.

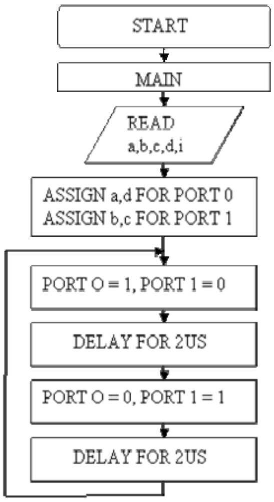

Figure 5. Flow chart for embedded controller 89C51.

DIN 4001 is chosen as the power diode which meets the requirements. Using the datasheets for the POWER MOSFET IRF 330 and the power diode – DIN 4001, given in appendix (A), the various parameters of the model are calculated and used in the circuit file. The simulated waveforms of V_{LS}, V_{LP}, V_{CS}, I_{LP}, I_{CS}, V_{AB}, and V_O found to agree with the analytical results to an appreciable degree.

7. About Keil

It is software, which is used to check the embedded C program and results that whether the program is correct or not, which is shown in Figure 6.

8. Conclusions

A modified SRC which employs a LCL-Resonant Full Bridge Converter circuit and operating above resonance (lagging power factor) mode has been presented. This converter with a voltage type load shows it provide load independent operation above the resonance frequency. So, the switching power losses are minimized. This new DC-DC converter has achieved improved power densities for air borne applications. This converter analyzed by using state space analysis is presented. The LCL resonant full bridge converter is potentially suited for applications such as space and radar high voltage power supplies with the appropriate turns ratio of high frequency transformer. Another good feature of this converter is that the converter operation is not affected by the non idealities of the output transformer (magnetizing inductance) because of the additional resonance inductor L_P.

Table 2. Comparison of PSPICE simulation, theoretical & experimental results obtained from the model for a 133W, 50 KHZ DC-DC LCL resonant converter.

(Ls = 185µH, Cs = 0.052 µF, C = 0.0087 µF, Lp = 200 µH, Co = 1000 µF, Load L=10µH, E=10V, Input Voltage = 100 V)

Load Resistance (Ohm)	Load Current (ampere)	Simulation Result (Volts)	Theoretical Results (Volts)	Experimental Results (Volts)
1	1.5625	127.9	125	127
20	1.556	128.5	125	127.5
30	1.554	128.7	125	128.1
50	1.55	129	125	128.7
100	1.548	129.2	125	129
200	1.548	129.2	125	129
300	1.548	129.2	125	129
400-1K	1.548	129.2	125	129

From Table 2, it is known that the hardware result for open loop LCL resonant converter varies from 127 V to 129V. But theoretical result should not go beyond 125V. So there is a scope for future extension.

The LCL-resonant full bridge converter is simulated by using PSPICE software. The simulation is carried out for 120µS which is equivalent to six cycles, and simulation results are obtained. The triggering circuit of LCL-RFB converter is also simulated by using PSPICE software. The hardware implementation of triggering circuit and the power circuit are obtained and the results are compared to the simulation results.

9. Scope of Future Extension

Analysis, design, simulation and fabrication of closed loop LCL resonant converter.

Comparison result of open loop and closed loop LCL resonant converter.

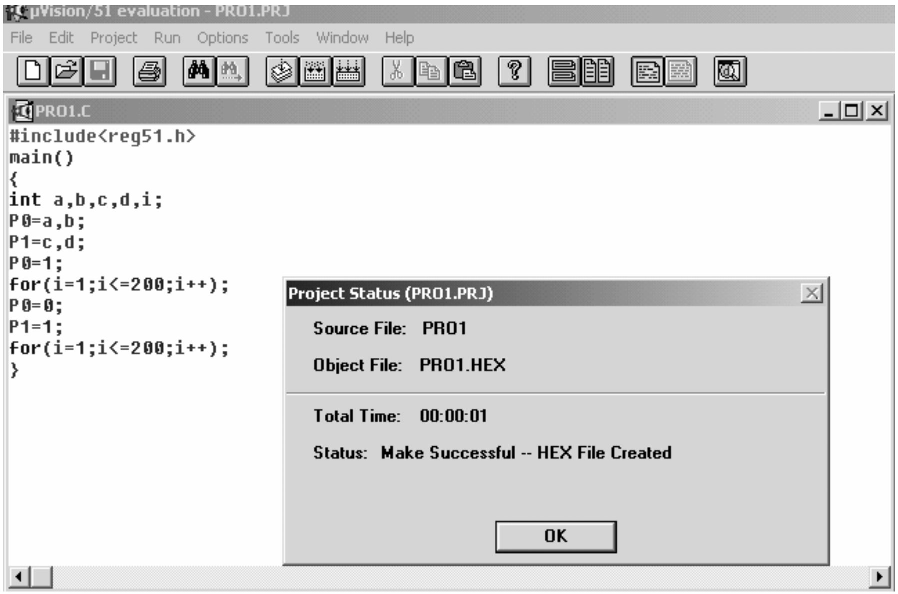

Figure 6. Program result for embedded controller output using Keil software.

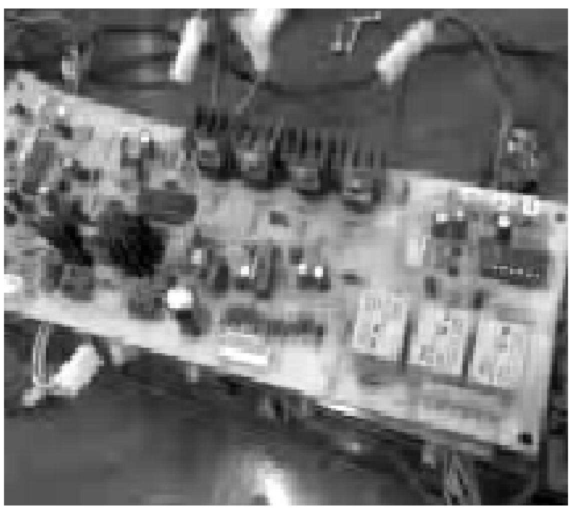

Figure 7. Prototype model -embedded control of LCL resonant converter.

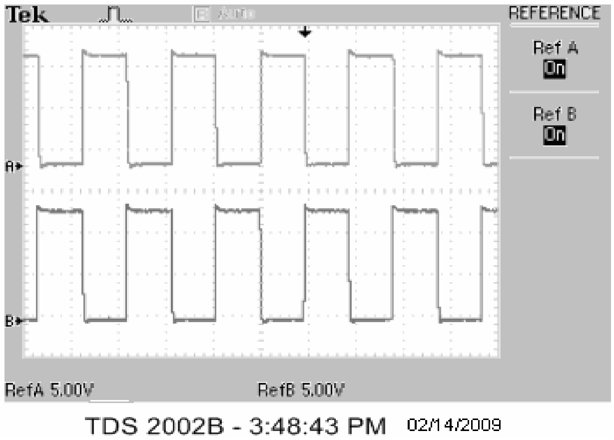

Figure 8. Experimental results of gate voltage (X axis represents time in micro seconds and Y axis represents Gate Voltage. The amplitude is 5V. If M1 & M4 conduct 0-20μs then M1 & M4 are in OFF State. If M2 & M3 conduct 20μs - 40μs then M2 & M3 are in OFF State).

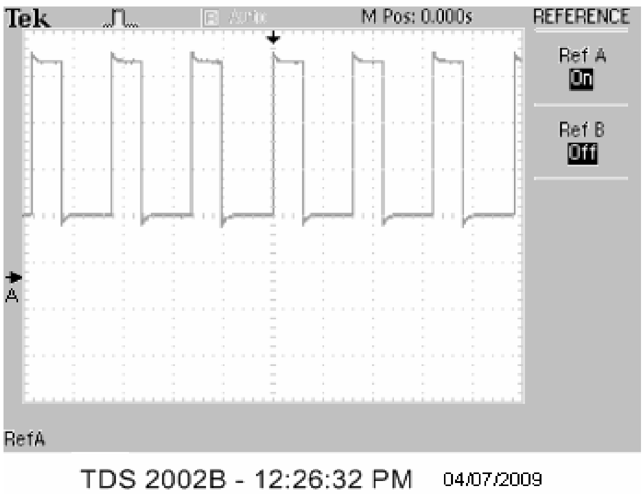

Figure 9. Experimental results obtained from the model for a 133W, 50 KHZ DC-DC LCL Resonant Converter output voltage = 127. 5 V (Ls = 185μH, Cs = 0.052 μF, C = 0.0087 μF, Lp = 200 μH, R= 20Ω, Co = 1000 μF, Load L=10μH, E=10V, Input Voltage = 100 V).

10. References

[1] A. K. S. Bhat, "Analysis and design of a modified series resonant converter," IEEE Transactions, Power Electronics, Vol. 8, pp. 423–430, October 1995.

[2] A. K. S. Bha, "Analysis and design of LCL-Type series resonant converter," IEEE INTELEC, pp. 172–178, 1994.

[3] A. K. S. Bhat, "Analysis and design of a fixed-frequency LCL-Type series resonant converter with capacitive output filter," IEE PROC-Circuits Devices System, Vol. 144, No. 2, April 1997.

[4] R. Sevverns, "Topologie for three element resonant converter," in IEEE Applied Power Electronics, Conference Record, pp. 712–722, March 1990.

[5] E. G. Schmidtner, "A new High-Frequency resonant Converter topology," in High Frequency Power Conversion Conference Record, pp. 390–403, 1988.

[6] R. L. Steigerwald, "A comparison of half bridge resonant converter topology," IEEE Transaction, Power Electronics, Vol. 3, pp.174–182, April 1988.

[7] T. H. Solane, "Design of high-efficiency series resonant converter above resonance," IEEE Transactions, Aerospace Electronics System, Vol. 26, pp. 393–402, March 1990.

[8] V. Agarwal, V. Belaguli, and A. K. S. Bhat, "Large signal analysis using discrete time domain modeling for LCC-type parallel resonant converter operating in discontinuous current mode," in Canadian Conference Electrical

and Computer Engineering, pp. 83–88, 1993.

[9] K. S Bhat, “Analysis and design of a series parallel resonant converter,” IEEE Transactions on Power Electronics, Vol. 8, pp.1–11, 1993.

[10] V. Belaguli, “Series-parallel and parallel series resonant converters operating on the utility line-analysis, simulation and experimental results,” Ph.D. Dissertation, University Victoria, 1995.

[11] R. Severns, “Topologies for three element resonant converters,” in IEEE Applied Power Electronics, Conference Record, pp. 712–722, 1990.

[12] H. Neufeld, “Half-bridge resonant converter using the CS-360,” Cherry Semiconductor, Application Note, 1990.

[13] B. P. McGrath, “Design of a soft-switched 6-kw battery charger for traction applications,” IEEE Transactions on Power Electronics, Vol. 22, No. 4, pp.1136–1142, July 2007.

[14] H. Deng, “Analysis and design of iterative learning control strategies for UPS inverters,” IEEE Transactions on Industrial Electronics, Vol. 54, No. 3, pp. 1739–1751, June 2007.

[15] F. Z. Peng, “Z-Source inverter for motor drives,” IEEE Transactions on Power Electronics, Vol. 20, No. 4, pp.857–862, July 2005.

[16] V. Belaguli, “Series-parallel and resonant converter operating in DCM–Analysis, design, simulation and experimental results,” IEEE Transactions on Circuits and Systems, Vol. 47, pp. 433–441, 2000.

[17] Y. Jang, “Isolated boost converters,” IEEE Transactions on Power Electronics, Vol. 22, No. 4, pp. 1514–1521, July 2007.

Engineering, 2009, 1, 1-54
Published Online June 2009 in SciRes (http://www.SciRP.org/journal/eng/).

An Identified Study on the Active Network of a Thermoacoustic Regenerator

Guozhong Ding[1], Feng Wu[2], Gang Zhou[3], Xiaoqing Zhang[1], Jiuyang Yu[2]
[1]*School of Energy and Power Engineering, State key laboratory of coal combustion, Huazhong University of Science and Technology, Wuhan, Hubei, China*
[2]*School of Science, Wuhan Institute of Technology, Wuhan, China*
[3]*Technical Institute of Physics and Chemistry, Chinese Academy of Science, Beijing, China*
Email: *ding_guo_zhong@163.com*
Received March 27, 2009; *revised April* 30, 2009; *accepted May* 4, 2009

Abstract

An active thermo-acoustic network model of regenerator which is a key component to accomplish the conversion between thermal-and acoustic power in thermo-acoustic system has been established in this paper. The experiment was carried out to quantify the network. A method called least square is employed in order to identify the H matrix describing the system. The results obtained here show that the active thermo-acoustic network can reliably depict the characteristics of a thermo-acoustic system.

Keywords: Regenerator, Active Network, H Matrix, System Identification

1. Introduction

The regenerator, which produces thermo-acoustic effects, is a key component for thermo-acoustic engines (refrigerators), and its performance has a significant impact on engine system. In recent years research on regenerators has received significant attention due to the complexity of oscillating flow. Gary et al. developed a computational model for a regenerator based upon the bounded derivative method by Kreiss [1]. Y. Matsubara studied the effect of void volume in regenerator [2]. Kwanwoo et al. made use of a novel flow analysis method for regenerator under oscillating flow [3] and Chen et al. studied the heat transfer characteristics of oscillating flow regenerator [4]. While their method produces accurate results, the implementation is difficult. Swift [5] showed that regenerators can convert heat into acoustic work, and a regenerator with longitude temperature gradient is an active network. The regenerator network model [6], which is based on linear thermo-acoustic theory, was adopted for theoretical analysis and engineering calculation.

The system identification is a powerful tool for investigation of practical engineering devices. By means of fitting experimental data, model parameters can be found and applied to the model for use in engineering. The objective of this paper is to identify these parameters of the thermo-acoustic network describing the regenerator in a thermo-acoustic engine. An active network model of regenerator has been established by solving transport equations describing the regenerator used in this paper. By adopting capillary numbers as identification parameter, the transport matrix of the network is identified systematically, this includes effects of the resistance and compliance to avoid linear error of the model. The results obtained herein will be useful for quantifying the network describing the regenerators and for the optimal design of real regenerators, although the model relies on linearity of the phenomenon, and ignore some complexity.

2. The Acoustic Properties of a Regenerator

The gas flow in the regenerator is considered as periodic one-dimensional unsteady flow. The interaction between porous material and working medium leads to the following equations that describe the propagation of the

[1]Corresponding author, Fax:+86-027-87540724.

sound waves in a "porous medium":

$$\frac{\partial^2 P}{\partial z^2} + \left(\frac{\omega}{c_z}\right)^2 P = 0 \tag{1}$$

$$\frac{\partial v}{\partial z} = -j\frac{\omega}{\rho_z c_z^2} P \tag{2}$$

where P is sound pressure, $c_z = \dfrac{c_p}{\sqrt{1 - j\dfrac{s}{\rho_p \omega}}}$, $\rho_z = \dfrac{\rho_p c_p^2}{c_z^2}$, $\rho_p = \phi \rho_f$ it denotes the density of the medium inside the material; $s = \phi^2 R + j\omega\rho_p (K_s - 1)$, is air/porous material coupling factor. ω is angular frequency. While the porosity and the density of the porous material can be measured easily, the definition of sound velocity c_p needs a hypothesis about the thermodynamic process that the fluid undergoes inside the porous material.

Generally porous materials have a complex propagation constant γ_0 and acoustic impedance Z_0. The real part of the propagation constant is directly related to sound wave attenuation inside the porous material; the acoustic impedance is high at low frequency and asymptotically tends to that of the medium at higher frequencies.

A volumetric porosity ϕ is defined simply as the ratio of connected void volume V_{void} to the total volume of the sample regenerator V_{total}, and hydraulic diameter are defined as follows:

$$\phi = \frac{V_{void}}{V_{total}} \tag{3}$$

$$r_h = d\frac{\phi}{4(1-\phi)} \tag{4}$$

These quantities are easy to measure accurately for stacked screens. As the frequency increases, the viscous penetration depth decreases, so the mesh of stacked screens need be chosen with the resonance frequency of the thermo-acoustic engine. The loss of the regenerator is a very difficult term because the heat transfer process has some complexity such as the presence of heat exchangers, minor losses associated with an abrupt change in the cross section of the flow passage. Its viscous distribution function h_v and heat distribution function h_k, mainly dependent on the geometry of regenerator channels, their expression for cylinders only as follows:

$$h_v = \frac{J_0\left[(i-1)r/\delta_v\right]}{J_0\left[(i-1)r_h/\delta_v\right]},\quad f_v = \frac{2J_1\left[(i-1)r_h/\delta_v\right]}{(i-1)r_h/\delta_v J_0\left[(i-1)r_h/\delta_v\right]}$$
$$h_\kappa = \frac{J_0\left[(i-1)r/\delta_\kappa\right]}{J_0\left[(i-1)r_h/\delta_\kappa\right]},\quad f_\kappa = \frac{2J_1\left[(i-1)r_h/\delta_\kappa\right]}{(i-1)r_h/\delta_\kappa J_0\left[(i-1)r_h/\delta_\kappa\right]} \tag{5}$$

f_v and f_k denotes spatial-mean values of viscous distribution function and heat distribution function, where J is Bessel function. $\delta_k = \sqrt{2k/\omega}$ is the fluid's thermal penetration depth, and $k = \dfrac{K}{\rho_0 c_p}$ is its thermal diffusivity. $\delta_v = \sqrt{\dfrac{2\nu}{\omega}}$ is the viscous penetration depth.

3. Active Network for No Isothermal Regenerators

An actual regenerator possesses longitude temperature oscillation and longitude pressure oscillation, and there is transverse temperature oscillation in fluid about a thermal penetration depth near the surface of solid boundary. The major difference between regenerators and stacks is that regenerators tend to be more like a porous medium, consisting of extremely narrow, smaller than the viscous penetration depth, tortuous paths. The characteristics could not be described by passive network. According to linear thermo-acoustic theory [5], regenerators can convert energy between thermal and acoustic work by coupling longitude sound wave (pressure wave) and transverse thermal wave (temperature wave), and this can be described by two subsystems , in which subsystem 1 links with acoustic field in regenerator channels and subsystem 2 links with the thermal penetration depth. The performance of regenerator depends on the optimization of the coupling between the two subsystems.

For an actual regenerator with temperature gradient, a capillary model is adopted in regenerator channels. By solving basic control equations (mass conversation equation, momentum equation, energy equation and state

Nomenclature: P-sound pressure, ω-frequency, c-sound velocity, s-air/porous material coupling factor, γ_0-complex propagation constant, ϕ-volumetric porosity, r_h-hydraulic diameter, h_v-viscous distribution function, h_k-heat distribution function, f_v-viscous distribution function, f_k-heat distribution function, δ_k thermal penetration depth, δ_v-viscous penetration depth, J-volumetric flow rate, Z-impedance, Y-admittance, Pr-Prandtl number, ρ_0- mean density, *A*-channel area, γ-ratio of specific heats, T_m-average temperature, A'-transport matrix, Re-real of complex number, θ-phase shift, ΔT-temperature difference.

equation) under the condition of known boundary, the transport equations for no isoentropy oscillation can be obtained as follows [6−8]:

$$\begin{cases} \dfrac{\partial P}{\partial z} = -ZJ \\ \dfrac{\partial J}{\partial z} = -YP + \alpha J \end{cases} \tag{6}$$

where P is the ordinary pressure wave and J is volumetric flow rate, $Z = \dfrac{i\omega\rho_0}{A(1-f_v)}$, $Y = \dfrac{i\omega A}{\gamma p_0}[1+(\gamma-1)f_\kappa]$, $\alpha = \dfrac{f_k - f_v}{(1-P_r)(1-f_v)}\dfrac{1}{T_m}\dfrac{dT_m}{dz}$.

Z is the impedance and Y is admittance per unit length of channel , Pr , ρ_0, A, γ , ω, T_m are the fluid's Prandtl number, mean density, channel area of regenerator , ratio of specific heats, average temperature and angular frequency respectively.

The second term of Equation (6) in the right is a source, it denotes a flow source, where α is the thermo-acoustic source parameter of the regenerator. On one hand, it is confirmed by mathematically configuration of Equation (6). On the other hand, position oscillation of medium results in pressure oscillation of medium in control volume physically, temperature variation and density variation. The density oscillations in the thermal boundary layer act as a volume flow source and result in the change of velocity oscillation. The temperature variation produces a source in the flow field, and these characteristics can be called flow source [6,8]. The input power deposited in acoustic field prompts pressure oscillation interfering with impedance. So there are a flow source in no isothermal capillary network, this is αJ. The thermo-acoustic source parameter α is also called as flow amplification factor. The flow gain αJ produced by flow source will increase the acoustic field in regenerator medium (acoustic work $\propto \alpha J$), and in the end of the regenerator stable acoustic work output can be obtained.

According to network theory [5,8], flow process of no isothermal tubes of ideal small length in terms of Equation (6) can be expressed for an active network as Figure 1 shown.

The transport equations responding to Figure 1 are expressed as:

$$\begin{bmatrix} P(z) \\ J(z) \end{bmatrix} = \begin{bmatrix} 1+Z\delta z\dfrac{Y\delta z}{1+\alpha\delta z} & \dfrac{Z\delta z}{1+\alpha\delta z} \\ \dfrac{Y\delta z}{1+\alpha\delta z} & \dfrac{1}{1+\alpha\delta z} \end{bmatrix} \begin{bmatrix} P(z+\delta z) \\ J(z+\delta z) \end{bmatrix} = A' \begin{bmatrix} P(z+\delta z) \\ J(z+\delta z) \end{bmatrix} \tag{7}$$

where A' is a transport matrix. For the tube whose length is l, its network is made up of many such networks shown as Figure 1, so we can obtain:

$$\begin{bmatrix} P_i \\ J_i \end{bmatrix} = (\prod A'_k) \begin{bmatrix} P_o \\ J_o \end{bmatrix} = A \begin{bmatrix} P_o \\ J_o \end{bmatrix} = \begin{bmatrix} A_{11} & A_{12} \\ A_{21} & A_{22} \end{bmatrix} \begin{bmatrix} P_o \\ J_o \end{bmatrix} \tag{8}$$

where i and o denote input and output.

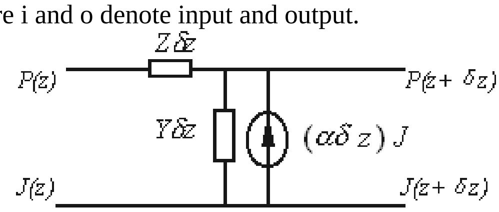

Figure 1. Schematic diagram of Γ type network model.

4. H Matrix Model and Identification

4.1. H Matrix Model

Obviously, it is not convenient to use Equation (8) to calculate the network. For quantifying the network, Equation (6) can be modified as:

$$\begin{cases} \dfrac{\partial^2 P}{\partial z^2} - \alpha\dfrac{\partial P}{\partial z} - YZP = 0 \\ \dfrac{\partial^2 J}{\partial z^2} - \alpha\dfrac{\partial J}{\partial z} - YZJ = 0 \end{cases} \tag{9}$$

where α, Y, Z are spacial mean value of responding parameter, approximately substitute for middle value in the regenerator. Solving Equation (9) with boundary P(0) and J0 and from Equation (6), we can obtain:

$$P(z) = H'_{11}P(0) + H'_{12}J(0) \tag{10}$$

$$J(z) = H'_{21}P(0) + H'_{22}J(0) \tag{11}$$

where $$H'_{11} = \frac{\gamma_1\exp(\gamma_2 z) - \gamma_2\exp(\gamma_1 z)}{\gamma_1 - \gamma_2} \tag{12}$$

$$H'_{12} = \frac{Z[\gamma_1\exp(\gamma_2 z) - \gamma_2\exp(\gamma_1 z)]}{\gamma_1 - \gamma_2} \tag{13}$$

$$H'_{21} = \frac{Y[\gamma_1\exp(\gamma_2 z) - \gamma_2\exp(\gamma_1 z)]}{\gamma_1 - \gamma_2} \tag{14}$$

$$H'_{22} = \frac{\gamma_1 \exp(\gamma_1 z) - \gamma_2 \exp(\gamma_2 z)}{\gamma_1 - \gamma_2} \quad \textbf{(15)}$$

$$\gamma_1 = \frac{1}{2}\alpha + \frac{1}{2}\sqrt{\alpha^2 + 4YZ}\ , \quad \gamma_2 = \frac{1}{2}\alpha - \frac{1}{2}\sqrt{\alpha^2 + 4YZ}$$

According to above equations, the output of acoustic work in the regenerators depends on flow source parameters α . As α =0, above equations are transport equations for isothermal regenerator, they are ideal transport equations; As $\alpha \neq 0$, the network is equivalent with self-actuated oscillation shown as Figure 2, where direct power supply corresponds to input heat, and sound oscillation induced by solid medium cooperating with gas micro mass in regenerator channels corresponds to self-actuated oscillation.

Suppose z=l in Equations (10) and (11), transport equations for channel length l are obtained:

$$\begin{bmatrix} P(l) \\ J(l) \end{bmatrix} = H \begin{bmatrix} P(0) \\ J(0) \end{bmatrix} \quad \textbf{(16)}$$

where $H = \begin{bmatrix} H'_{11} & H'_{12} \\ H'_{21} & H'_{22} \end{bmatrix}_{z=l} = \begin{bmatrix} H_{11} & H_{12} \\ H_{21} & H_{22} \end{bmatrix}$.

Regenerators can be regarded as capillary bundles made up of N capillary. According to network characteristics:

$$\begin{bmatrix} P(l) \\ J(l)/N \end{bmatrix} = H \begin{bmatrix} P(0) \\ J(0)/N \end{bmatrix} \quad \textbf{(17)}$$

Equation (17) becomes

$$\begin{bmatrix} P(l) \\ J(l) \end{bmatrix} = \begin{bmatrix} H_{11} & H_{12}/N \\ H_{21}N & H_{22} \end{bmatrix} \begin{bmatrix} P(0) \\ J(0) \end{bmatrix} \quad \textbf{(18)}$$

4.2. Identification of H Matrix

Capillary number N are regarded as identification parameter x, Equation (18) becomes

$$\begin{cases} P_l = H_{11}P_0 + \dfrac{H_{12}}{x} J_0 \\ J_l = H_{21}xP_0 + H_{22}J_0 \end{cases} \quad \textbf{(19)}$$

The acoustic work of regenerators can be obtained as:

$$\bar{\dot{W}}_i = \frac{1}{2}\mathrm{Re}(P_l J_l^* - P_0 J_0^*)_i = \frac{1}{2}(A_i x + \frac{B_i}{x} + C_i) \quad \textbf{(20)}$$

where $A_i = P_{0i}^2 \mathrm{Re}[H_{11}H_{21}^*]_i$, $B_i = J_{0i}^2 \mathrm{Re}[H_{12}H_{22}^*]_i$

$$C_i = \mathrm{Re}[(H_{11}H_{22}^* - 1)P_0 J_0^* + H_{12}H_{21}^* P_0^* J_0]_i$$

Re denotes the real of complex number. i stands for experiment number. System identification adopts extreme theory, by solving function $\bar{\dot{W}}(x)$, the minimum of target functional analysis can be obtained. When theoretical $\bar{\dot{W}}(x)$ shows an optimal agreement with measured $\bar{\dot{W}}_i'$, x is an optimal evaluation. Error law function can be expressed as [11]:

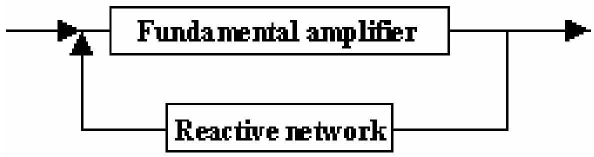

Figure 2. Self-actuated oscillation.

$$F(x) = \sum_i \left[\frac{1}{2}(A_i x + \frac{B_i}{x} + C_i) - \bar{\dot{W}}_i' \right]^2 \quad \textbf{(21)}$$

In order to get the minimum of error law function, let $\frac{\partial F}{\partial x} = 0$, we can obtain :

$$x^4 + bx^3 + dx + e = 0 \quad \textbf{(22)}$$

where $b = \dfrac{\sum_i A_i (C_i - 2\bar{\dot{W}}_i)}{\sum_i A_i^2}$, $d = -\dfrac{\sum_i B_i (C_i - 2\bar{\dot{W}}_i)}{\sum_i A_i^2}$,

$$e = -\frac{\sum_i B_i^2}{\sum_i A_i^2}$$

There should be 4 solutions. The right one can be chosen by mesh numbers and hydraulic diameter.

5. Experimental Identification

5.1. Experimental Apparatus

In order to identify the H matrix, a regenerator test apparatus with external actuator has been established, and its configuration is shown as Figure 3 and Figure 4. Input work is given by linear compressor, amplified output work is measured at the work receiver of an orifice valve and a buffer. In experiments, the helium gas as working medium is charged at 1.0MPa, while four kinds of dense meshes (#120, #150, #200, #250) were tested. Their geometric properties are shown as table 1. The pressures at two end of regenerator are measured by two piezo-electricity sensors of type CY-Yd-203, their signals are amplified by electric charge amplifier of type YE5853, and their phase shift is measured by SR830 DSP lock-in amplifier. The working frequency of linear compressor can be regulated by signal source. The hot heat exchanger consists of 15mm chinaware with an electrical heater. The length of regenerator is 50mm, the cold heat exchanger consists of 30mm copper shell tube exchanger. The corresponding working frequency is 282Hz.

In order to measure the output acoustic work, a small orifice valve and compliance are needed. Then

$$U_1 = -i\omega C p_{1,c} = \frac{i\omega V}{\gamma p_m} p_{1,c} \quad \textbf{(23)}$$

$$\dot{W}_2 = \frac{1}{2}\mathrm{Re}[p_{1,in}\tilde{U}_1] = \frac{\omega V}{2\gamma p_m}\mathrm{Im}[p_{1,in}\tilde{p}_{1,c}] = \frac{\omega V}{2\gamma p_m}\left|p_{1,in}\right|\left|p_{1,c}\right|\sin\theta \quad \textbf{(24)}$$

where $p_{1,in}$ is oscillating pressure behind the valve, $p_{1,c}$ is the entrance pressure in the network, and their phase shift is θ.

This is a lumped parameter RLC model for measurement of acoustic work, its calculation is independent of temperature of network components.

The pressure and volumetric flow rate measurement of regenerator inlet and outlet adopt two sensors method. The pressures between two ends of regenerator are measured by two pressure sensors. The acoustic power flow entering the regenerator is determined by reference [9] and [10].

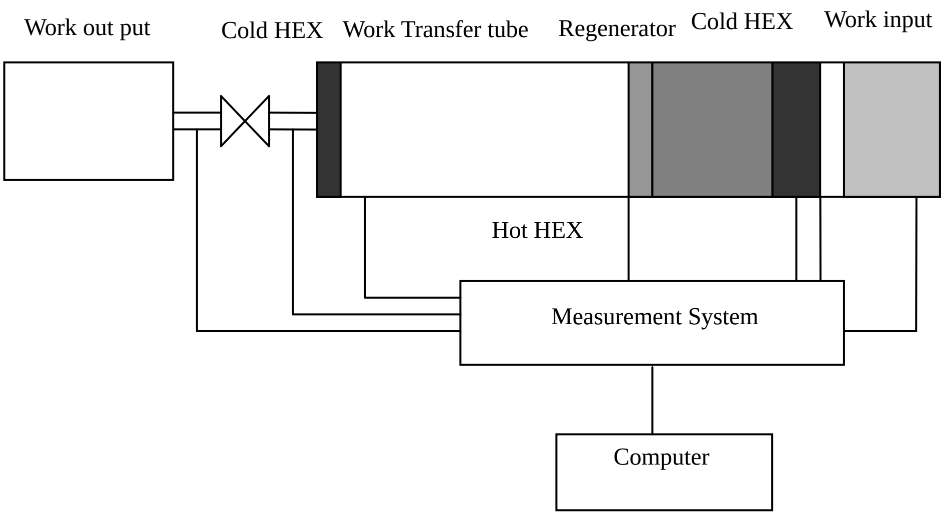

Figure 3. Schematic diagram of the experimental system.

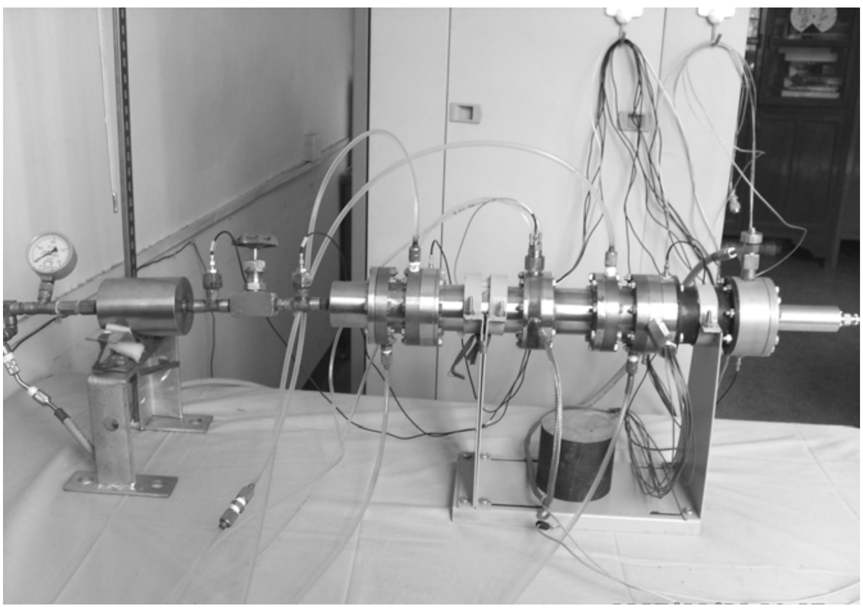

Figure 4. Experimental apparatus for system identification of regenerator.

Table 1. Geometric properties of regenerator Specimens (regenerator length=50mm,inner diameter=22mm).

Type of wire screen	Mesh number/cm	Hole diameter(mm)	Wire diameter(mm)	Porosity (%)	Hydraulic diameter(um)
80	31.5	0.198	0.12	70.3	71.1
120	47.2	0.132	0.08	70.3	47.4
150	59.1	0.104	0.065	69.8	37.7
200	78.7	0.074	0.053	67.2	27.2

The stacked screen is made up of #200 wire meshes (Table 1), its porosity is 0.672, and the temperature difference between the two ends of regenerator is 226K（the whole experimental range is 220K~400K）, and the oscillating frequency dependence can be found in Reference [9].

5.2. Experimental Results

Based on the experiment, the relation between the capillary number and wire meshes is shown as Figure 5 according to Equation (22). The calculated data and measured data of output acoustic work in regenerator after identification are shown as Figure 6 (for meshes #200). The error in the dimension measurements is less than 1.0%. The thermocouples with an accuracy of ±0.75% are utilized to measure both fluid and wall temperature. The error between measured and calculated acoustic work is less than 3% according to Figure 6.

The output acoustic work and COPR of regenerators for different wire meshes are shown as follows:

From Figure 7, the length of regenerators need be chosen accurately. The meshes of regenerators must match with the working frequency of thermo-acoustic engines.

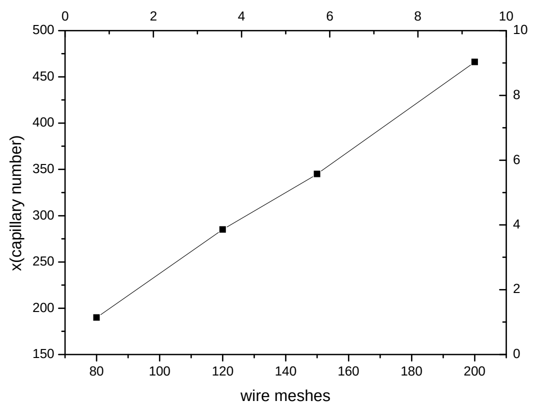

Figure 5. The relation of the identified capillary number and wire meshes.

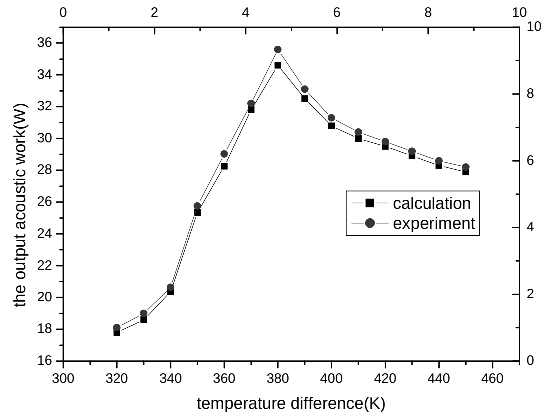

Figure 6. The relation of the output work and temperature difference of regenerator.

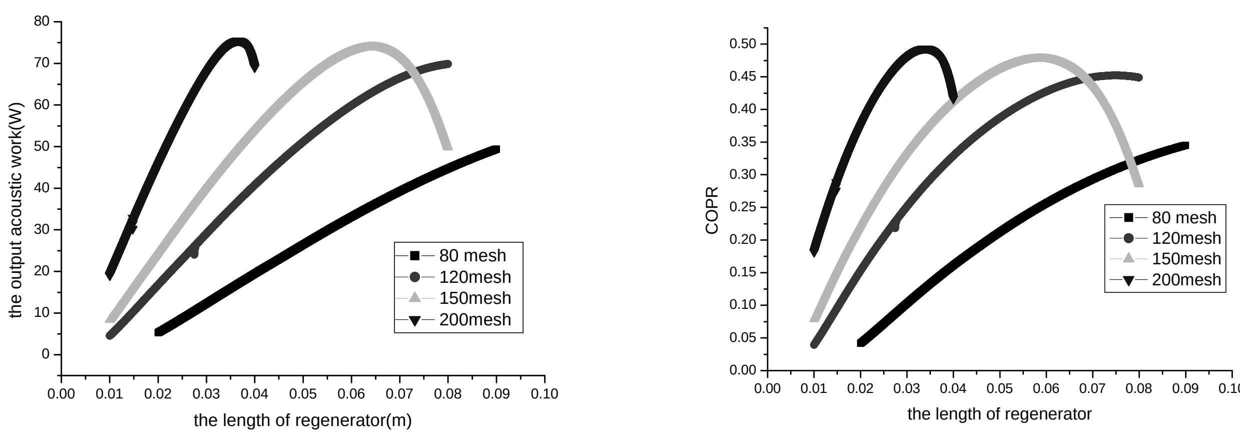

Figure 7. The output acoustic work and COPR of regenerators.

6. Conclusions

The lumped parameter H matrix of regenerator network is derived by establishing an active thermo-acoustic network model of regenerator, and identification parameters using capillary number N of system network are identified. The calculated results and measured data of output acoustic work in regenerators show a well agreement by identifying H matrix. The identified H matrix provides convenience for engineering calculation of regenerator, and provided a basis for whole network of thermo-acoustic engines.

7. Acknowledgements

The paper is supported by the Natural Science Fund of P. R. China (project No. 50676068).

8. References

[1] J. Gary, D. E. Pancy, and R. Radebaugh, "A computational model for a regenerator," in: Proceedings of Third Cryocooler Conference, NIST Special Publication, Vol. 698, pp.199–211, 1985.

[2] Y. Matsubara, "Effect of void volume in regenerator," in: Proceedings of The Sixth International Cryocooler Conference, 1990.

[3] K. Nam and S. Jeong, "Novel flow analysis of regenerator under oscillating flow with pulsating pressure," Cryogenics, Vol. 45, pp. 368–379, 2005.

[4] Y. Y. Chen, E. C. Luo, and W. Dai, "Heat transfer characteristics of oscillating flow regenerator filled with circular tubes or parallel plates," Cryogenics, Vol. 47, pp. 40–48, 2007.

[5] G. W. Swift, "Thermoacoustic engines," Journal of the Acoustical Society of America, Vol. 84, No. 4, pp. 1145–1179, 1988.

[6] X. H. Deng, "Thermoacoustic theory of regenerator and design theory for thermoacoustic engine [D]," Wuhan: Huazhong University of Science and Technology, 1994.

[7] F. Wu, et al., "Active network modeling for regenerator cryocooler [A]," Proceedings of Symposium on Energy Engineering in the 21st Century [C], Begell House New York, Wallingford, 2000.

[8] F. Z. Guo, "Dynamic heat transfer [M]," Wuhan: Huazhong University of Science and Technology Press, 1997.

[9] Q. Tu, Q. Li, F. Wu, and F. Z. Guo, "Network model approach for calculating oscillating frequency of thermoacoustic prime mover," Cryogenic, Vol. 43, pp. 351–357, 2003.

[10] Q. Tu, C. Wu, Q. Li, F. Wu, and F. Z. Guo, "Influence of temperature gradient on acoustic characteristic parameters of stack in TAE," International Journal of Engineering Science, Vol. 41, pp. 1337–1349, 2003.

Engineering, 2009, 1, 1-54
Published Online June 2009 in SciRes (http://www.SciRP.org/journal/eng/).

Skyhook Surface Sliding Mode Control on Semi-Active Vehicle Suspension System for Ride Comfort Enhancement

Yi Chen*
Department of Mechanical Engineering, University of Glasgow, Glasgow, United Kingdom
Email: *yichen@mech.gla.ac.uk*
Received March 25, 2009; *revised April* 11, 2009; *accepted April* 18, 2009

Abstract

A skyhook surface sliding mode control method was proposed and applied to the control on the semi-active vehicle suspension system for its ride comfort enhancement. A two degree of freedom dynamic model of a vehicle semi-active suspension system was given, which focused on the passenger's ride comfort performance. A simulation with the given initial conditions has been devised in MATLAB/SIMULINK. The simulation results were showing that there was an enhanced level of ride comfort for the vehicle semi-active suspension system with the skyhook surface sliding mode controller.

Keywords: Sliding Mode Control, Skyhook Damper, Fuzzy Logic Control, Semi-Active Suspension System

1. Introduction

The ride comfort is one of the most important characteristics for a vehicle suspension system. By reducing the vibration transmission and keeping proper tire contacts, the active and semi-active suspension system are designed and developed to achieve better ride comfort performance than the passive suspension system. The active suspension is designed to use separate actuators which can exert an independent force on the suspension, this action is to improve the suspension ride comfort performance. The active suspension system has been investigated since 1930s, but for the bottle neck of complex and high cost for its hardware, it has been hard for a wide practical usage and it is only available on premium luxury vehicle [1]. Semi-active (SA) suspension system was introduced in the early 1970s, it has been considered as good alternative between active and passive suspension system. The conceptual idea of SA suspension is to replace active force actuators with continually adjustable elements, which can vary or shift the rate of the energy dissipation in response to instantaneous condition of motion. SA suspension system can only change the viscous damping coefficient of the shock absorber, it will not add additional energy to the suspension system. The SA suspension system is also less expensive and energy cost than active suspension system in operation [2]. In recent years, research on SA suspension system has been continuing to advance with respect to their capabilities, narrowing the gap between SA and active suspension system. SA suspension system can achieve the majority of the performance characteristics of active suspension system, which cause a wide class of practical applications. Magnetorheological / Electrorheological (MR/ER) [3−5] dampers are both of the most widely studied and tested components of the SA suspension system. MR/ER fluids are materials that respond to an applied magnetic/electrical field with a change in rheological behaviour.

Variable structure control (VSC) with sliding mode control was introduced in the early 1950s by Emelyanov and was published in 1960s [6], further work was developed by several researchers [7−9]. Sliding mode control (SMC) has been recognized as a robust and efficient control method for complex high order nonlinear dynamical system. The major advantage of sliding mode control is the low sensitivity to a system's parameter changing under various uncertainty conditions, and it can decouple system motion into independent partial com-

*Yi Chen is with the Department of Mechanical Engineering, University of Glasgow, Glasgow, United Kingdom, G12 8QQ. Tel: 44(0)-141-330-2477, Fax: 44(0)-141-330-4343.

ponents of lower dimension, which reduces the complexity of the system control and feedback design. A major drawback of traditional SMC is chattering, which is generally disadvantageous within control system.

In recent years, a lot of literature has been generated in the area of SMC and has covered the improvement for traditional SMC, they harnessed to achieve better performance and reduce the chattering problem. A skyhook surface sliding mode control (SkyhookSMC) method will be developed and applied to the semi-active vehicle suspension system for the ride comfort enhancement in this paper.

It has been also well recognized, fuzzy logic control (FLC) is effective and robust control method for various applications, the FLC's rule-base comes from human's practical experience, however, the linguistic expression of the FLC rule-base makes it difficult to make guarantee the stability and robustness of the control system [10−11]. In order to compare and validate the control effects from the SkyhookSMC, a FLC controller is also designed in this paper.

2. Two Degree of Freedom Semi-Active Suspension System

The role of the vehicle suspension system is to support and isolate the vehicle body and payload from road disturbances, maintain the traction force between tires and road surface. The SA suspension system can offer both the reliability and versatility including passenger ride comfort with less power demand.

A two degree of freedom model which focused on the passenger ride comfort performance is proposed for SA suspension system in Figure 1. The SA suspension model can be defined by the Equation (1), where, m_1 and m_2 are the unsprung mass and the sprung mass respectively, k_1 is tire deflection stiffness, k_2 and c_2 are suspension stiffness and damping coefficients respectively, c_e is the semi-active damping coefficient which can generate damping force of f_d by MR/ER absorber in Equation (2). z_1, z_2 and q are the displacements for unsprung mass, sprung mass and road disturbance respectively, g is the acceleration of gravity. In order to observe the SA suspension status, the Equation (1) is re-written as a state-space in Equation (3).

$$\left\{\begin{array}{l} m_1\ddot{z}_1 + k_2(z_2 - z_1) + (c_2 + c_e)(\dot{z}_2 - \dot{z}_1) - k_1(z_1 - q) \\ +m_1 g = 0 \\ m_2\ddot{z}_2 - k_2(z_2 - z_1) - (c_2 + c_e)(\dot{z}_2 - \dot{z}_1) \\ +m_2 g = 0 \end{array}\right. \tag{1}$$

$$f_d = c_e(\dot{z}_2 - \dot{z}_1) \tag{2}$$

$$\left\{\begin{array}{l} \dot{X} = AX + BQ + EU \\ Y = CX + DQ + FU \end{array}\right. \tag{3}$$

In Equation (3), X is the state matrix for 2-DOF SA suspension system, which including tire deformation, suspension deformation, unsprung mass velocity and sprung mass velocity. Y is the output matrix, which including vehicle body acceleration, tire deformation, suspension deformation. U is the control force matrix. Q is the external disturbance matrix, which contains two disturbance signals: road profile of velocity and gravity acceleration for 2-DOF SA suspension system modelling. A, B, C, D, E, F are coefficient matrixes.

$$X = \left\{\begin{array}{c} z_1 - q \\ z_2 - z_1 \\ \dot{z}_1 \\ \dot{z}_2 \end{array}\right\} \quad Y = \left\{\begin{array}{c} \ddot{z}_2 \\ z_1 - q \\ z_2 - z_1 \end{array}\right\} \quad U = \{f_d\}$$

$$F = \left\{\begin{array}{c} \frac{1}{m_2} \\ 0 \\ 0 \end{array}\right\} \quad A = \begin{bmatrix} 0 & 0 & 1 & 0 \\ 0 & 0 & -1 & 1 \\ \frac{k_1}{m_1} & -\frac{k_2}{m_1} & \frac{c_2}{m_1} & -\frac{c_2}{m_1} \\ 0 & \frac{k_2}{m_2} & -\frac{c_2}{m_2} & \frac{c_2}{m_2} \end{bmatrix}$$

$$B = \begin{bmatrix} -1 & 0 & 0 \\ 0 & 0 & 0 \\ 0 & -1 & -\frac{1}{m_1} \\ 0 & -1 & \frac{1}{m_2} \end{bmatrix} \quad C = \begin{bmatrix} 0 & \frac{k_2}{m_2} & -\frac{c_0}{m_2} & \frac{c_0}{m_2} \\ 1 & 0 & 0 & 0 \\ 0 & 1 & 0 & 0 \end{bmatrix}$$

$$D = \begin{bmatrix} 0 & -1 & \frac{1}{m_2} \\ 0 & 0 & 0 \\ 0 & 0 & 0 \end{bmatrix} \quad E = \left\{\begin{array}{c} 0 \\ 0 \\ -\frac{1}{m_1} \\ \frac{1}{m_2} \end{array}\right\} \quad Q = \left\{\begin{array}{c} \dot{q} \\ g \\ 0 \end{array}\right\}$$

3. Sliding Mode Control with Skyhook Surface Design

In designing a SkyhookSMC, the objective is to consider

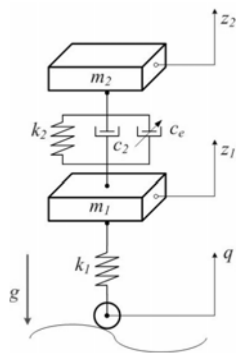

Figure 1. Two degree of freedom semi-active suspension system.

the non-linear tether system as the controlled plant, and therefore defined by the general state-space in Equation (4), where $x \in R^n$ is the state vector, n is the order of the non-linear system, and $u \in R^m$ is the input vector, m is the number of inputs.

$$\dot{x} = f(x, u, t) \quad \textbf{(4)}$$

$s(e,t)$ is the sliding surface of the hyper-plane, which is given in Equation (5) and shown in Figure 2, where λ is a positive constant that defines the slope of the sliding surface.

$$s(e,t) = \left(\frac{d}{dt} + \lambda\right)^{n-1} e \quad \textbf{(5)}$$

In the 2-DOF SA suspension system, we let n = 2, given that, as it is a second-order system in which s defines the position and velocity errors.

$$s = \dot{e} + \lambda e \quad \textbf{(6)}$$

From Equations (5) and (6), the second-order tracking problem is now being replaced by a first-order stabilization problem in which the scalar s is kept at zero by means of a governing condition [12]. This is obtained from use of the Lyapunov stability theorem, given in Equation (7), and it states that the origin is a globally asymptotically stable equilibrium point for the control system. Equation (7) is positive definite and its time derivative is given in inequality (8), to satisfy the negative definite condition, the system should satisfy the inequality in (8).

$$V(s) = \frac{1}{2}s^2 \quad \textbf{(7)}$$

$$\dot{V}(s) = s\dot{s} < 0 \quad \textbf{(8)}$$

The ideal Skyhook control strategy was introduced in 1974 by Karnopp et al. [13], which is known as one of the most effective in terms of the simplicity of the control algorithm. Figure 3 gives the ideal skyhook control scheme, the basic idea is to link the vehicle body sprung mass to the stationary sky by a controllable 'skyhook' damper, which could generate the controllable force of $f_{skyhook}$ and reduce the vertical vibrations by the road disturbance of all kinds [14−15]. Their original work uses only one inertia damper between the sprung mass and the inertia frame. The skyhook control is applicable for both a semi-active system as well as an active system. In practical, the skyhook control law was designed to modulate the damping force by a passive device to approximate the force that would be generated by a damper fixed to an inertial reference as the 'sky'.

The skyhook control can reduce the resonant peak of the sprung mass quite significantly and thus can achieve a good ride quality. By borrowing this idea to reduce the sliding chattering phenomenon, in Figure 4, a soft switching control law is introduced for the major sliding surface switching activity in Equation (9), which is to achieve good switch quality for the SkyhookSMC. The variable of s is defined in Equation (6), which contains the system information. It can be taken as a part of the SkyhookSMC control law in Equation (9), where c_0 is an

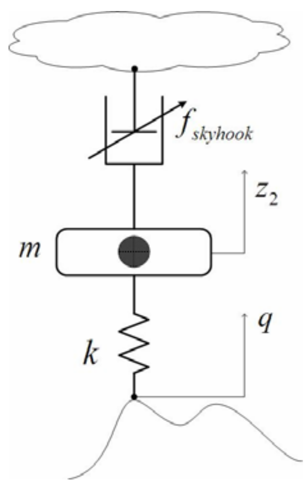

Figure 3. Ideal Skyhook control scheme.

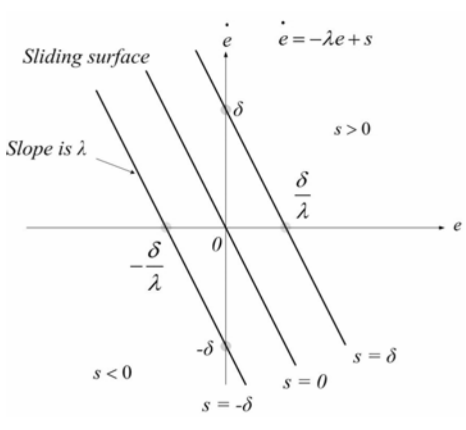

Figure 2. Sliding surface design.

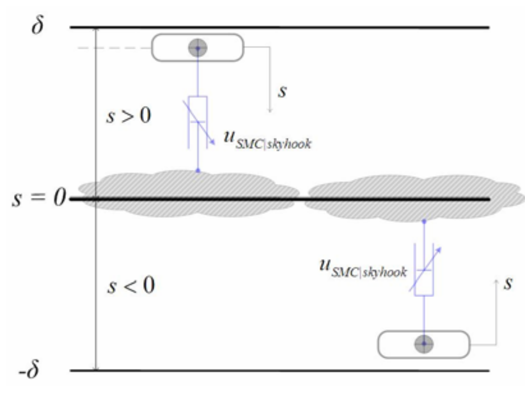

Figure 4. Sliding mode surface design with skyhook control law.

assumed positive damping ratio for the switching control law. The SkyhookSMC needs to be chosen in such a way that the existence and the reachability of the sliding-mode are both guaranteed. Noting that δ is an assumed positive constant which defines the thickness of the sliding mode boundary layer [16].

$$u_{SkyhookSMC} = \begin{cases} -c_0 \tanh\left(\frac{s}{\delta}\right) & s\dot{s} > 0 \\ 0 & s\dot{s} \leq 0 \end{cases} \quad \textbf{(9)}$$

4. Fuzzy Logic Controller Design

Fuzzy logic control is a practical alternative for a variety of challenging control applications, because it provides a convenient method for constructing nonlinear controllers via the use of heuristic information. The fuzzy logic control's rule-base comes from an operator's experience that has acted as a human-in-the-loop controller. It actually provides a human experience based representing and implementing the ideas that human has about how to achieve high-performance control.

The structure of the FLC for the 2-DOF SA suspension system is shown in Fig. 5, the 'If-Then' rule-base is then applied to describe the experts' knowledge. Fig. 6 is the 2-in-1-out FLC rule-base cloud which can drive the FLC inference mechanism. The FLC rule-base is characterized by a set of linguistic description rules based on conceptual expertise which arises from typical human situational experience. The 2-in-1-out FLC rule-base for the ride comfort of the 2-DOF SA suspension system is given in Table 1, which came from previous experience gained for the semi-active damping force control during body acceleration changes for ride comfort. Briefly, the main linguistic control rules are: 1) when the body acceleration increases, the SA damping force increases; 2) Conversely, when the body acceleration decreases, the SA damping force decreases.

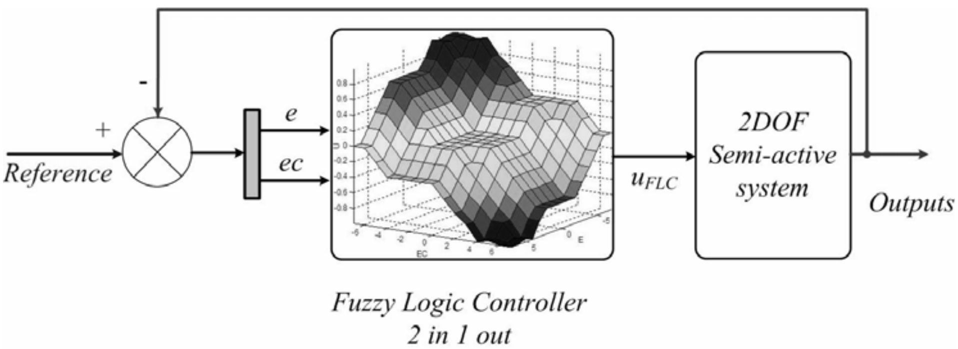

Figure 5. 2-in-1-out fuzzy logic control workflow diagram.

Figure 6 is the a rule-base 3D cloud map plot, which defines the relationship between 2 inputs of the error (E) and the change in error (EC) with 1 output of the semi-active control force (U). The full 2-in-1-out FLC rule-base is given in Table 1, which can map the FLC rule-base based on the inputs information of semi-active suspension body acceleration to the output control force.

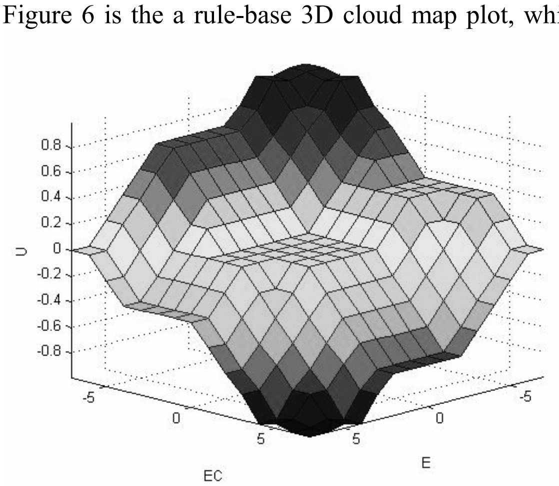

Figure 6. FLC rule-base 3D cloud map.

Fuzzification is the process of decomposing the system inputs into the fuzzy sets, that is, it is to map variables from practical space to fuzzy space. The process of fuzzification allows the system inputs and outputs to be expressed in linguistic terms so that rules can be applied

Table 1. 2-in-1-out FLC rule table for 2-DOF SA suspension system.

U		**EC**						
		NL	**NM**	**NS**	**ZE**	**PS**	**PM**	**PL**
	NL	PL	PL	PM	PS	PS	PS	ZE
	NM	PL	PM	PS	PS	PS	ZE	NS
E	**NS**	PM	PS	ZE	ZE	ZE	NS	NM
	ZE	PM	PS	ZE	ZE	ZE	NS	NM
	PS	PM	PS	ZE	ZE	ZE	NS	NM
	PM	PS	ZE	ZE	ZE	ZE	NM	NL
	PL	ZE	NS	NS	NS	NM	NL	NL

in a simple manner to express a complex system. In the FLC for 2-DOF SA suspension system, there are 7 elements in the fuzzy sets for 2 inputs of Error(E) and Error-in-Change(EC) and 1 output of FL are: < *NL, NM, NS, ZE, PS, PM, PL* >, the Fuzzy Inference System (FIS) of Mamdani-type inference for the FLC is shown in Figure 8. Defuzzification is the opposite process of fuzzification, it is to map variables from fuzzy space to practical space.

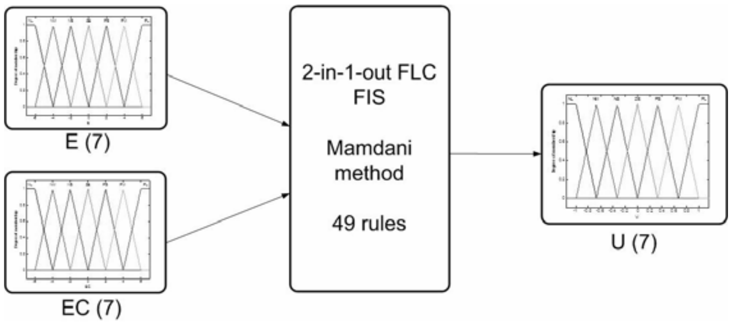

Figure 7. 2-in-1-out FLC inference system.

Basically, a membership function (MF) is a generalization of the indicator function in classical sets, which defines how each point in the input space is mapped to a membership value between 0 and 1. The MF for the 2-DOF SA suspension system is the triangular-shaped membership function, the MF for E is shown in Figure 8, the MF for EC and U are also triangular-shaped membership function with same elements range. The inputs of E and EC are interpreted from this fuzzy set, and the degree of membership is interpreted.

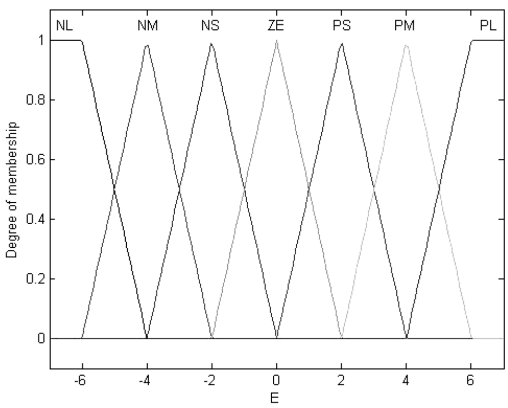

Figure 8. Triangular-shaped membership function for FLC controller.

5. Simulation and Conclusions

In the simulation for the control on 2-DOF SA suspension system, it is excited by a random road disturbance loading which is described by the road profile with the parameters of reference space frequency n_0 and road roughness coefficient $P(n_0)$ in Table 2. The numerical results are obtained using a MATLAB/SIMULINK. The velocity and acceleration of vehicle body are selected as error (e) and change in error (ec) feedback signals for the 2-DOF SA suspension system control. Unless stated otherwise all the results are generated using the following parameters for SA suspension system and controller in Table 2. Generally and partly, there are three performance indexes for vehicle suspension system, which include body acceleration, suspension deformation and tire load. In this context, the three indexes are good enough to evaluate the performance of the 2-DOF SA suspension system.

Table 2. 2-DOF SA suspension parameters.

m_1	Unsprung mass, kg	36
m_2	Sprung mass, kg	240
c_2	Suspension damping coefficient, Ns/m	1400
k_1	Tire stiffness coefficient, N/m	160000
k_2	Suspension stiffness coefficient, N/m	16000
g	Gravity acceleration, m/s^2	9.81
K_e	FLC scaling gains for e	−1
K_{ec}	FLC scaling gains for ec	−10
K_u	FLC scaling gains for u	21
C_0	SkyhookSMC damping coefficient	−5000
δ	Thickness of the sliding mode boundary layer	28.1569
λ	Slope of the sliding surface	10.6341
n_0	Reference space frequency, m^{-1}	0.1
P (n_0)	Road roughness coefficient, m^3/cycle	256×10^{-6}
v_0	Vehicle speed, km/h	72

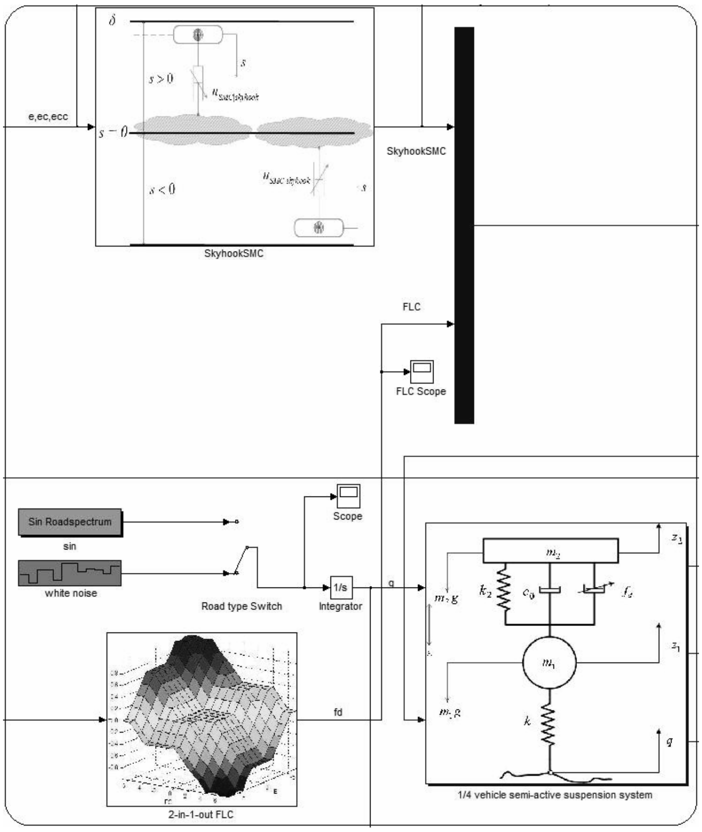

Figure 9. MATLAB/SIMULINK block for 2-DOF SA suspension system.

Figure 9 is the SkyhookSMC and FLC MATLAB/SIMULINK block for 2-DOF SA suspension system, which can compare the ride comfort performance with both SkyhookSMC and FLC control methods, all the post-simulation data analysis and plots are also generated by this SIMULINK block and its support MATLAB functions.

Mostly, a road profile is a series of random data in the actual surroundings. That is reason to describe the road profile by statistical techniques. One practical statistical way to generate road input is describing the road roughness in power spectral density (PSD). To generate the road profile of a random base excitation for the 2-DOF SA suspension simulation disturbance, a spectrum of the geometrical road profile with road class roughness-C is considered. The vehicle is travelling with a constant speed v_0, the time histories data of road irregularity are described by PSD method [17−19]. According to International Standard Organization (ISO)2631 [20], the ride comfort is specified in terms of root mean square (RMS) acceleration over a frequency range, in this simulation the RMS values for SkyhookSMC and FLC are {1.0530, 1.3134}, respectively, which confirms the validation of the SkyhookSMC on the ride comfort enhancement for 2-DOF SA suspension system.

The FLC parameters require a judicious choice of the scaling gains of $\{K_e, K_{ec}\}$ for fuzzification and the scaling gain of $\{K_u\}$ for defuzzification, in which, the $\{K_u\}$ is used to map the control force from the fuzzy space range to practical space range that actuators can work practically. Similarly, the SkyhookSMC damping coefficient c_0 is required to expand the normalised controller output force into a practical range. The thickness of the sliding mode boundary layer is given by $\delta = 28.1569$, and the slope of the sliding surface $\lambda = 10.6341$. Both of δ and λ value came from previous passive 2-DOF SA suspension system simulation results without control. With different simulation results of SkyhookSMC and FLC for the 2-DOF SA suspension system, all the control methods have an effect on the ride comfort enhancement for the 2-DOF suspension system in the given initial conditions.

Figure 10 gives the vertical behaviour of body acceleration - ride comfort performance. The upper subplot in Fig. 10 contains the body acceleration plots for SA suspension with FLC and passive suspension system, the FLC has body acceleration reducing effects on the passive suspension system to some extend, which depends on the human experience in FLC's rule-base. Meanwhile, the lower subplot in Figure 10 compares the control effects of SkyhookSMC and FLC control methods, it shows SkyhookSMC has better control effect than the FLC on body acceleration reducing.

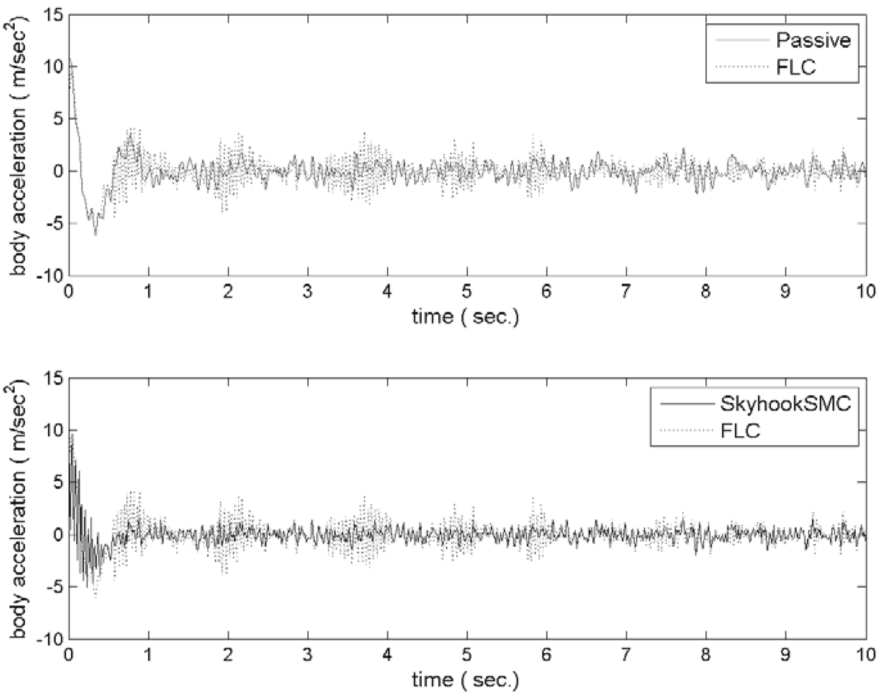

Figure 10. 2-DOF SA suspension system body acceleration response with SkyhookSMC vs. FLC control.

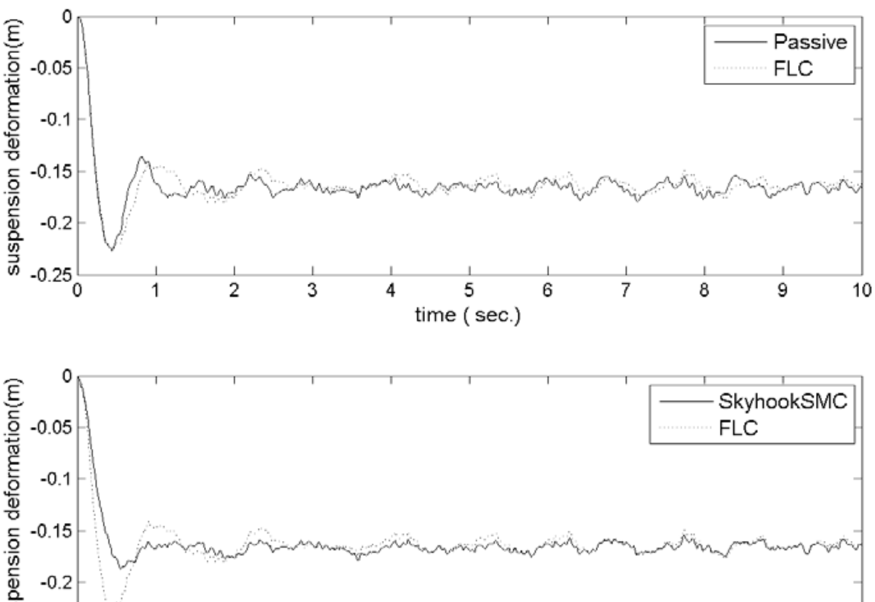

Figure 11. 2-DOF SA suspension deformation response with SkyhookSMC vs. FLC control methods.

Figure 11 shows the relative displacement between vehicle sprung mass and unsprung mass - suspension deformation, both of the plots in the simulation are showing the appearance of better and stable ride comfort. In Figure 11 the SkyhookSMC has also smaller suspension deformation than the FLC and passive suspension system, which also provides better ride comfort performance. According to Figure 10 and Figure 11, SkyhookSMC can provide better body acceleration and suspension deformation at the same time.

Figure 12 shows the tire load of the 2-DOF SA suspension system. In the upper subplot of Figure 12, when the FLC taking its effects on the SA system, the tire load staying in the same level as the passive suspension system. In the lower subplot of Figure 12, the tire load performs smaller and better when SkyhookSMC taking effects on the 2-DOF SA suspension system than FLC acting on the 2-DOF SA suspension system.

Figure 13 is the body acceleration amplitude in frequency domain, it shows that all the control methods of SkyhookSMC and FLC can reduce at two of the key resonance peak points (10 and 10^1 Hz). It also shows the SkyhookSMC has better control effects on 2-DOF SA suspension system ride comfort enhancement than traditional FLC and passive suspension system, but in higher frequency range, FLC has better performance than the SkyhookSMC to some extent in higher frequency range ($>10^1$Hz).

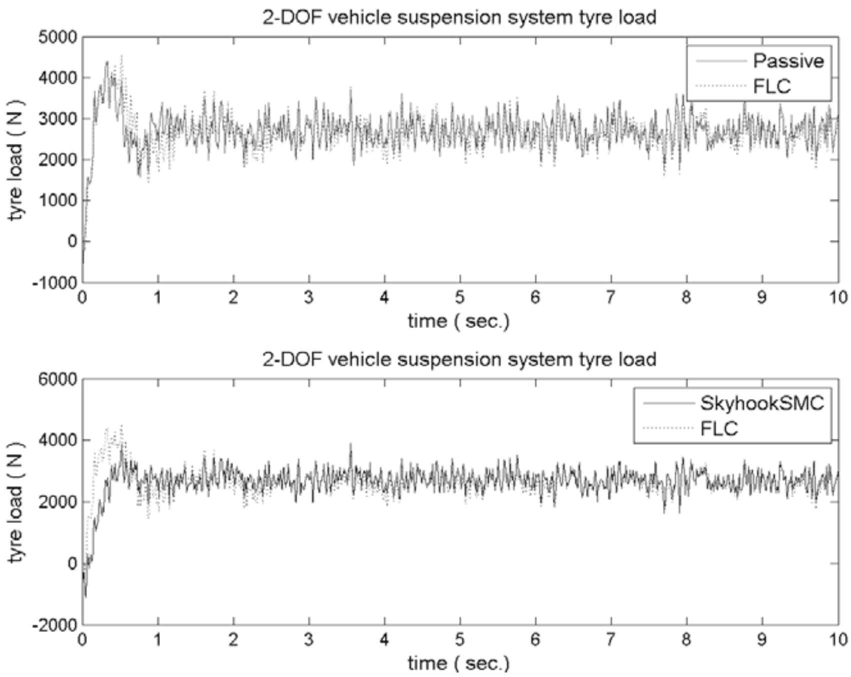

Figure 12. 2-DOF SA tire load response with SkyhookSMC vs. FLC control methods.

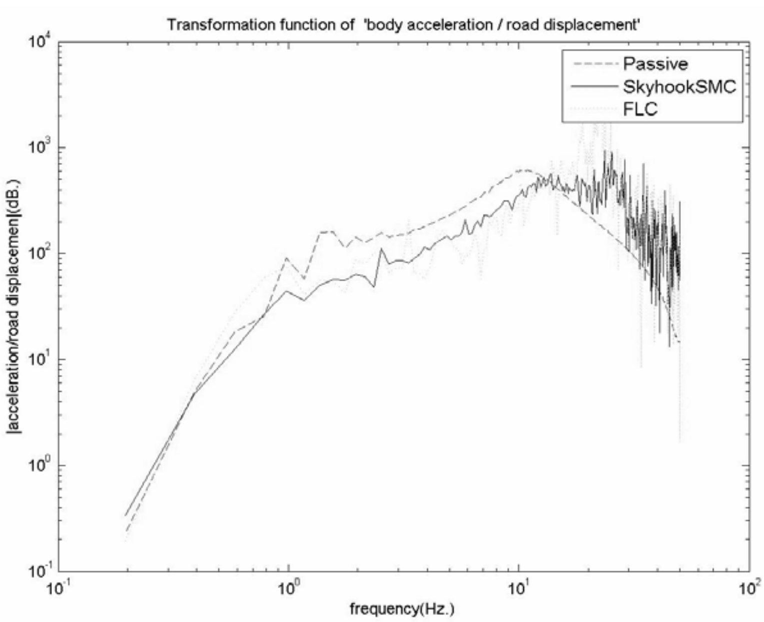

Figure 13. 2-DOF SA suspension system body acceleration response in frequency domain.

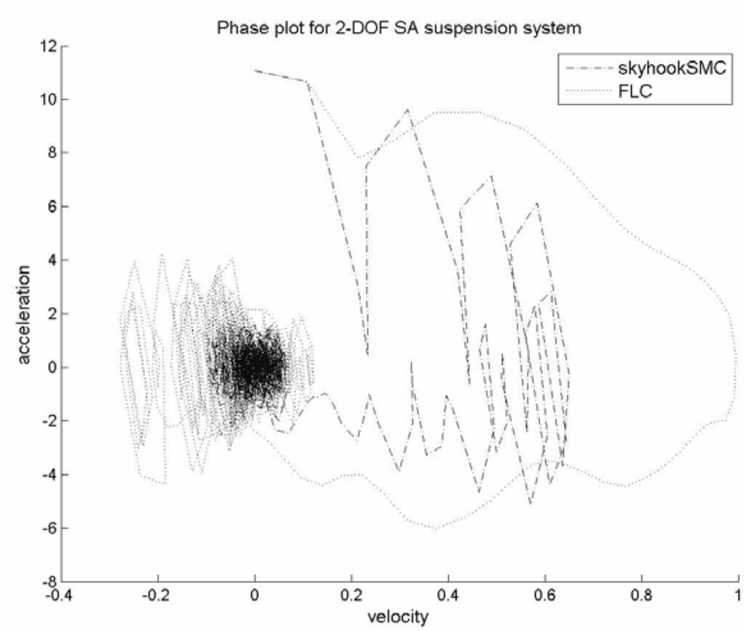

Figure 14. 2-DOF SA suspension system body response phase plot.

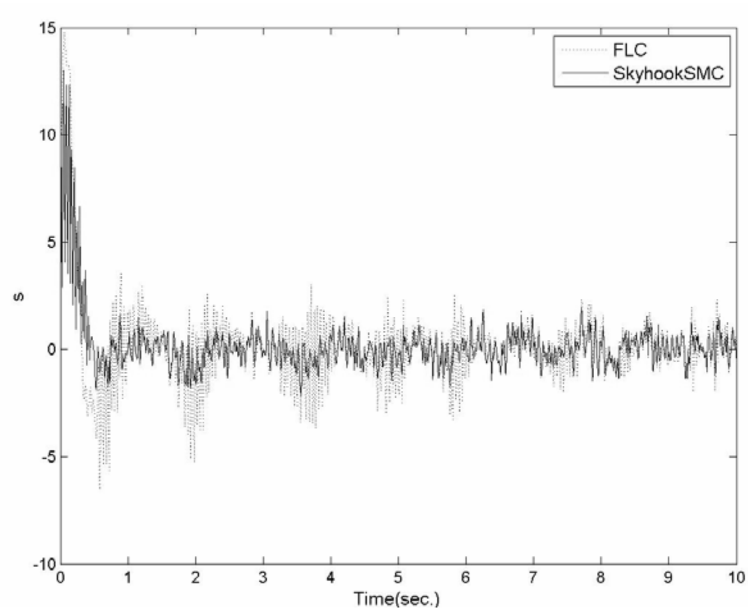

Figure 15. Sliding surface switching plot.

The phase plot (body velocity vs. body acceleration) is shown in Figure 14 as limit cycles with behaviour for 2-DOF SA suspension body vertical vibration, the curves started from the initial value point of (0,*g*), and gathered to the stable points area around (0,0) in close-wise direction, clearly, SkyhookSMC controller goes faster from the start point to steady status point, which corroborated the 2-DOF SA suspension system's SkyhookSMC controllable steady-state.

6. Future Work

The further study on the FLC and SkyhookSMC control methods by experimental system for the 2-DOF SA suspension system need to be designed. The further control methods will be studied to balance the control ability of FLC and SkyhookSMC to make obvious enhancement for the 2-DOF SA suspension system ride comfort in both time and frequency domain.

The parameter settings for the FLC and SkyhookSMC, including the SkyhookSMC damping coefficient c_0, thickness of the sliding mode boundary layer δ, slope of the sliding surface λ and FLC scaling gains of $\{K_e, K_{ec}, K_u\}$, need further consideration because the current simulation results come from manual parameter selection which based on passive suspension system simulation results. In order to enhance the parameter selection process and validation, some computational intelligence (CI) optimisation tools, such as Genetic Algorithms (GA) and Artificial Neural Networks (ANN), could be applied for parameter selection for the FLC and SkyhookSMC, this can hopefully give some reference sets for parameter selection. A GA has been used as an optimisation tool for parameter selection of the motorised momentum exchange tether system payload transfer from low Earth orbit to geostationary Earth orbit, and the GA's optimisation ability has therefore been reasonably demonstrated [21].

7. Acknowledgements

The author would like to acknowledge the support provided by the Overseas Research Students Awards Scheme and the Scholarship awarded by the University of Glasgow's Faculty of Engineering.

8. References

[1] K. Yi, M. Wargelin, and K. Hedrick, "Dynamic tire force control by semiactive suspensions," Journal of Dynamic Systems, Measurement, and Control, Vol. 115, No. 3, pp. 465−474, 1993.

[2] N. Jalili, "A comparative study and analysis of semi-active vibration-control systems," Journal of Vibration and Acoustics, Vol. 124, No. 4, pp. 593−605, 2002.

[3] R. Stanway, "The development of force actuators using ER and MR fluid technology," Actuator Technology: Current Practice and New Developments, IEE Colloquium on (Digest No: 1996/110), Vol. 6, pp. 1−5, 1996.

[4] L. Caracoglia and N. P. Jones, "Passive hybrid technique for the vibration mitigation of systems of interconnected stays," Journal of Sound and Vibration, Vol. 307, No. 3−5, pp. 849−864, 2007.

[5] Q. Zhou, S. R. K. Nielsen, and W. L. Qu, "Semi-active control of shallow cables with magnetorheological dampers under harmonic axial support motion," Journal of Sound and Vibration, Vol. 311, No. 3−5, pp. 683−706, 2008.

[6] S. V. Emelyanov, "Variable structure control systems (in Russian)," Moscow: Nauka, 1967.

[7] Y. Itkis, "Control systems of variable structure," New York: Wiley, 1976.

[8] V. A. Utkin, "Sliding modes and their application in variable structure systems," Moscow: Nauka (in Russian), 1978.

[9] J. Y. Hung, W. Gao, and J. C. Hung, "Variable structure control: A survey," IEEE Transactions on Industrial Electronics, pp. 2−22, 1993.

[10] L. A. Zadeh, "Fuzzy sets," Information and Control, Vol. 8, No. 3, pp. 338–353, 1965.

[11] K. M. Passino and S. Yurkovich, "Fuzzy control," Addison Wesley Longman, Menlo Park, CA, 1998.

[12] J. J. E. Slotine and W. P. Li, "Applied nonlinear control," Prentice-Hall International, 1991.

[13] D. C. Karnopp, M. J. Crosby, and R. A. Harwood, "Vibration control using semi-active force generators," Journals of Engineering for Industry, Transactions of the ASME, Vol. 94, pp. 619−626, 1974.

[14] H.-S. Kima and P. N. Roschke, "Design of fuzzy logic controller for smart base isolation system using genetic algorithm," Engineering Structures, Vol. 28, No. 1, pp. 84−96, 2006.

[15] S. M. Savaresi, E. Silani, and S. Bittanti, "Acceleration-Driven-Damper (ADD): An optimal control algorithm for comfort-oriented semiactive suspensions," ASME Transactions: Journal of Dynamic Systems, Measurement and Control, Vol. 127, No. 2, pp. 218−229, 2005.

[16] J. J. E. Slotine, "Tracking control of non-linear systems using sliding surfaces with application to robot manipulations," PhD Dissertation, Laboratory for Information and Decision Systems, Massachusetts Institute of Technology, 1982.

[17] E. M. Elbeheiry and D. C. Karnopp, "Optimal control of vehicle random vibration with constrained suspension deflection," Journal of Sound and Vibration, Vol. 189, No. 5, pp. 547−564, 1996.

[18] Y. Liu, H. Matsuhisaa, and H. Utsunoa, "Semi-active vibration isolation system with variable stiffness and damping control," Journal of Sound and Vibration, Vol. 313, No. 1−2, pp. 16−28, 2008.

[19] K. Ramji, A. Gupta, V. H. Saran, V. K. Goel, and V. Kumar, "Road roughness measurements using PSD approach," Journal of the Institution of Engineers, Vol. 85, pp. 193−201, 2004.

[20] International Organization for Standardization, "Mechanical vibration and shock – evaluation of human exposure to whole-body vibration – Part 1: General requirements," ISO 2631−1, 1997.

[21] Y. Chen and M. P. Cartmell, "Multi-objective optimisation on motorised momentum exchange tether for payload orbital transfer," IEEE Congress on Evolutionary Computation, pp. 987−993, September 25−28, 2007.

Engineering, 2009, 1, 1-54
Published Online June 2009 in SciRes (http://www.SciRP.org/journal/eng/).

The Effect of Price Discount on Time-Cost Trade-off Problem Using Genetic Algorithm

Hadi Mokhtari[1], Abdollah Aghaie[2]
Industrial Engineering Department, K. N. Toosi University of Technology, Tehran, Iran
Email: [1]*Mokhtari_IE@yahoo.com*, [2]*AAghaie@kntu.ac.ir*
Received April 21, 2009; *revised May* 13, 2009; *accepted May* 18, 2009

Abstract

Time-cost trade off problem (TCTP), known in the literature as project crashing problem (PCP) and project speeding up problem (PSP) is a part of project management in planning phase. In this problem, determining the optimal levels of activity durations and activity costs which satisfy the project goal(s), leads to a balance between the project completion time and the project total cost. A large amount of literature has studied this problem under various behavior of cost function. But, in all of them, influence of discount has not been investigated. Hence, in this paper, TCTP would be studied considering the influence of discount on the resource price, using genetic algorithm (GA). The performance of proposed idea has been tested on a medium scale test problem and several computational experiments have been conducted to investigate the appropriate levels of proposed GA considering accuracy and computational time.

Keywords: Project Management, PERT Networks, Time Cost Trade off, Genetic Algorithm, Discount

1. Introduction

Time-cost trade off problem (TCTP) is an important part of the project management in planning phase. It is a sub problem of project scheduling when finding the most cost effective way to finish a project within time limit is desirable. In the TCTP, the objective is to determine the duration of each activity in order to obtain the minimum costs of the project. All existing patterns of this problem satisfy the objective function through expediting the activity durations. In this problem, determining the optimal levels of activity durations and activity costs leads to a balance between the project completion time and the project total cost. There are some procedures in TCTP (e.g. extra resource allocation, improvement in technology level, increase in the quality of materials, hiring highly skillful human resources, etc.) used for expediting the activity durations, according to activity characteristics. These procedures can be summarized to a unique cost function corresponding to each activity.

Herroelen and Leus [1] evaluated some stochastic models of the TCTP under two main categories: “The stochastic discrete time/cost trade-off problem” and “Multi-mode trade-off problem in stochastic networks”. In the stochastic TCTP, when objective function of the model is related to the time, Bowman [2] presents a heuristic algorithm based on simulation technique and solves a general project compression problem using the derivative estimators. Besides, the application of mathematical programming for the stochastic project crashing problem was suggested by Abbasi and Mukattash [3], in which activities are assumed to have three time estimates. Unfortunately, it seems that the proposed approach has been developed for a network with a single path and is not applicable for the networks with slight differences in the path durations. Arisawa and Elmaghraby [4] suggested the use of fractional linear programming for the optimal allocation of resources to the activities in order to maximize the reduction in project mean duration per unit investment in GERT type networks. A novel resource-constrained project scheduling problem has been modeled by Golenko and Gonik [5] as a knapsack resource reallocation problem in which a heuristic algorithm has been to determine the optimal amount of resources allocated to the activities and their start times.

Some authors have investigated the stochastic TCTP to minimize the project total costs [6–8]. Gutjahr et al. [9] studied the discrete model of this problem by using the stochastic branch and bound method to improve the probability of meeting project deadline. In their work, they assumed that the crashing of activity durations (by using additional costs) leads to higher direct costs and lower penalty costs. In another research, Mitchell and Klastorin [10] have formulated the objective function with the direct, indirect, and penalty costs. This study presents a Stochastic Compression Project (SCOP) heuristic based on decomposition of PERT networks into the serial and parallel subnets. Recently, some researchers have considered the multi criteria/objective formulation for the stochastic TCTP [11–14].

In all of the presented papers, TCTP have investigated under various behaviors of the cost function such as discrete cost function [5,15–19], linear continuous cost function [20–22], nonlinear convex cost function [23,24], nonlinear concave cost function [25] and linear piecewise cost function [26,27]. But, in all of them, influence of discount has not been investigated. In this study, we develop a new TCTP based on discount in resource price to maximize the project completion probability in a predefined deadline using a limited available budget. In order to construct the model we assume that activity durations follow the normal distribution and the activity mean durations represent the decision variables. In order to solve this problem, we organize the genetic algorithm (GA) technique. Recently, some researchers use the GA in order to solve the project scheduling problems such as TCTP [11].

This paper is organized in the following way. The mathematical model is presented in Section 2. Section 3 describes the structure of the proposed approach, which is based on the GA algorithm. The characteristics of a large scale numerical example and results of applying the proposed approach to that example are presented in Section 4. The appropriate levels of GA parameters are investigated in this section. Finally Section 5 consists of concluding remarks.

2. Mathematical Model

Let $G=(N,A)$ be an acyclic Activity on Arrow (AOA) graph with arrow set A and node set N, where the source and sink node are denoted by s and t, respectively. $N=(n_1,n_2,...,n_m)$ represents the set of events, $A=(a_1,a_2,...,a_n)$ represents the set of activities in a project PERT network with m nodes and n activities.

Considered notations are presented as follows:

(i,j) Activity with i head node and j tail node

t_{ij} Random variable of activity (i, j) duration

μ_{ij} Mean duration of activity (i, j) (decisionvariable)

σ_{ij} Standard deviation of activity (i, j)

CS_{ij} Cost slope of activity (i, j)

R_{ij} Amount of allocated resource to activity (i, j)

T_d Project completion deadline

μ_{ij}^u Upper limit of mean of ith activity.

μ_{ij}^l Lower limit of mean of ith activity.

M Amount of available budget (i, j).

L Total number of paths.

n_r Number of activities which lie on path r.

T_r Random variable of path r duration.

μ_r The mean duration of path r.

σ_r The standard deviation of path r.

φ Cumulative distribution function (CDF) ofnormal standard distribution.

Generally, the TCTP is a nonlinear optimization problem. In order to investigate the effect of discount on this problem, we extract the objective function (project completion probability) and constraints, separately. The objective function (OF) is concerned with the maximization of project completion probability. To construct the OF, we can write a single path completion probability according to the central limit theorem (CLT), in the following way:

$$\Pr(T_r<T_d)=\Pr\left(Z<\frac{T_d-\mu_r}{\sigma_r}\right)=\Pr\left(Z<\frac{T_d-\sum_{ij\in r}\mu_{ij}}{\sum_{ij\in r}\sigma_{ij}}\right)=\phi\left(\frac{T_d-\sum_{ij\in r}\mu_{ij}}{\sum_{ij\in r}\sigma_{ij}}\right) \quad \textbf{(1)}$$

Equation (1) is related to a single path and can't improve the total project completion probability. Thus, considering all of the paths, the following objective function is suggested:

$$Max\ \{\ Min\ \ \phi\left(\frac{T_d-\sum_{ij\in r}\mu_{ij}}{\sum_{ij\in r}\sigma_{ij}}\right)\quad \forall\ r=1,2,....,L\ \ \} \quad \textbf{(2)}$$

Two type of restrictions should be modeled in a mathematical formulation to ensure the obtained solutions satisfy the budget limitation and real conditions. Each activity can be planned between two maximum and minimum limit of its mean duration. Following mathematical representation show this type of constraint:

$$\mu_{ij}{}^{l} \le \mu_{ij} \le \mu_{ij}{}^{u} \quad \textbf{(3)}$$

It is assumed that each activity needs a unique type of resource. Using this assumption, in order to model the budget limitation, we can define the effect of discount on resource price in a mathematical representation. For this purpose, cost slope (CS) due to various levels of μ_{ij} is presented below:

Using (4) we can formulate the cost function for activity (i, j) as a mathematical representation, in the following way:

$$CS_{ij} = \begin{cases} S_{ij}^{\circ} & R_{ij}^{\min} \le R_{ij} < R_{ij}^{1} \\ S_{ij}^{1} & R_{ij}^{1} \le R_{ij} < R_{ij}^{2} \\ S_{ij}^{2} & R_{ij}^{2} \le R_{ij} < R_{ij}^{3} \\ . & . \\ . & . \\ . & . \\ S_{ij}^{k-1} & R_{ij}^{k-1} \le R_{ij} < R_{ij}^{k} \\ S_{ij}^{k} & R_{ij}^{k} \le R_{ij} < R_{ij}^{\max} \end{cases} \quad \textbf{(4)}$$

$$C_{ij}(\mu_{ij}) = \begin{pmatrix} S_{ij}^{\circ}(\mu_{ij}^{\max} - \mu_{ij}) & \mu_{ij}^{\circ} \le \mu_{ij} < \mu_{ij}^{\max} \\ \vdots & \vdots \\ S_{ij}^{\circ}(\mu_{ij}^{\max} - \mu_{ij}^{\circ}) + \sum_{k=1}^{n-1} S_{ij}^{k}(\mu_{ij}^{k-1} - \mu_{ij}^{k}) + S_{ij}^{n}(\mu_{ij} - \mu_{ij}^{n-1}) & \mu_{ij}^{n-1} \le \mu_{ij} < \mu_{ij}^{n} \\ \vdots & \vdots \\ S_{ij}^{\circ}(\mu_{ij}^{\max} - \mu_{ij}^{\circ}) + \sum_{k=1}^{\min-1} S_{ij}^{k}(\mu_{ij}^{k-1} - \mu_{ij}^{k}) + S_{ij}^{\min}(\mu_{ij} - \mu_{ij}^{\min-1}) & \mu_{ij}^{\min} \le \mu_{ij} < \mu_{ij}^{(\min)-1} \end{pmatrix} \quad \textbf{(5)}$$

Using (4) and (5), we can formulate the second constraint that satisfies budget limitation, in the following way:

$$\sum C_{ij}(\mu_{ij}) \le M \quad \textbf{(6)}$$

So, the proposed TCTP can be summarized as a nonlinear optimization model, as follows:

$$Max\ \{\ Min\ \ \varphi \left(\frac{T_d - \sum_{ij \in r} \mu_{ij}}{\sum_{ij \in r} \sigma_{ij}} \right) \quad \forall\ r = 1, 2, \ldots, L\ \ \} \quad \textbf{(7)}$$

Subject to:

$$\sum C_{ij}(\mu_{ij}) \le M\ , \quad \textbf{(8)}$$

$$\mu_{ij}{}^{l} \le \mu_{ij} \le \mu_{ij}{}^{u} \qquad \forall\ Activitiy\ ij \in r \quad \textbf{(9)}$$

This is a new formulation of TCTP in PERT networks. In order to shorten each activity, some amount of extra resources is needed. This amount of resources may be provided by external suppliers, who may determine some incentive policy such as price discount. Our proposed TCTP, models this situation. Using this model, project manager can increase confidence level of on-time project completion and prevent project delay. Also, proposed model help us to use the available extra budget more efficiently, when we could find suppliers with discount policies.

3. Applying Genetic Algorithm

Genetic Algorithm (GA) is one of the popular metaheuristic algorithms, which can explore the feasible space using computational intelligence inspired from natural genetics and evolutionary concepts. It is a search method based on random selection policy can be used to solve the nonlinear mathematical programs. In this technique, an initial population containing several feasible solutions (chromosome) is generated randomly. Interesting fact is that GA does not need a good initial solution. In this procedure, algorithm starts from an initial solution and then it would be improved through an evolutionary process. After production of initial randomly generated population, parents are selected from this primary population and produce offspring. Second population is a combination of parent and offspring. The generation procedure has been done using two effective operators, cross over and mutation. The crossover is a genetic operator used to vary the programming of a chromosome or chromosomes from one generation to the next and the mutation operator can prevent the premature convergence of a new generation [28]. Desirability of obtained offspring is investigated using fitness function which is concerned with objective function and feasibility. The most common steps for GA follow:

- Generate the initial population
- Evaluate the fitness of all solutions in population
- Repeat:

Select parents

Apply the cross over and mutation operators to produce children

Evaluate the fitness of children

Establish new population using a combination of parents and children

- Until a satisfactory solution has been obtained

About the proposed GA for the discount based TCTP, we develop the chromosome structure as a simple string of decision variables. Indeed, each chromosome represents μ_{ij} for all of the activities. Proposed GA algorithm steps are presented in the following way:

- Initial random population is generated using uniform random number generator.
- Fitness of individuals is evaluated.
- Population is ranked in terms of computed fitness.
- Parents are selected randomly.
- Cross over and mutation are applied to produce children.
- Produced offspring are evaluated using fitness function.
- Form the new population using half of the fittest parent and half of the fittest children.

About the fitness function some points should be mentioned. In order to evaluate a solution (chromosome), two parameter should be investigated, goodness of solution and meaningfulness of solution. The goodness is concerned with objective function (project completion probability) and the meaningfulness indicates the feasibility. According to these parameters the fitness function can be represented as follows:

$$Fitness\ Function = \prod_{ij \in project} \gamma_{ij} \times \left[Min\ \varphi \left(\frac{T_d - \sum_{ij \in r} \mu_{ij}}{\sum_{ij \in r} \sigma_{ij}} \right) \forall r = 1, 2, \ldots, L \right] \tag{10}$$

In which, the first term represents feasibility and second one is concerned with project completion probability. γ_{ij} would be equal to one, if ${\mu_{ij}}^l \le \mu_{ij} \le {\mu_{ij}}^u$ & $\sum C_{ij}(\mu_{ij}) \le M$ and otherwise, indicates zero.

4. Numerical Example

In order to investigate the performance of the presented GA approach for the proposed discount based model of stochastic TCTP, a numerical example are described in this section. We conducted the proposed approach for the large scale example with 15 nodes, 20 independent activities and 44 interrelated paths to show that how the presented approach optimally improves the project completion probability. Characteristics of this network are presented in Table 2. The objective is to obtain optimal allocated budget to the activities in order to improve the all path completion probability from a risky value to a maximum confident one. It is assumed that the time unit is in weeks and the cost is in thousand dollars. According to the presented characteristics, initial probability of the project completion time at $T_d = 150$ which can be computed by using the Central Limit Theorem (CLT) is equal to 55%. This value is related to a situation that all activities are planned in their upper bound of μ_{ij}. The proposed approach attempts to improve this value to a maximum level using the limited available budget in order to decrease the risk of project tardiness. It is also assumed that the available amount of additional budget for this purpose is equal to 10,000 thousand dollars. We conducted our analysis of the presented example in two steps. In first step we run the developed procedure with the random initial values for parameters of the proposed GA. Then the obtained results are considered to determine the efficient values of the parameters in terms of the accuracy and computation time. For this purpose we developed a computer simulation program based on the proposed approach and randomly initial values of GA parameters have been considered in primary computational effort. The obtained simulation results for the considered example are organized in Table 1.

To investigate efficiency of the proposed GA approach, best obtained project completion probability and CPU time have been considered. In order to make trade off between the accuracy and computation time, we also solve the example with the different values of population size (k), mutation and cross over probabilities, then

Table 1. Characteristics of considered example.

Activity	μ_{ij}^{l}	μ_{ij}^{1}	μ_{ij}°	μ_{ij}^{u}	S_{ij}^{2}	S_{ij}^{1}	S_{ij}°	σ_{ij}
1	8.51	12.32	13.29	14.26	201.59	250.00	265.95	0.25
2	11.60	-	14.56	16.70	-	195.25	225.45	0.60
3	9.56	-	10.05	15.09	-	302.70	321.28	0.45
4	12.95	15.29	16.09	17.77	259.30	295.52	305.04	0.15
5	11.72	12.56	14.05	16.79	252.27	265.33	294.37	0.51
6	11.14	13.00	15.25	16.34	257.84	301.04	326.65	0.67
7	10.43	-	12.05	15.77	-	254.05	295.73	0.65
8	13.43	14.59	17.05	18.15	194.51	201.36	254.00	0.41
9	13.03	15.05	16.32	17.83	241.08	259.32	294.21	0.62
10	12.61	-	15.02	17.50	-	201.51	285.54	0.57
11	9.46	10.25	12.98	15.01	199.65	209.21	225.31	0.14
12	13.22	-	16.02	17.99	-	295.84	309.74	0.03
13	12.41	-	17.02	17.34	-	229.74	276.48	0.24
14	11.32	-	15.25	16.48	-	207.97	257.54	0.10
15	10.17	14.52	15.02	15.57	154.95	174.04	198.74	0.58
16	8.58	10.21	14.09	14.32	174.00	198.32	254.13	0.36
17	9.00	-	12.06	14.65	-	205.27	211.37	0.50
18	10.50	11.65	14.21	15.84	298.57	314.45	365.36	0.25
19	9.31	-	14.09	14.89	-	302.12	341.91	0.17
20	9.41	11.64	13.92	14.97	157.37	164.18	187.47	0.63

compute thecomputation time and efficiency measure. The appropriate levels of these parameters can conduct the GA toward optimal solution, directly and therefore, the analysis of these parameters is an important aspect of the proposed GA approach. Tables 2, 3 and 4 provide the behavior of the model results according to different levels of parameters, for presented example.

According to the simulation results provided by Tables 2, 3 and 4 the best probability of cross over and mutation rates are 0.8 and 0.2, respectively and best values of considered criteria (accuracy and CPU time) obtained by setting population size at 25-30. In this example the project completion probability has been improved from 55% to 0.79%.

5. Model Validation

The appropriate levels of the GA parameters have been investigated in section 4 to reach the accurate results with reasonable computation time. By using this procedure we reach the maximum capabilities of the proposed GA approach in terms of accuracy and computational time, but these maximum capabilities should be compared

Table 2. Model results (objective function) for different levels of P_c ($P_m = 0.2$, k = 25).

P_c	Run 1*	Run 2	Run 3	Run 4	Best Obj.
0.1	0.7390	0.7142	0.6952	0.7202	0.7390
0.2	0.6966	0.6414	0.7157	0.7377	0.7377
0.4	0.7222	0.6197	0.7585	0.6726	0.7585
0.6	0.7247	0.6253	0.7822	0.6792	0.7822
0.8	0.7009	0.6957	0.7951	0.7823	0.7951

* Each runs containing 200 iterations

Table 3. Model results (objective function) for different levels of P_m ($P_c = 0.7$, k = 25).

P_m	Run 1	Run 2	Run 3	Run 4	Best Obj.
0.1	0.7108	0.7561	0.6970	0.7896	0.7896
0.2	0.6876	0.7857	0.7952	0.7396	0.7952
0.4	0.7185	0.6969	0.7355	0.7291	0.7355
0.6	0.6827	0.6873	0.6269	0.7565	0.7565
0.8	0.7007	0.7067	0.7477	0.6900	0.7477

Table 4. Model results (computational time, objective function) for different levels of k ($P_c = 0.7$, $P_m = 0.2$).

k	Run 1		Run 2		Run 3		Run 4		CPU Time	Best Obj.
	CPU time	Obj. Func.	CPU Time	Obj. Func.	CPU Time	Obj. Func.	CPU Time	Obj. Func.		
5	10.40	0.692	11.24	0.642	9.80	0.716	15.59	0.701	10.40	0.716
10	16.10	0.722	15.92	0.707	25.21	0.757	20.65	0.740	15.92	0.757
12	17.41	0.710	16.10	0.735	29.51	0.740	23.62	0.727	16.10	0.740
18	30.60	0.731	29.25	0.765	39.74	0.788	45.41	0.751	29.25	0.788
25	40.25	0.758	45.62	0.761	54.30	0.780	42.20	0.796	40.25	0.796
30	51.50	0.793	47.26	0.757	59.20	0.798	65.20	0.795	47.26	0.798

with other standard solutions which are available in the literature to validate the solution. Since, this paper is the first combination of price discount with the TCTP, there isn't any standard test problem for the proposed model, in the published literature. We use the global optimum solution obtained by LINGO software to evaluate the performance of proposed approach. Indeed, LINGO can handle nonlinear programming problems involving both continuous and binary variables and solve such problem by generalized reduced gradient (GRG).

For this purpose a mathematical model based on a single path of PERT network has been considered. The results of comparing the proposed GA's best objective function (obtained by appropriate levels of GA parameters based on the procedure described in section 4) and LINGO's global optimum for a single path are presented in Table 5.

According to the Table 5, the proposed GA approach shows a difference with LINGO's global optimum with the average of 1.84%. Such a little difference can be reliable and shows the good performance of proposed approach.

6. Conclusions

In this paper, we proposed a new approach based on price discount for TCTP in PERT networks in which activity durations follow the normal distribution. The main objective of the developed model is to improve the

Table 5. Comparing the proposed GA best objective function and LINGO's global optimum.

Problem	Limited Budget (M)	Proposed GA	LINGO	Differences (LINGO-GA)	% Differences
1	10,000	0.7425	0.7489	0.0064	0.8620
2	15,000	0.7689	0.7909	0.0220	2.8612
3	20,000	0.7849	0.7981	0.0132	1.6817
4	25,000	0.8001	0.8214	0.0213	2.6622
5	30,000	0.8149	0.8236	0.0087	1.0676
6	35,000	0.8311	0.8544	0.0233	2.8035
7	40,000	0.864	0.8764	0.0124	1.4352
8	60,000	0.9049	0.9171	0.0122	1.3482
Average					1.8402 %

project completion probability from a risky amount to a maximum value using limited additional budget. To our knowledge, this is the first combination of price discount as a supplier's policy, with the TCTP, in the published literature. The presented model determines the optimal additional resources should be allocated to activities using the genetic algorithm. The GA algorithm has organized to allocate the available budget to activities. In order to illustrate the model efficiency, a computer program using MATLAB 7.6.0 was developed and the model was tested on a medium scale PERT network. Best amount of objective function and CPU time have been recorded and efficient levels of GA parameters have been investigated through the several computational experiments. In order to validate the GA approach, proposed model have been compared with the LINGO's global optimum solution and obtained results showed the good performance of the proposed solution approach.

7. References

[1] W. Herroelen and R. Leus, "Project scheduling under uncertainty: Survey and research potentials," European Journal of Operational Research, Vol. 165, pp. 289–306, 2005.

[2] R. A. Bowman, "Stochastic gradient-based time-cost tradeoffs in PERT networks using simulation," Annals of Operations Research, Vol. 53, pp. 533–551, 1994.

[3] G. Abbasi and A. M. Mukattash, "Crashing PERT networks using mathematical programming," International Journal of Project Management, Vol. 19, pp. 181–188, 2001.

[4] S. Arisawa and S. E. Elmaghraby, "Optimal time-cost trade-offs in GERT networks," Management Science, Vol. 18, pp. 589–599, 1972.

[5] L. V. Tavares, "A multi stage non-deterministic model for a project scheduling under resource consideration," European Journal of Operational Research, Vol. 49, pp. 92–101, 1990.

[6] R. L. Bergman, "A heuristic procedure for solving the dynamic probabilistic project expediting problem," European Journal of Operational Research, Vol. 192, pp. 125–137, 2009.

[7] S. Foldes and F. Soumis, "PERT and crashing revisited: Mathematical generalization," European Journal of Operational Research, Vol. 64, pp. 286–294, 1993.

[8] L. Sunde and S. Lichtenberg, "Net-present value cost/time trade off," International Journal of Project Management, Vol. 13, pp. 45–49, 1995.

[9] W. J. Gutjahr, C. Strauss and E. Wagner, "A stochastic branch-and-bound approach to activity crashing in project management," INFORMS Journal on Computing, Vol. 12, pp. 125–135, 2000.

[10] G. Mitchell and T. Klastorin, "An effective methodology for the stochastic project compression problem," IIE Transaction, Vol. 39, pp. 957–969, 2007.

[11] A. Azaron, C. Perkgoz, and M. Sakawa, "A genetic algorithm approach for the time-cost trade-off in PERT networks," Applied Mathematics and Computation, Vol. 168, pp. 1317–1339, 2005.

[12] A. Azaron and R. Tavakkoli-Moghaddam, "A multi objective resource allocation problem in dynamic PERT networks," Applied Mathematics and Computation, Vol. 18, pp. 163–174, 2006.

[13] A. Azaron, H. Katagiri, and M. Sakawa, "Time-cost trade-off via optimal control theory in Markov PERT networks," Annals of Operations Research, Vol. 150, pp. 47–64, 2007.

[14] P. C. Godinho and J. P. Costa, "A stochastic multimode model for time cost tradeoffs under management flexibility," OR Spectrum, Vol. 29, pp. 311–334, 2007.

[15] W. Crowston and G. L. Thompson, "Decision CPM: A method for simultaneous planning, scheduling, and control of projects," Operations Research, Vol. 15, pp. 407–426, 1967.

[16] E. Demeulemeester, S. E. Elmaghraby, and W. Herroelen, "Optimal procedures for the discrete time/cost trade-off problem in project networks," European Journal of Operational Research, Vol. 88, pp. 50–68, 1996.

[17] E. Demeulemeester, B. De Reyck, B. Foubert, W. Herroelen, and M. Vanhoucke, "New computational results on the discrete time/cost trade-off problem in project networks," Journal of the Operational Research Society, Vol. 49, pp. 1153–1163, 1998.

[18] D. R. Robinson, "A dynamic programming solution to cost-time tradeoff for CPM," Management Science, Vol. 22, pp. 158–166, 1975.

[19] M. Vanhoucke and D. Debels, "The discrete time/cost trade-off problem: Extensions and heuristic procedures," Journal of Scheduling, Vol. 10, pp. 311–326, 2007.

[20] I. Cohen, B. Golany, and A. Shtub, "The stochastic time–cost tradeoff problem: a robust optimization approach," Networks, Vol. 49, pp. 175–188, 2007.

[21] D. R. Fulkerson, "A network flow computation for project cost curves," Management Science, Vol. 7, pp. 167–178, 1961.

[22] P. S. Pulat and S. J. Horn, "Time-resource tradeoff problem," IEEE Transactions on Engineering Management,

Vol. 43, pp. 411–417, 1996.

[23] E. B. Berman, “Resource allocation in PERT network under activity continuous time-cost functions,” Management Science, Vol. 10, pp. 734–745, 1964.

[24] R. Lamberson and R. R. Hocking, “Optimum time compression in project scheduling,” Management Science, Vol. 16, pp. B597–B606, 1970.

[25] J. Falk and J. Horowitz, “Critical path problems with concave cost-time curves,” Management Science, Vol. 19, pp. 446–455, 1972.

[26] R. Kelley, “Critical-pathplanning and scheduling: Mathematical basis,” Operations Research, Vol. 9, pp. 296–320, 1961.

[27] P. Vrat and C. Kriengkrairut, “A goal programming model for project crashing with piecewise linear time-cost tradeoff,” Engineering Costs and Production Economics, Vol. 10, pp. 161–172, 1986.

[28] I. Kaya, “A genetic algorithm approach to determine the sample size for control charts with variables and attributes,” Expert Systems with Applications, Vol. 36, pp. 8719–8734, 2009.

Engineering, 2009, 1, 1-54
Published Online June 2009 in SciRes (http://www.SciRP.org/journal/eng/).

Microstrip Antennas Loaded with Shorting Post

Pradeep Kumar, G. Singh
Department of Electronics and Communication Engineering,
Jaypee University of Information Technology, Solan, India
Email: *erpradeep_tiet@yahoo.co.in*
Received April 28, 2009; *revised May* 7, 2009; *accepted May* 14, 2009

Abstract

In this paper, a technical review with recent advances of the microstrip antennas loaded with shorting posts is presented. The overall size of the antenna is significantly reduced by a single shorting posts and the effect of the various parameters of shorting posts on short-circuit microstrip antenna is also discussed.

Keywords: Microstrip Antennas, Loading, Shorting Post, Efficiency, Gain, Bandwidth

1. Introduction

An explosive growth of the wireless radio communication systems is currently observed in the microwave band. In the short range communications or contactless identification systems, antennas are key components, which must be small, low profile, and with minimal processing costs [1−4]. The microstrip patch antennas are of great interest for aforementioned mentioned applications due to their compact structure. The flexibility afforded by microstrip antenna technology has led to a wide variety of design and techniques. The main limitations of the microstrip antennas are low efficiency and narrow impedance bandwidth. The bandwidth of the microstrip antenna can be increased using various techniques such as by loading a patch, by using a thicker substrate, by reducing the dielectric constant, by using gap-coupled multi-resonator etc [3−5]. However, using a thicker substrate causes generation of spurious radiation and there are some practical problems in decreasing the dielectric constant. The spurious radiation degrades the antenna parameters. Among various antenna bandwidth enhancement configurations, the two gap-coupled circular microstrip patch antenna is most elegant one. So, gap-coupling is the suitable method for enhancing the impedance bandwidth of the antennas [6,7]. In the configuration of gap-coupled microstrip antennas method, two patches are placed close to each other. The gap-coupled microstrip antennas generate two resonant frequencies and the bandwidth of the microstrip antennas can be increased [6].

There exist a wide range of basic microstrip antenna shapes such as rectangular, circular and triangular patch shapes which are commonly used patches. For these patches, operating at their fundamental mode resonant frequency, are of the dimension of the patch is about half wavelength in dielectric. At lower frequencies the size of the microstrip antennas becomes large. In modern communication systems the compact microstrip patch antennas are desirable. There are various techniques to reduce the size of the microstrip antennas. A common technique to reduce the overall size of a microstrip patch antenna is to terminate one of the radiating edges with a short circuit. The short circuit can be in the form of a metal clamp or a series of shorting posts [1]. It was shown that by changing the number of shorting posts and the relative position of these posts, the resonance frequency of the short-circuited microstrip patch can be adjusted [2]. In fact, by reducing the number of shorting posts the resonance frequency of the modified patch can be reduced. Thus for a set resonance frequencies, a significantly smaller element can be achieved using this technique compared to conventional microstrip patches. Further decrease in size can be obtained by loading the basic shapes by shorting post or slots [1,8,9].

In [10,11], circular microstrip patch antenna with dual frequency operation is designed by shorting the patch and the results are compared with the conventional circular microstrip antenna (without a shorting post) which shows that the size of the circular microstrip antenna can be reduced for the same frequency application. It is also observed that the resonant frequency of the circular microstrip antenna with shorting post can be varied by varying its location. In [12,13], the technique of shorting post is used for dual frequency operation.

2. Need of Loading with Shorting Post

The trend for technology in recent times is towards miniaturization and the demand for more compact and robust designs has been growing. The revolution in semiconductor manufacturing and device design methodologies has helped to achieve very high data rates transmission and compact size. In wireless devices, the antenna still remains a matter of concern as regards to its size. In some applications, operation at two or more discrete bands and an arbitrary separation of bands is desired. Further, all bands may be required to have the same polarization, radiation pattern and input impedance characteristics. Therefore, short circuit microstrip antennas are widely used because the short circuit antenna can realize the same resonant frequency, at about half the size of the standard microstrip antenna [2]. The shorted microstrip antenna is constructed by short-circuiting the zero-potential plane of an ordinary microstrip antenna excited with a dominant mode. Physically, this short circuit may be complete, by wrapping a copper strip around the edge of the antenna, or it may be simulated by shorting posts. From manufacturing point of view, construction of shorting posts is much easier than wrapping a copper strip around the edge of the antenna.

By loading of the microstrip antenna with shorting post, the size of the microstrip antennas can be reduced as well as multi-frequency operation, change of polarization etc can be achieved [11,14]. Depending on the application, the shorting pin may be located at the edge or at the center of the patch. However, the effect of the shorting posts depends on different parameters like the number of the posts, the radius of each post and the thickness of the microstrip antenna which determines the length of the posts.

Basically, the shorting post is modeled as an inductance parallel to the resonant LC circuit describing a reference resonant mode of the unloaded (without shorting post) patch. In an equivalent circuit, new resonance mode (with shorting post) can be viewed as resulting from the inductance (due to shorting post) in series with static capacitance of the patch configuration. Larger the inductive part smaller will be the resulting resonance frequency, that is, the larger will be the degree of miniaturization achieved for a fixed operating frequency [1]. This technique is used to reduce the resonance frequency has been proposed first time by Waterhouse [15] and has been demonstrated on a variety of different patch shapes [16]. Microstrip antennas were miniaturized by using shorting post in [1,17]. As shown in [15], the maximum reduction in physical size can be achieved if a single shorting post is used. Here the radius of circular patch was reduced by a factor of three, making the antenna size suited for compact communication systems. In [10], circular microstrip antenna with dual frequency operation is designed by shorting the patch. The results are compared with the conventional circular microstrip antenna (without a shorting pin). In [11], a rectangular microstrip antenna with dual frequency operation is designed by shorting the patch. It is observed that the size of the antenna can be reduced by shorting the patch at its edge.

3. Shorting Post Loaded Microstrip Patch Antennas for Various Applications

For lower frequencies, the size of the microstrip antenna is large. So, reduction in the size of the antenna is desired. The size of the antenna can be reduced by using microstrip antennas the size of the antenna can be reduced. The microstrip antennas loaded with shorting post for various applications are discussed as follows:

3.1. Circular Microstrip Antennas Loaded with Shorting Post

In [8], the rectangular and the circular microstrip antennas are loaded with shorting pin/post. The rectangular and circular microstrip antennas loaded with shorting post are shown in Figure 1(a) and Figure 1(b) respectively. The antennas are fed by probe feeding. The sizes of the antennas are reduced and the antennas are designed for mobile communication handsets.

In [1], an analytical theory for the eigenfrequencies and eigenmodes of shorting post loaded microstrip antennas is presented. It is shown that the zero mode of the unloaded MSA plays a central role for reducing the lowest operating frequency of the loaded microstrip antenna. For a circular patch loaded with single post, it was shown that a larger shorting post radii lead to stronger suppression of the inductive part of the shorting-post impedance and, therefore, resonates at higher resonant frequencies. The lowest values for the resonant frequency are obtained when positioning the shorting post at the edge of the patch. In general, the resonant frequencies obtainable from a loaded circular patch are larger than those of a rectangular patch of equal cross section. It is also seen that the sensitivity of the resonance frequency against variations of the shorting-post position of the circular patch is stronger than in the rectangular patch.

3.2. Rectangular Microstrip Antennas Loaded with Shorting Post

In [11], the rectangular microstrip antenna is loaded with shorting post at the center line of the patch as shown in Figure 2. This type of loading produces two lowest resonant frequencies with the same polarization. The size reduction of the antenna at the lowest frequency is roughly 2.6.

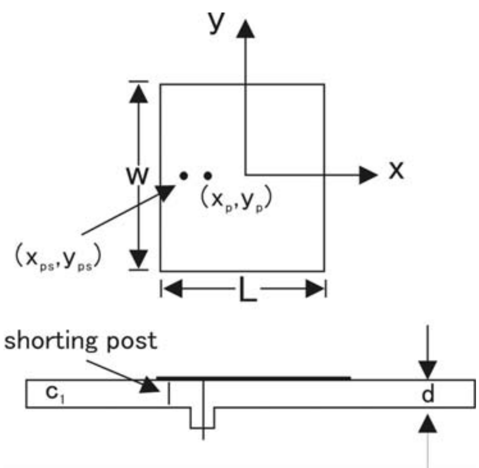

(a)

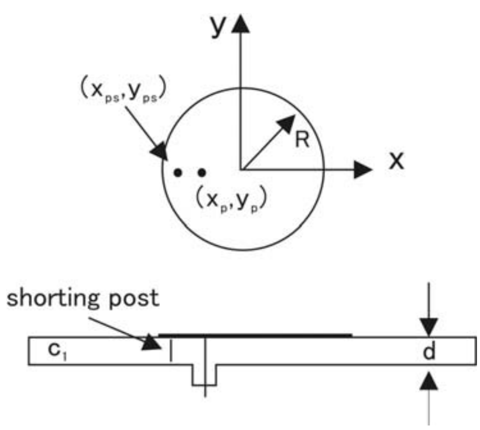

(b)

Figure 1. (a) Rectangular microstrip antennas loaded with shorting post, (b) circular microstrip antennas loaded with shorting post.

A dual frequency compact antenna capable of receiving both linearly and circularly polarized radiation has been reported in [18]. It generates linear polarization at the lower frequency and circular polarization at the upper frequency. It consists of a square patch with two symmetrical shorting pins. A reduction factor of 5 in area has been achieved at the lower frequency end.

3.3. Triangular Microstrip Antennas Loaded with Shorting Post

In [19] equilateral and 30o-60o-90o triangular microstrip antennas are shorted along the zero field to reduce the size of the antennas. The equilateral and 30o-60o-90o triangular microstrip antennas loaded with shorting post is shown in Figure3. These equilateral and 30o-60o-90o triangular microstrip antennas yield shorted 60 and 30o sectoral microstrip antennas, respectively and result in area reduction by factors of 2.5 and 5 respectively.

3.4. Pin Shorted Microstrip Antenna for Mobile Communication

In [20], pin shorted rectangular antenna is designed for mobile communication applications as shown in Figure4. The desired resonant frequency is obtained by shorting the patch. The designing is performed by simulation using Method-of-moments based software (IE3D). The shorting pin diameter as well as location of pin is varied and the antenna is made for mobile communication.

In [21], the size of the gap-coupled microstrip antennas is miniaturized using shorting post. The fed patch is loaded and the gap-coupled microstrip antennas produce triple frequency operation. The mutual coupling and input impedance of the gap-coupled circular microstrip antennas loaded with shorting post can be controlled by changing the diameter of shorting post [22–24]. In [25],

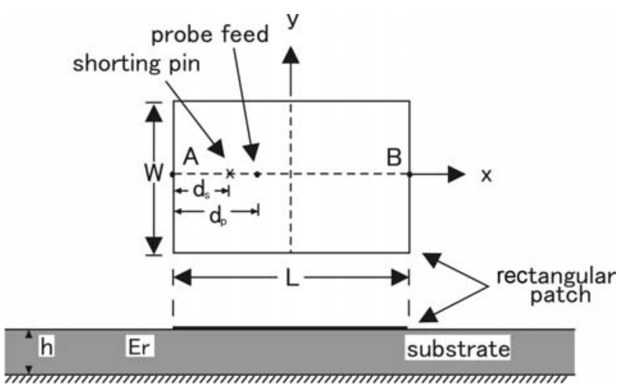

Figure 2. Rectangular microstrip antenna loaded with shorting post at the center line.

using shorting pin and multi-layer dielectric concept, a broadband and small antenna is designed. The designed antenna can be used in communication systems. In [12,13], the microstrip antennas are loaded with shorting post and the antennas are designed for dual frequency operation.

4. Conclusions

The size of the microstrip antennas can be reduced by using the concept of loading a microstrip antenna with shorting posts. For multi-frequency applications shorting posts loaded microstrip antenna can be used. A review of shorting post loaded microstrip antenna as well as need of the shorting post loaded microstrip antenna is presented. The different types of shorting post loaded microstrip antennas can be used for different applications.

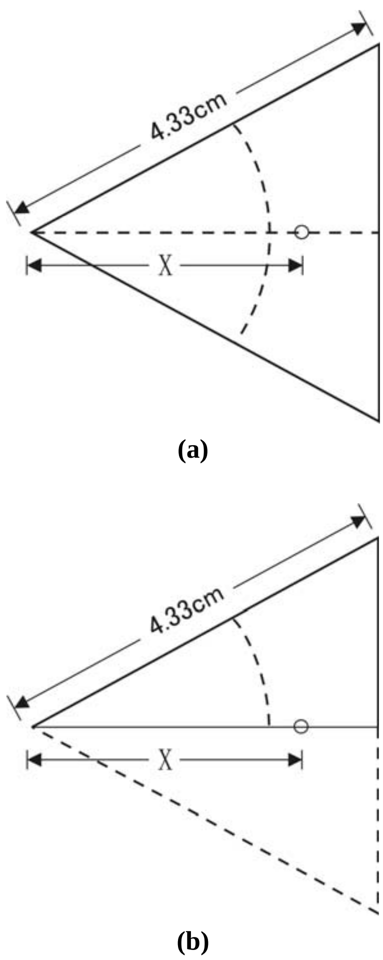

Figure 3. Triangular microstrip antennas loaded with shorting post, (a) Equilateral, (b) 30°-60°-90°.

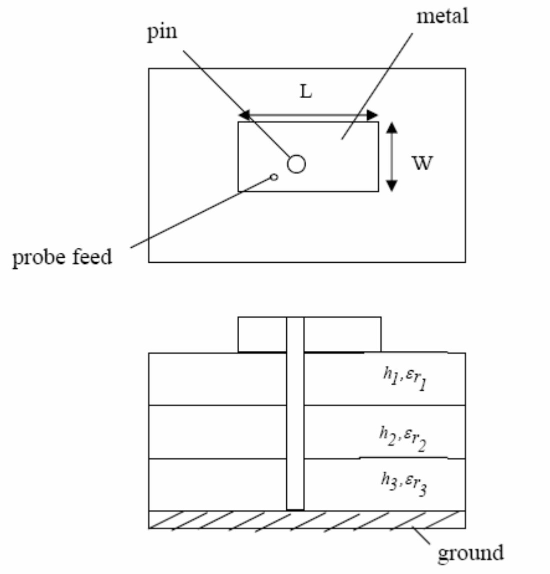

Figure 4. Pin shorted microstrip antenna for mobile communications.

5. References

[1] R. Porath, "Theory of miniaturized shorting-post microstrip antennas," IEEE Transactions, Antennas and Propagation, Vol. 48, No. 1, pp. 41–47, 2000.

[2] M. Sanad, "Effect of the shorting posts on short circuit microstrip antennas," Proceedings, IEEE Antennas and Propagation Society International Symposium, pp. 794–797, 1994.

[3] R. Garg, P. Bhartia, I. Bahl, and A. Ittipiboon, "Microstrip antenna design handbook," Artech House: London, 2001.

[4] D. M. Pozar, "Microstrip antennas," Proceedings of IEEE, Vol. 80, No 1, pp. 79–91, January 1992.

[5] T. Chakravarty, S. Biswas, A. Majumdar, and A. De, "Computation of resonant frequency of annular-ring-loaded circular patch," Microwave and Optical Technology Letters, Vol. 48, No. 3, pp. 622–626, 2006.

[6] P. Kumar, G. Singh, and S. Bhooshan, "Gap-coupled microstrip antennas," Proceedings of International Conference on Computational Intelligence and Multimedia Appications, pp. 434–437, 2007.

[7] K. P Ray, S. Ghosh, and K. Nirmala, "Compact broadband gap-coupled microstrip antennas," Proceedings of IEEE Antennas and Propagation Society International Symposium, pp. 3719–3722, July 2006.

[8] R. B. Waterhouse, S. D. Targonski, and D. M. Kokoto, "Design and performance of small printed antennas," IEEE Transactions, Antennas and Propagation, Vol. 46, pp. 1629–1633, 1998.

[9] T. K. Lo, C.-O. Ho, Y. Hwang, E. K. W. Lam, and B. Lee, "Miniature aperture-coupled microstrip antenna of

very high permittivity," Electronics Letters, Vol. 33, pp. 9−10, 1997.

[10] C. L. Tang, H. T. Chen, and K. L. Wong, "Small circular microstrip antenna with dual frequency operation," Electronics Letters, Vol. 33, No. 73, pp. 1112−1113, 1997.

[11] K. L. Wong and W. S. Chen, "Compact microstrip antenna with dual-frequency operation," Electronics Letters, Vol. 33, No. 8, pp. 646−647, 1997.

[12] T. Chakravarty and A. De, "Investigation of modes tunable circular patch radiator with arbitrarily located shorting posts," IETE Technical Review, Vol. 16, No.1, pp. 109−111, 1999.

[13] T. Chakravarty and A. De, "Design of tunable modes and dual-band circular patch antenna using shorting posts," IEE Proceedings on Microwave, Antennas and Propagation, Vol. 146, No. 3, pp. 224−228, 1999.

[14] A. Vallecchi, G. B. Gentili, and M. Calamia, "Dual-band dual polarization microstrip antenna," Proceedings, IEEE International Symposium, pp. 134−137, 2003.

[15] R. Waterhouse, "Small microstrip patch antenna," Electronics Letters, Vol. 31, pp. 604−605, 1995.

[16] S. Dey and R. Mitra, "Compact microstrip patch antennas," Microwave and Optical Technology Letters, Vol. 13, pp. 12−14, 1996.

[17] H. K. Kan and R. Waterhouse, "Size reduction technique for shorted patches," Electronics Letters, Vol. 35, pp. 948−949, 1999.

[18] E. Lee, P. S. Hall, and P. Gardner, "Compact dual-band dual-polarization microstrip patch antennas," Electronics Letters, Vol. 35, pp. 1034−1036, 1999.

[19] S. K. Satpathy, G. Kumar, and K. P. Ray, "Compact shorted variations of triangular microstrip antennas," Electronics Letters, Vol. 34, No. 8, pp. 709−711.

[20] P. Kumar, G. Singh, and S. Bhooshan, "Pin shorted rectangular patch microstrip antenna for mobile communication," Proceedings of National Conference on Wireless and Optical Communication, pp. 77−79, 2007.

[21] P. Kumar, V. K. Dwevidi, G. Singh and S. Bhooshan, "Miniaturization of gap-coupled microstrip antennas," Proceedings, International Conference on Recent Advances in Microwave and Applications (Microwave-08), India, pp. 489−491, 2008.

[22] P. Kumar, V. K. Dwivedi, G. Singh and S. Bhooshan, "Input impedance of gap-coupled circular microstrip antennas loaded with shorting post," Proceedings, Progress in Electromagnetics Research Symposium, Beijing, China, pp. 1634−1638, 2009.

[23] P. Kumar and G. Singh, "Computation of mutual coupling for gap-coupled circular patch antennas loaded with shorting post," International Journal of Electronics Engineering, Vol. 1, No. 1, pp. 99−102, 2009.

[24] P. Kumar, G. Singh, T. Chakravarty, and S. Bhooshan, "Mutual coupling between gap-coupled pin shorted circular patch antennas," Proceedings, IEEE Applied Electromagnetic Conference, pp. 1−3, 2007.

[25] A. Sharma and G. Singh, "Design of single pin shorted three-dielectric-layered substrates rectangular patch microstrip antenna for communication systems," Progress In Electromagnetics Research Letters, Vol. 2, pp. 157–165, 2008.

Engineering, 2009, 1, 1-54
Published Online June 2009 in SciRes (http://www.SciRP.org/journal/eng/).

A Novel Solution Based on Differential Evolution for Short-Term Combined Economic Emission Hydrothermal Scheduling

Chengfu Sun[1], Songfeng Lu[2]
School of Computer Science and Technology,
Huazhong University of Science and Technology, Wuhan, China
Email: [1]*ajason509@smail.hust.edu.cn*, [2]*lusongfeng@sina.com*
Received April 17, 2009; *revised May* 13, 2009; *accepted May* 18, 2009

Abstract

This paper presents a novel approach based on differential evolution for short-term combined economic emission hydrothermal scheduling, which is formulated as a bi-objective problem: 1) minimizing fuel cost and 2) minimizing emission cost. A penalty factor approach is employed to convert the bi-objective problem into a single objective one. In the proposed approach, heuristic rules are proposed to handle water dynamic balance constraints and heuristic strategies based on priority list are employed to repair active power balance constraints violations. A feasibility-based selection technique is also devised to handle the reservoir storage volumes constraints. The feasibility and effectiveness of the proposed approach are demonstrated and the test results are compared with those of other methods reported in the literature. Numerical experiments show that the proposed method can obtain better-quality solutions with higher precision than any other optimization methods. Hence, the proposed method can well be extended for solving the large-scale hydrothermal scheduling.

Keywords: Hydrothermal Power Systems, Economic Load Scheduling, Combined Economic Emission Scheduling, Differential Evolution

1. Introduction

One of the major problems existing today on electric power systems is the optimum scheduling of hydrothermal plants. Short-term hydrothermal scheduling is a daily planning task in power systems and its main objective is to minimize the total operational cost subjected to a variety of constraints of hydraulic and power system network. As the source for hydropower is the natural water resources, the operational cost of hydroelectric plants is insignificant. Thus, the objective of minimizing the operational cost of a hydrothermal system essentially reduces to minimize the fuel cost of thermal plants over a scheduling horizon while satisfying various constraints. Due to increasing concern over atmospheric pollution, harmful emission produced by the thermal units must be minimized simultaneously. So a revised economic power dispatch program considering both the fuel cost and emission is required. But minimizing pollution may lead to an increase in generation cost and vice versa.

The importance of the generation scheduling problem of hydrothermal systems is well recognized. Therefore, many methods have been devised to solve this difficult optimization problem for several decades. Some of these methods are dynamic programming methodology [1], linear programming [2], and decomposition techniques [3]. Recently, aside from the above methods, optimal hydrothermal scheduling problems have been solved by meta-heuristic approaches such as genetic algorithm [4–6], cultural algorithm [7] and particle swarm optimization [8] etc. Various heuristic methods such as heuristic search technique [9], fuzzy satisfying evolutionary programming procedures [10] and fuzzy decision-making stochastic technique [11] have been applied to solve multi-objective short-term hydrothermal scheduling problems. Because these meta-heuristic optimization methods are able to provide higher quality solutions, they have received more interest. One of these meta-heuristic optimization methods is differential evolution (DE) [13].

A new optimization method known as DE, which is a stochastic search algorithm based on population cooperation and competition of individuals, has gradually become more popular and has been successfully applied to solve optimization problems particularly involving non-smooth objective function. DE combines the simple arithmetic operators with the classical evolution operators of crossover, mutation and selection to evolve from a randomly generated population to a final solution. The DE algorithm has been applied to various fields of power system optimization such as dynamic economic dispatch with valve-point effects [14], hydrothermal scheduling [15], economic dispatch with non-smooth and non-convex cost functions [16], optimal reactive power planning in large-scale distribution system [17], and economic dispatch problem [18].

This work presents a novel approach based on differential evolution to solve short-term combined economic emission scheduling of cascaded hydrothermal systems. Moreover, heuristic rules are proposed to handle the water dynamic balance constraints and heuristic strategies based on priority list are employed to handle active power balance constraints. At the same time, a feasibility-based selection technique is devised to handle the reservoir storage volumes constraints. The results obtained with the proposed approach were analyzed and compared with the results of the differential evolution [12] and interactive fuzzy satisfying method based on evolutionary programming [10] reported in the literature.

The remainder of the paper is organized as follows. The formulation of the short-term combined economic emission scheduling of hydrothermal power systems with cascaded reservoirs is introduced in Section 2, while Section 3 explains the classical DE. Section 4 describes the implementation of the proposed method for solving the short-term hydrothermal scheduling and outlines heuristic strategies to handle water dynamic balance constraints and active power balance constraints. Section 5 presents the optimization results for the short-term hydrothermal power systems scheduling. Lastly, section 6 draws the conclusions.

2. Problem Formulation

The hydrothermal scheduling problem combined economic emission scheduling is formulated as a bi-objective optimization problem. It is concerned with the attempt to minimize the fuel cost and as well as the emission of thermal units, while making full use of the availability of hydro-resources as much as possible. In the formulation of the hydrothermal scheduling problem, the following objectives and constraints must be taken into account and the equality and inequality constraints must simultaneously be satisfied.

2.1. Notations

In order to formulate the hydrothermal scheduling problem mathematically, the following notations is introduced first:

$f_{it}^{v}(P_{sit})$ fuel cost of thermal plant i including valve point loading

$e_{it}^{v}(P_{sit})$ emission of thermal plant i including valve point loading

a_{si}, b_{si}, c_{si} e_{si}, f_{si} coefficients of thermal generating plant i

$\alpha_{si}, \beta_{si}, \gamma_{si}, \eta_{si,} \delta_{si}$ emission coefficients of thermal plant i

T total time intervals over scheduling horizon

N_s, N_h number of thermal and hydro plants respectively

P_{hjt} power generation of hydro generating plant j at time interval t

P_{sit} power generation of thermal generating unit i at time interval t

P_{Dt} power demand at time interval t

P_{Lt} total transmission loss at time interval t

$C_{1j}, C_{2j}, C_{3j}, C_{4j}, C_{5j}, C_{6j}$ power generation coefficients of hydro plant j

V_{hjt} storage volume of reservoir j at time interval t

Q_{hjt} water discharge rate of the j th reservoir at time t.

$P_{si}^{\min}$ $P_{si}^{\max}$ minimum and maximum power generation by thermal plant i

$P_{si}^{\min}$ $P_{si}^{\max}$ minimum and maximum power generation by hydro plant j

$V_{hj}^{\min}, V_{hj}^{\max}$ minimum and maximum storage volumes of reservoir j

I_{hjt} inflow of hydro reservoir j at time interval t

S_{hjt} spillage discharge rate of hydro plant j at time interval t

τ_{mj} water transport delay from reservoir m to j

R_{uj} number of upstream hydro generating plants directly above reservoir j

G current iteration generation

N_p number of the parameter vectors

2.2. Objective Functions

2.2.1. Economic Scheduling

In this paper, non-smooth fuel cost function of thermal generating unit with valve-point effects is considered.

$$f_{it}^{v}\left(P_{sit}\right)=a_{si}+b_{si}*P_{sit}+c_{si}*P_{sit}^{2}+\left|e_{si}*\sin\left\{f_{si}*\left(P_{si}^{\min}-P_{sit}\right)\right\}\right| \quad \mathbf{(1)}$$

For a given hydrothermal system, the problem may be described as minimization of total fuel cost associated to the on-line N units for T intervals in the given time horizon as defined by Equation (2) under a set of operating constraints as follows:

$$F=\min\sum_{t=1}^{T}\sum_{i=1}^{N_s}[f_{it}^{v}\left(P_{sit}\right)] \quad \mathbf{(2)}$$

2.2.2. Emission Scheduling

In this study, the amount of emission from each generator can be described as the sum of a quadratic and an exponential function.

$$e_{it}^{v}\left(P_{sit}\right)=\alpha_{si}+\beta_{si}*P_{sit}+\gamma_{si}*P_{sit}^{2}+\eta_{si}*\exp\left(\delta_{si}*P_{sit}\right) \quad \mathbf{(3)}$$

The economic emission scheduling problem can be expressed as the minimization of total amount of emission release defined by Equation(4) as

$$E=\sum_{t=1}^{T}\sum_{i=1}^{N_s}[e_{it}^{v}\left(P_{sit}\right)] \quad \mathbf{(4)}$$

2.3. Constraints

While minimizing the above two objectives, the following constraints must be satisfied simultaneously.

Active power balance constraint

$$\sum_{i=1}^{N_s}P_{sit}+\sum_{j=1}^{N_h}P_{hjt}-P_{Dt}-P_{Lt}=0 \quad \mathbf{(5)}$$

The hydroelectric generation is a function of water discharge rate and reservoir water head, which can be expressed as follows:

$$P_{hjt}=C_{1j}*V_{hjt}^{2}+C_{2j}*Q_{hjt}^{2}+C_{3j}*V_{hjt}*Q_{hjt}+C_{4j}*V_{hjt}+C_{5j}*Q_{hjt}+C_{6j} \quad \mathbf{(6)}$$

Generation limits constraints

$$P_{si}^{\min}\le P_{sit}\le P_{si}^{\max} \quad \mathbf{(7)}$$

$$P_{hj}^{\min}\le P_{hjt}\le P_{hj}^{\max} \quad \mathbf{(8)}$$

1) Reservoir storage volumes constraints

$$V_{hj}^{\min}\le V_{hjt}\le V_{hj}^{\max} \quad \mathbf{(9)}$$

2) Discharge rates limit

$$Q_{hj}^{\min}\le Q_{hjt}\le Q_{hj}^{\max} \quad \mathbf{(10)}$$

3) Water dynamic balance constraints

$$V_{hjt}=V_{hj,t-1}+I_{hjt}-Q_{hjt}-S_{hjt}+\sum_{m=1}^{R_{uj}}\left(Q_{hm,t-\tau_{mj}}+S_{hm,t-\tau_{mj}}\right) \quad \mathbf{(11)}$$

3. Overview of Differential Evolution Algorithm

As a population-based and stochastic global optimizer, differential evolution (DE) is one of the latest evolutionary optimization methods proposed by Storn and Price [13]. In a DE algorithm, candidate solutions are randomly generated and evolved to final individual solution by simple technique combining simple arithmetic operators with the classical events of mutation, crossover and selection. One of the most frequently used mutation strategies, named “DE/rand/1/bin”, will be employed in this paper.

3.1. Mutation Operation

The essential ingredient in the mutation operation is the vector difference. For each target vector $X_i^G\left(i=1,2,\cdots,N_p\right)$, the weighted difference between two randomly selected vectors X_l^G and X_m^G is added to a third randomly selected vector X_k^G to generate a mutated vector V_i^G using the following equation.

$$V_i^G=X_k^G+F*\left(X_l^G-X_m^G\right) \quad \mathbf{(12)}$$

where X_k^G, X_l^G and X_m^G are randomly selected vectors and $i\ne k\ne l\ne m$; The mutation factor $F>0$ is a user chosen parameter to control the amplification of the difference between two individuals so as to avoid search stagnation.

3.2 Crossover Operation

Following the mutation phase, the crossover operation is performed in order to increase the diversity in the searching process.

$$U_{i,j}^G=\begin{cases}V_{i,j}^G & if \quad \left(\eta_j\le CR\right) \quad or \quad \left(j=q\right)\\ X_{i,j}^G & otherwise\end{cases} \quad \mathbf{(13)}$$

where $\eta_j\in\left[0,1\right]$, generated anew for each value of j, is a uniformly distributed random number. The crossover factor $CR\in\left[0,1\right]$ controls the diversity of the population. $X_{i,j}^G, V_{i,j}^G$ and $U_{i,j}^G$ are the j th parameter of the i th target vector, mutant vector and trial vector at generation G, respectively.

3.3. Selection Operation

Thereafter, a selection operator is applied to compare the fitness function value of two competing vectors, namely, target and trial vectors to determine who can survive for the next generation.

$$X_i^{G+1} = \begin{cases} U_i^G & if \quad f\left(U_i^G\right) \le f\left(X_i^G\right) \\ X_i^G & otherwise \end{cases} \quad \textbf{(14)}$$

where f denotes the fitness function under optimization (minimization).

4. Implementation of the Proposed Method for Solving the Short-Term Hydrothermal Scheduling

In this section, the procedures for solving short-term scheduling problem of hydrothermal power system are described in details. Especially, heuristic strategies will be given to handle constraints of hydrothermal scheduling problem. The process of the proposed method for solving hydrothermal scheduling can be summarized as follows.

4.1. Structure of Parameter Solution Vector

The structure of a solution for hydrothermal scheduling problem is composed of a set of decision variables which represent the discharge rate of the each hydro plant and the power generated by each thermal unit over the scheduling horizon.

$$P_k = \begin{bmatrix} Q_{h11} & Q_{h21} & \cdots & Q_{hN_h1} & P_{s11} & P_{s21} & \cdots & P_{sN_s1} \\ Q_{h12} & Q_{h22} & \cdots & Q_{hN_h2} & P_{s12} & P_{s22} & \cdots & P_{sN_s2} \\ \vdots & \vdots & \cdots & \vdots & \vdots & \vdots & \cdots & \vdots \\ Q_{h1T} & Q_{h2T} & \cdots & Q_{hN_hT} & P_{s1T} & P_{s2T} & \cdots & P_{sN_sT} \end{bmatrix} \quad \textbf{(15)}$$

The elements Q_{hjt} and P_{sit} P_{sit} ($j = 1, 2 \cdots, N_h$; $i = 1, 2, \cdots, N_s$) are subjected to the water discharge rate and the thermal generating capacity constraints as depicted in Equation. (10) and (7), respectively. The water discharge rate of the j th hydro plant in the dependent interval must satisfy the water dynamic balance constraints in Equation (11).

4.2. Initialization Parameter Vectors

During the initialization process, the candidate solution of each parameter vector $X_k\left(k = 1, 2, \cdots, N_p\right)$ is randomly initialized within the feasible range as follows:

$$Q_{hjt} = Q_{hj}^{\min} + r_q * \left(Q_{hj}^{\max} - Q_{hj}^{\min}\right) \quad \textbf{(16)}$$

$$P_{sit} = P_{si}^{\min} + r_s * \left(P_{si}^{\max} - P_{si}^{\min}\right) \quad \textbf{(17)}$$

where r_q and r_s are the random numbers uniformly distributed in $[0,1]$.

4.3. Combined Economic and Emission Scheduling

The short-term combined economic emission scheduling of hydrothermal power systems with cascaded reservoirs is a bi-objective problem with the attempt to minimize simultaneously fuel cost and emission of thermal plants. The bi-objective optimization problem can be transformed into a single objective one by introducing price penalty factors h_t . For more details, see Ref. [12].

4.4. Solution Modification

New values of water discharge rate $Q_{hj,t+1}$ and power generation $P_{si,t+1}$ are generated through mutation and crossover operation according to Equations (12) and (13), respectively. The new values are not always guaranteed to satisfy the constraints Equations (10) and (7), respectively. If any value violating its constraint is modified in the following way:

$$Q_{hj,t+1} = \begin{cases} Q_{hj}^{\min} & if \quad Q_{hj,t+1} < Q_{hj}^{\min} \\ Q_{hj,t+1} & if \quad Q_{hj}^{\min} \le Q_{hj,t+1} \le Q_{hj}^{\max} \\ Q_{hj}^{\max} & if \quad Q_{hj,t+1} > Q_{hj}^{\max} \end{cases} \quad \textbf{(18)}$$

$$P_{si,t+1} = \begin{cases} P_{si}^{\min} & if \quad P_{si,t+1} < P_{si}^{\min} \\ P_{si,t+1} & if \quad P_{si}^{\min} \le P_{si,t+1} \le P_{si}^{\max} \\ P_{si}^{\max} & if \quad P_{si,t+1} > P_{si}^{\max} \end{cases} \quad \textbf{(19)}$$

4.5. Heuristic Strategies to Handle Equality Constraints

4.5.1. Handling Water Dynamic Balance Constraints

To meet exactly the restrictions on the initial and final reservoir storage, the water discharge rate of the j th hydro plant in the dependent interval d is then calculated using Equation(21). The dependent water discharge rate must satisfy the constraints in Equation (10). Assuming the spillage in Equation (11) to be zero for simplicity, the water dynamic balance constraints are

$$V_{hj0} - V_{hjT} = \sum_{t=1}^{T} Q_{hjt} - \sum_{t=1}^{T}\sum_{m=1}^{R_{uj}}\left(Q_{hm,t-\tau_{mj}}\right) - \sum_{t=1}^{T} I_{hjt} \quad \textbf{(20)}$$

where V_{hj0} is the initial storage volume of reservoir j; V_{hjT} is the final storage volume of reservoir j. The procedures for repairing the water dynamic balance violations in hydrothermal scheduling are as follows:

Step 1: Set $j=1$.

Step 2: Randomly choose a time interval d as a dependent interval and set $count=1$.

Step 3: In order to meet equality constraint in Equation (11), the water discharge rate of the jth hydro plant Q_{hjd} in the dependent interval d is then calculated by

$$Q_{hjd} = V_{hjo} - V_{hjT} - \sum_{\substack{t=1 \\ t \neq d}}^{T} Q_{hjt} + \sum_{t=1}^{T} \sum_{m=1}^{R_{uj}} \left(Q_{hm,t-\tau_{mj}} \right) + \sum_{t=1}^{T} I_{hjt} \quad \textbf{(21)}$$

If the computed Q_{hjd} doesn't violate the constraints in Equation (10) then go to step 7; otherwise go to the next step

Step 4: Change Q_{hjd} using Equation(18).

Step 5: A new random time interval d is chosen ensuring that it is not repeatedly selected and $count = count + 1$.

Step 6: If $count \le T$, then go to step 3; otherwise go to next step.

Step 7: $j = j+1$, if $j \le N_h$, then go to step 2; otherwise go to next step.

Step 8: The modification process is terminated.

4.5.2. Handling Active Power Balance Constraints

The power balance equality constraints in Equation(5) still remain to be resolved after the water dynamic balance constraints are preserved. The heuristic strategy based on priority list is proposed for handling the power balance constraints. In this paper, priority list is created according to each thermal plant parameter. When the thermal plant is at its maximum output power, the average full-load cost α_{it} of thermal plant i at time interval t is defined by

$$\alpha_{it} = \frac{\omega_1 * f_{it}^{v}\left(P_{si}^{\max}\right) + \omega_2 * h_t * e_{it}^{v}\left(P_{si}^{\max}\right)}{P_{si}^{\max}} \quad \textbf{(22)}$$

where h_t is price penalty factor at time interval t, ω_1 and ω_2 are the weight factors. The detail procedures for handling active power balance constraints are as follows:

Step 1: Calculate the average full-load cost α_{it} using Equation(22) at time interval t. Arrange them in ascending order of α_{it} to obtain a priority list $PL(t)$.

Step 2: Set $t=1$.

Step 3: Set $temp\_PL(t) = PL(t)$.

Step 4: The amount of active power balance violation at time interval t is calculated by $t=1 \Delta P^t = \sum_{i=1}^{N_s} P_{sit} - (\sum_{j=1}^{N_h} P_{hjt} + P_{Dt})$. In this paper the power loss is not considered for simplicity.

Step 5: If $\Delta P^t = 0$, go to Step 14; if $\Delta P^t > 0$, go to Step 6; if $\Delta P^t < 0$, go to Step 10.

Step 6: Set $m=1$.

Step 7: Set power of the generator unit k with highest α_{it} in $temp\_PL(t)$ to be $P_k^t = P_{sk}^{\min}$. Then delete thermal unit k from $temp\_PL(t)$.

Step 8: Calculate the total power P_{sum}^t generated by all thermal units at time interval t. If $P_{sum}^t \le \sum_{j=1}^{N_h} P_{hjt} + P_{Dt}$, set $P_k^t = P_{si}^{\min} + (\sum_{j=1}^{N_h} P_{hjt} + P_{Dt} - P_{sum}^t)$ and go to step 14; otherwise set $P_k^t = P_{sk}^{\min}$.

Step 9: $m = m+1$. If $m \le N_s$, then go to Step 7; otherwise go to Step 14

Step 10: Set $m=1$.

Step 11: Set power of the generator unit k with lowest α_{it} in $temp\_PL(t)$ to be $P_k^t = P_{sk}^{\max}$. Then delete thermal unit k from $temp\_PL(t)$.

Step 12: Calculate the total power P_{sum}^t generated by all thermal units at time interval t. If $P_{sum}^t \ge \sum_{j=1}^{N_h} P_{hjt} + P_{Dt}$, set $P_k^t = P_{si}^{\max} + (\sum_{j=1}^{N_h} P_{hjt} + P_{Dt} - P_{sum}^t)$ and go to step 14; otherwise set $P_k^t = P_{sk}^{\max}$.

Step 13: $m = m+1$. If $m \le N_s$, then go to Step 11; otherwise go to Step 14.

Step 14: $t = t+1$. If $t \le T$, then go to Step 3; otherwise go to Step 15.

Step 15: The modification process is terminated.

4.6. Selection Based Technique for Handling Reservoir Storage Volumes Constraints

In this work, the feasibility-based selection rules are applied to the proposed approach for handling the inequality constraints of reservoir storage volumes constraints. The procedures for repairing the reservoir storage volumes constraints are as follows:

Step 1: The overall reservoir storage volumes constraints violation of solution x is $CV(x)$, which is defined as

$$CV(x) = \sum_{t=1}^{T}\sum_{j=1}^{N_h}\left[\max\left(0, V_{hjt} - V_{hj}^{\max}, V_{hj}^{\min} - V_{hjt}\right)\right] \quad \textbf{(23)}$$

Step 2: (1) If both parameter vectors are feasible, then the one with the better fitness value wins. (2) Otherwise, if both parameter vectors are infeasible, then the one with the less value of $CV(x)$ wins. (3) Otherwise, the feasible parameter vectors always wins.

5. Simulation Results

In this section, a test system consisting of a multi-chain cascade of four hydro units and three thermal units is studied to demonstrate the feasibility and effectiveness of the proposed method for solving short-term hydrothermal scheduling with cascaded reservoirs. The entire scheduling period is chosen as one day with 24 intervals of 1 hour each. The load demand of the system, hydro and thermal unit coefficients, reservoir inflows and reservoir limits are taken from the literature [10].

In order to compare with Ref. [12], the parameters for population size and maximum number of generations allowed are set as follows: $N_p = 70$, maximum number of iterations $Maxiter = 400$, respectively. Before proceeding to the simulated calculation, careful selection of mutation and crossover factor is important to produce a competent result. The following values for mutation and crossover factor were selected by parameter setting through trial and error for the present test system: mutation factor $F = 0.44$, crossover factor $CR = 0.85$. Under the chosen parameters, it has been found to provide optimum results. The proposed approach is performed 10 trials for different cases of hydrothermal scheduling.

According to [12], the total cost can be presented as follows for a trade off between fuel cost and emission cost.

$$TC = \omega_1 * F\left(P_{sit}\right) + \omega_2 * h_t * E\left(P_{sit}\right) \quad \textbf{(24)}$$

where ω_1 and ω_2 are the weight factors.

The results of proposed method for obtaining combined economic emission scheduling (CEES, $\omega_1 = 1$ and $\omega_2 = 1$) solution are illustrated as follows. In this case, the values α_{it} of thermal unit 1, 2 and 3 at time intervals 1, 2, 3, 4, 5, 6, 24 are 4.8695, 6.2728 and 13.2897, while at other time intervals they are 7.1634, 11.8597 and 31.3219. But the priority list is $\{1,2,3\}$ over the entire scheduling horizon. The thermal unit 1 with the lowest α_{it} will have the highest priority to be dispatched more generation power. The optimal hydrothermal generation schedule for CEES is shown in Figure 1 and the optimal hourly water discharge rate obtained by the proposed method for CEES is presented in Figure 2.

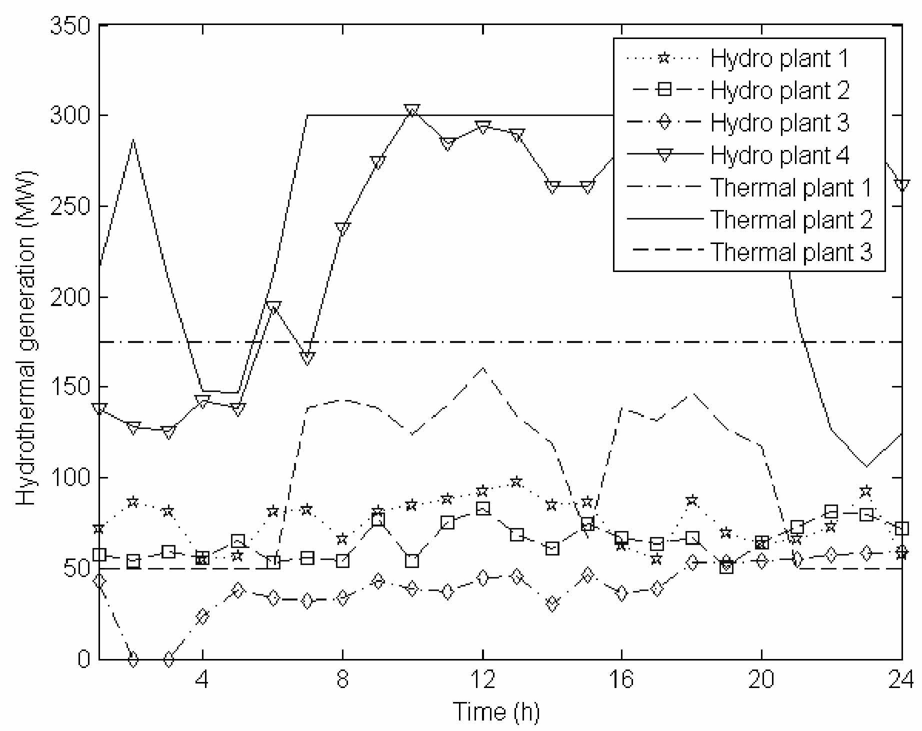

Figure 1. Hydrothermal generation (MW) schedule for CEES.

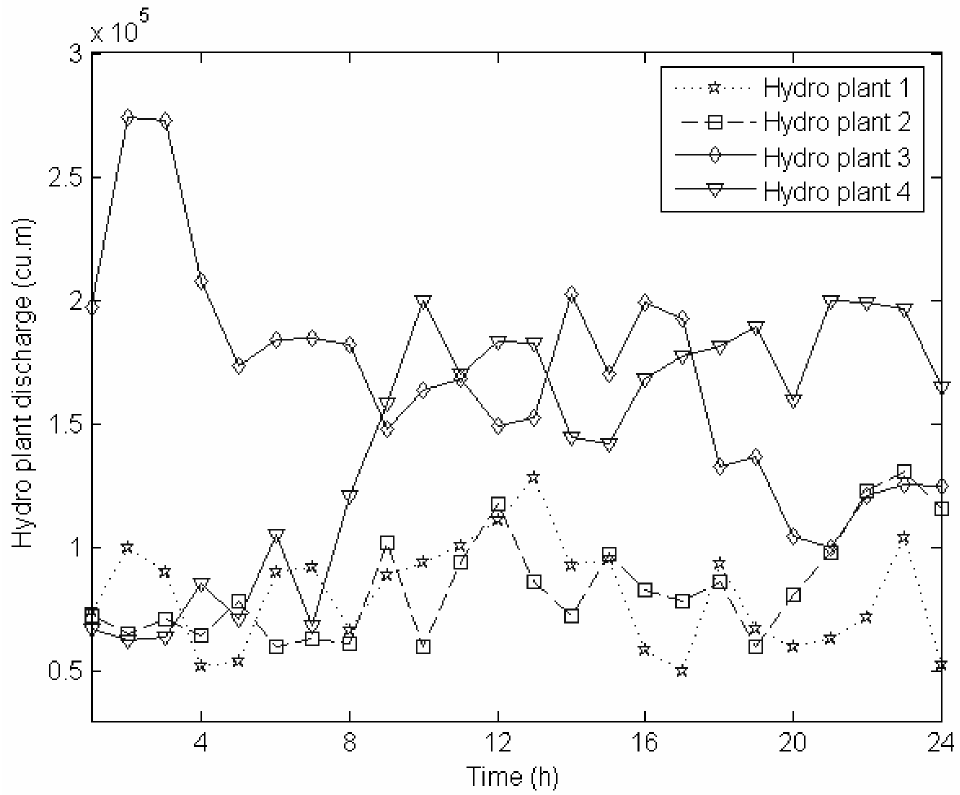

Figure 2. Hourly hydro plant discharge (m^3) for CEES.

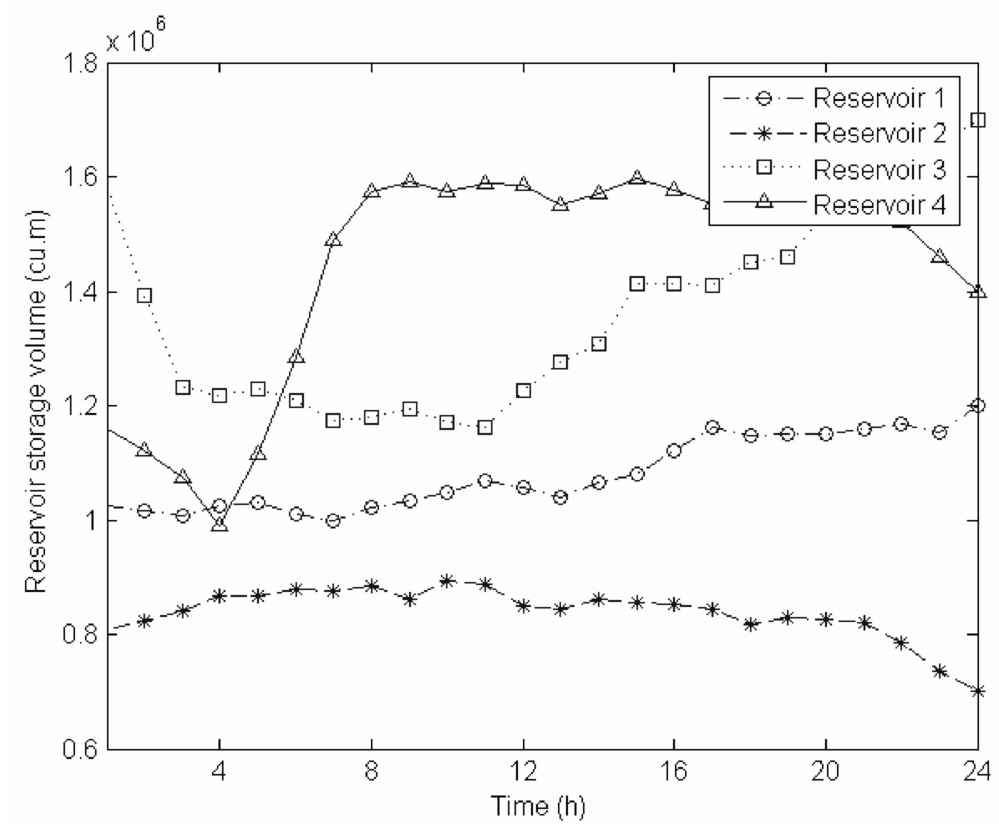

Figure 3. Reservoir storage volumes for CEES.

The trajectories of reservoir storage volumes for CEES are shown in Figure 3. Table 1 shows that using the proposed method optimal fuel cost is found to be $44265.00, while amount emission is found to be 18060.00 lb.

In Table 1, the optimal solutions of the fuel cost and emission cost for economic load scheduling (ELS, $\omega_1 = 1$ and $\omega_2 = 0$), economic emission scheduling (EES, $\omega_1 = 0$ and $\omega_2 = 1/h_t$) and CEES obtained from the proposed approach have been compared with those of DE [12]. From the results it is quite evident that the proposed method provides better solutions for short-term combined economic emission hydrothermal scheduling with cascaded hydro reservoirs. Table 2 presents the best, worst and mean value of fuel cost and emission of CEES obtained by differential evolution without priority list, particle swarm optimization without priority list and the proposed approach. From the analysis of results in Table 2, it can be seen that the proposed approach can produce valuable trade off solutions for CEES. It also shows that the two objectives of minimizing the fuel cost and emission cost are of conflicting nature, that is to say, minimizing pollution increases fuel cost and vice versa. From the results of CEES, it clearly sees that with some compromise in fuel cost, it is possible to obtain huge reduction in emission.

It can be seen clearly from Table 1 that the proposed method yields much better results in terms of fuel cost, the amount of emission than known optimization methods reported in the literature. It is also very important to note that compared with the results of fuzzy satisfying [10] the better results from [12] are obtained based on violating the constraints of the test system, such as the results of Table 1, Table 3 and Table 5 in Ref. [12], from which it is clearly shown that the power generation of thermal unit P_{s1} violates its constraint which is $20 \le P_{s1} \le 175$ at some time intervals. However, in this study we obtain even better results while strictly satisfying all constraints of the test system.

6. Conclusions

In this paper, a novel approach in combination with novel equality constraint handling techniques has been successfully introduced to solve hydrothermal scheduling with non-smooth fuel and emission cost functions. The major advantages of this novel method are as follows: 1) In order to handle constraints effectively, heuristic rules are proposed to handle water dynamic balance constraints and heuristic strategies based on priority list are employed to handle active power balance constraints; 2) The feasibility-based selection rules are developed to handle the reservoir storage volumes constraints. Additionally, the improved heuristic strategies can be simply incorporated into differential evolution. Hence the proposed method does not require the use of penalty functions and explores the optimum solution at a relatively lesser computational effort. Numerical experiments show that the proposed method can obtain better-quality solutions with higher precision than any other optimization methods reported in the literature. Hence, the proposed method can well be extended for solving the large-scale hydrothermal scheduling.

7. Acknowledgements

The authors gratefully acknowledge the financial supports from National Natural Science Foundation of China under Grant no. 10876012. The authors thank the anonymous Reviewers and Editors for constructive and detailed comments.

Table 1. Comparison of cost for ELS, EES and CEES by proposed method and DE.

		Fuel cost ($)	Emission (lb)
The proposed method	ELS	42766.00	31002.00
	EES	46066.00	17655.00
	CEES	44265.00	18060.00
Differential evolution (DE)	ELS	43500.00	21092.00
	EES	51449.00	18257.00
	CEES	44914.00	19615.00

Table 2. Comparison of cost of CEES by proposed method, DE and PSO.

		Best Value	Worst Value	Mean Value
The proposed method	Fuel cost($)	44265	45258	44622
	Emission(lb)	17797	18255	18069
Differential evolution without priority list	Fuel cost($)	47999	48792	48390
	Emission(lb)	17076	17716	17362
PSO without priority list	Fuel cost($)	45670	46895	46530
	Emission(lb)	16980	17807	17295

8. References

[1] J. Tang and B. Peter, "Hydrothermal scheduling via extended differential dynamic programming and mixed coordination," IEEE Transactions on Power System, Vol. 10, pp. 2021−2028, 1995.

[2] M. Piekutowski, "Optimal short-term scheduling for a large-scale cascaded hydro system," IEEE Transactions on Power System, Vol. 9, pp. 805−811, 1994.

[3] M. V. F. Pereira and L. M. V. G. Pinto, "A decomposition approach to the economic dispatch of the hydrothermal systems," IEEE Transactions on Power Systems, Vol. 101, pp. 3851−3860, 1982.

[4] M. Ramirez and P. E. Ontae, "The short-term hydrothermal coordination via genetic algorithms," Electric Power Components and Systems, Vol. 34, pp. 1−19, 2006.

[5] E. Gil, J. Bustos, and H. Rudnick, "Short-term hydrothermal generation scheduling model using a genetic algorithm," IEEE Transactions on Power System, Vol. 18, pp. 1256−1264, 2003.

[6] X. Yuan and Y. Yuan, "A hybrid chaotic genetic algorithm for short-term hydro system scheduling," Mathematics and Computers in Simulation, Vol. 59, pp. 319−327, 2002.

[7] X. Yuan and Y. Yuan, "Application of cultural algorithm to generation scheduling of hydrothermal systems," Energy Conversion and Management, Vol. 47, pp. 2192−2201, 2006.

[8] B. Yu, X. Yuan, and J. Wang, "Short-term hydro-thermal scheduling using particle swarm optimization method," Energy Conversion and Management, Vol. 48, pp. 1902−1908, 2007.

[9] J. S. Dhillon and D.P. Kothari, "Multi-objective short-term hydrothermal scheduling based on heuristic search technique," Asian Journal of Information Technology, Vol. 6, pp. 447−454, 2007.

[10] M. Basu, "An interactive fuzzy satisfying method based on evolutionary programming technique for multi-objective short-term hydrothermal scheduling," Electric Power Systems Research, Vol. 69, pp. 277−285, 2004.

[11] J. S. Dhillon, S. C. Parti, and D. P. Kothari, "Fuzzy decision-making in stochastic multi-objective short-term hydrothermal scheduling," IEE Proceedings of Generation Transmission and Distribution, Vol. 149, pp. 191−200, 2002.

[12] K. K. Mandal and N. Chakraborty, "Short-term combined economic emission scheduling of hydrothermal power systems with cascaded reservoirs using differential evolution," Energy Conversion and Management, Vol. 50, pp. 97−104, 2009.

[13] R. Storn and K. Price, "Differential evolution–a simple and efficient heuristic for global optimization over continuous spaces," Journal of Global Optimization, Vol. 11, pp. 341−359, 1997.

[14] X. H. Yuan, L. Wang, Y. C. Zhang, and Y. B. Yuan, "A hybrid differential evolution method for dynamic economic dispatch with valve-point effects," Expert System with Application, Vol. 36, pp. 4042−4048, 2009.

[15] X. H. Yuan, B. Cao, B. Yang, and Y. B. Yuan. "Hydrothermal scheduling using chaotic hybrid differential evolution", Energy Conversion and Management, Vol. 49, pp. 3627−3633, 2008.

[16] S. K. Wang, J. P. Chiou, and C. W. Liu, "Non-smooth/non-convex economic dispatch by a novel hybrid differential evolution algorithm," IEE Proceeding Generation Transmission and Distribution, Vol. 1, pp. 793−803, 2007.

[17] C. F. Changa, J. J. Wong, J. P. Chiou, and C. T. Su, "Robust searching hybrid differential evolution method for optimal reactive power planning in large-scale distribution sytems," Electric Power Systems Research, Vol. 77, pp. 430−437, 2007.

[18] J. P. Chiou, "Variable scaling hybrid differential evolution for large-scale economic dispatch problems," Electric Power Systems Research, Vol. 77, pp. 212−218, 2007.

Call for Papers

The 4th International Conference on Bioinformatics and Biomedical Engineering (iCBBE 2010)

June 18-20, 2010 Chengdu, China

The 4th International Conference on Bioinformatics and Biomedical Engineering (iCBBE 2010) will be held from June 18th to 20th, 2010 in Chengdu, China. You are welcome to share your recent advances and achievements in all aspects of bioinformatics and biomedical engineering on the conference. **And all accepted papers in iCBBE 2010 will be published by IEEE and indexed by Ei Compendex and ISTP.**

Topics

Bioinformatics and Computational Biology

- Protein structure, function and sequence analysis
- Protein interactions, docking and function
- Computational proteomics
- DNA and RNA structure, function and sequence analysis
- Gene regulation, expression, identification and network
- Structural, functional and comparative genomics
- Computer aided drug design
- Data acquisition, analysis and visualization
- Algorithms, software, and tools in Bioinformatics
- Any novel approaches to bioinformatics problems

Biomedical Engineering

- Biomedical imaging, image processing & visualization
- Bioelectrical and neural engineering
- Biomechanics and bio-transport
- Methods and biology effects of NMR/CT/ECG technology
- Biomedical devices, sensors and artificial organs
- Biochemical, cellular, molecular and tissue engineering
- Biomedical robotics and mechanics
- Rehabilitation engineering and clinical engineering
- Health monitoring systems and wearable system
- Bio-signal processing and analysis
- Biometric and bio-measurement
- Biomaterial and biomedical optics
- Other topics related to biomedical engineering

Special Sessions

Biomedical imaging
Biostatistics and biometry
The information technology in bioinformatics
Environmental pollution & public health

Important Dates

Paper Due: Oct.30, 2009
Acceptance Notification: Dec.31, 2009
Conference: June 18-20, 2010

Sponsors

IEEE Eng. in Medicine and Biology Society, USA
Gordon Life Science Institute, USA
University of Lowa, USA
Wuhan University, China
Sichuan University, China
Journal of Biomedical Science and Engineering, USA

Contact Information

Website:http://www.icbbe.org/2010/
E-mail: submit@icbbe.org

Call for Papers

ENGINEERING

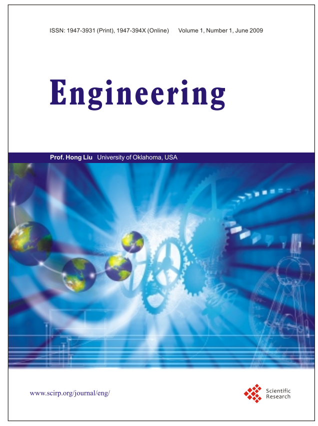

A Journal Published by Scientific Research Publishing, USA

www.scirp.org/journal/eng

ENGINEERING is an international journal dedicated to the latest advancement of engineering. The goal of this journal is to provide a platform for engineers and academicians all over the world to promote, share, and discuss various new issues and developments in different areas of engineering. All manuscripts must be prepared in English, and are subject to a rigorous and fair peer-review process. Accepted papers will immediately appear online followed by printed hard copy. The journal publishes original papers including but not limited to the following fields:

- Aerospace Engineering
- Agricultural Engineering
- Chemical Engineering
- Civil Engineering
- Electrical Engineering
- Environmental Engineering
- Industrial Engineering
- Materials Engineering
- Mechanical Engineering
- Mining Engineering
- Nanotechnology
- Nuclear Engineering
- Power Engineering
- Test Engineering
- Transportation Engineering

We are also interested in: 1) Short Reports—2-5 page papers where an author can either present an idea with theoretical background but has not yet completed the research needed for a complete paper or preliminary data; 2) Book Reviews—Comments and critiques.

☆ Notes for Intending Authors

Submitted papers should not be previously published nor be currently under consideration for publication elsewhere. Paper submission will be handled electronically through the website. For more details, please access the website.

☆ Website and E-Mail

http://www.scirp.org/journal/eng   eng@scirp.org

Engineering, 2009, 1, 1-54
Published Online June 2009 in SciRes (www.scirp.org/journal/eng/)

TABLE OF CONTENTS

Volume 1 Number 1 **June 2009**

9771947393001 01